Dissertation
submitted to the
Combined Faculties for the Natural Sciences and for Mathematics
of the Ruperto-Carola University of Heidelberg, Germany
for the degree of
Doctor of Natural Sciences

Put forward by
Dipl.-Phys. Mario Benjamin Mendes
born in München
Oral Examination: 23.06.2010

Molecular fragmentation by recombination with cold electrons studied with a mass sensitive imaging detector

Referees: Prof. Dr. Andreas Wolf
Prof. Dr. Selim Jochim

Untersuchung der Molekülfragmentation durch Rekombination mit kalten Elektronen mit Hilfe eines massenempfindlichen Fragmentabbildungsdetektors

Die Rekombination eines molekularen Kations mit einem niederenergetischen Elektron ist ein grundlegender Reaktionsprozess in kalten verdünnten Plasmen. Bei mehratomigen Ionen können dabei ro-vibrationell angeregte Fragmente erzeugt werden. Die Unterscheidung der Zerfallskanäle mit chemisch unterschiedlichen Fragmenten und die Messung deren Anregungsenergien ist eine experimentelle Herausforderung. Diese Arbeit diskutiert ein neues experimentelles Verfahren, das auf Fragmentabbildung mit einem Siliziumstreifendetektor bei schnellen Strahlen in einem Speicherring basiert. Das Prinzip des Detektors und die Auswertetechniken werden diskutiert, und die Leistungsfähigkeit wird in einem Experiment zur dissoziativen Rekombination von CHD^+ demonstriert. Außerdem wird mit dem neuen Aufbau die dissoziative Rekombination von $DCND^+$ untersucht. HCN und das höherenergetische Isomer HNC spielen eine wichtige Rolle in der Chemie dichter interstellarer Wolken. Es ist vorgeschlagen worden, dass beide Isomere mit der gleichen Wahrscheinlichkeit in der dissoziativen Rekombination von $HCNH^+$ produziert werden. Um die Produkte dieses Reaktionskanals erstmals direkt zu untersuchen, wird die dissoziative Rekombination von $DCND^+$ mit dem neuen Detektor analysiert. Die Ergebnisse zeigen, dass DCN/DNC hauptsächlich in vibrationsangeregten Zuständen weit oberhalb der Isomerisierungsschwelle produziert wird. Die Bedeutung dessen für Verzweigungsverhältnisse und Dissoziationsmechanismus werden diskutiert.

Molecular fragmentation by recombination with cold electrons studied with a mass sensitive imaging detector

The recombination of a molecular cation with a low-energy electron, followed by fragmentation, is a fundamental reaction process in cold and dilute plasmas. For polyatomic ions, it can yield molecular fragments in ro-vibrationally excited states. The discrimination between decay channels with chemically different fragments and the measurement of their excitation energies pose an experimental challenge. This work discusses a new experimental scheme based on fast beam fragment imaging in a storage ring with a silicon strip detector. The working principle of the detector and analysis procedures are discussed, and the performance is demonstrated in an experiment on the dissociative recombination of CHD^+. Moreover, the new arrangement is used to study the dissociative recombination of $DCND^+$. Hydrogen cyanide (HCN) and its energetically higher lying isomer hydrogen isocyanide (HNC) play an important role in the chemistry of dense interstellar clouds. It has been proposed that both isomers are formed with the same efficiency in dissociative recombination of $HCNH^+$. For the first direct investigation of the products of this reaction channel, the new detector is used to analyse the dissociative recombination of $DCND^+$. The results show that DCN/DNC is mostly produced in vibrationally excited states, well above the isomerization barrier. The implications of this finding on branching ratios and the dissociation mechanism are discussed.

Contents

1 Introduction

Most of the matter in our universe is in a plasma state, which means that it is ionized to some degree. Plasmas are found in the upper atmosphere of our earth, in industrial applications (e. g. silicon etching), or in huge interstellar molecular clouds. Nevertheless, the chemical processes that occur in such a plasma are not as well understood as the "normal" chemistry we were taught at school or in undergraduate university courses. One reason is that plasmas cannot be studied in a standard test tube; instead, dedicated experimental schemes have to be developed in order to unveil the secrets of the fascinating processes involving ions.

One of the basic reaction processes of ion chemistry is the recombination of a molecular cation with a free electron, followed by subsequent breakup into neutral fragments. This process, which can be written for a simple generic diatomic ion as

$$\mathrm{AB}^+ + \mathrm{e}^- \rightarrow \mathrm{A} + \mathrm{B},$$

is usually known as *dissociative recombination* (DR). DR has been employed to understand different interesting phenomena, like the *airglow*, a faint illumination of the sky caused by ion chemistry processes in the upper atmosphere, among them DR, or the formation and destruction of molecules in interstellar space [1]. However, many secrets of this process are still undiscovered. Although a first description of the reaction mechanism has been given 60 years ago [2], many questions could not yet been answered, especially concerning the DR of *polyatomic* ions.

Our understanding of DR has been advanced since the beginning of the 1990s by the use of *heavy ion storage rings*. As far as diatomic ions are concerned, the results have been paving the way towards a comprehensive understanding of the reaction mechanisms, although there are still many open questions. For polyatomic ions, however, the situation is complicated by the fact that *chemically different decay channels* can occur and that the

production of *molecular fragments* is possible, which can have various compositions and conformations of the components and in which rotations and vibrations can be excited in many ways. This results in a much larger number of possible final states as compared to the DR of diatomic ions. Storage ring experiments conducted in the past where not able to account for these states. They have been either blind to the excitation of the fragments, or they could not determine the chemical fragment species.

In this thesis, a new experimental scheme based on a *silicon strip detector* is presented. This is a big leap in the investigation of the DR of polyatomic ions, since for the first time chemically different decay channels can be distinguished and simultaneously the excitation energies of the fragments in each of these channels can be measured in a storage ring experiment.

Chapter 2 introduces DR with regard to simple polyatomic ions. In chapter 3, the general experimental scheme based on a storage ring and the technique of *fragment imaging* is explained, and the new **E***nergy-sensitive* **MU***lti-strip detector* (EMU) is separately discussed in chapter 4. How this detector behaves in reality is shown in chapter 5 by the example of the DR of the deuterated methylene ion CHD^+. The results show a strong isotope effect, favouring the production of CD over CH.

A very fascinating problem in the chemistry of interstellar clouds is the occurrence of the isomers HCN and HNC and their observed abundance ratios. Their clearly distinguishable spectra offer a tool to probe the relative importance of different chemical pathways. To explain the strongly varying observed abundance ratios, their production by DR was considered as early as 1974 [3], while their isomeric abundances in this process so far could not yet be revealed experimentally. In order to contribute new insights to this old problem, the DR of $DCND^+$ has been studied with the EMU detector. This is presented in chapter 6. The results indicate that the production mechanism for the two isomers differs from the 'traditional' perception; the DR process leaves undetermined which isomer is formed. Instead, a highly excited fragment is produced, and the subsequent process of radiative relaxation has to be considered in order to understand the isomeric branching.

2 Dissociative recombination of small polyatomic ions

Among the various different molecular dissociation processes, the recombination of a positively charged molecular ion with an electron, followed by subsequent dissociation of the now neutral molecule, is probably of the lesser known ones. Nevertheless, being a fundamental process behind the formation and destruction of molecules in different plasma environments, it attracts a lot of interest from some research areas. Whereas both magnitude and energy dependence of the cross section revealed some of the secrets behind this process in the last decades, we are at the very beginning of being able to predict details like the possible fragment species, the branching ratios for their production, or the internal states in which they are formed. New experimental schemes are being developed in order to answer these questions. Although these methods are in principle applicable to different dissociation processes, this work focusses on the *dissociative recombination* – a good reason to look at that process in more detail.

This chapter presents an introduction to dissociative electron-ion recombination, targeted at the non-specialist. At the beginning, the relevance of this process is pointed out from the historical perspective. Basic theoretical concepts, which are frequently used to describe molecular processes, will be reviewed. On this basis, some ideas about the mechanisms behind dissociative recombination (and related processes) can be discussed – this is meant to introduce the vocabulary and to give a "sense" for these concepts.[1] Finally, some special aspects about the dissociative recombination of small polyatomic ions, i. e. ions that consist of three or more atoms, will be mentioned.

[1] For a comprehensive and more systematic introduction, the reader should consult one of the recent review articles or the book by Larsson and Orel [1].

2.1 Historical introduction

Dissociative recombination (DR), i. e. the recombination of a molecular cation with an electron, followed by the breakup into neutral atomic or molecular fragments, is a fundamental dynamical process behind many interesting real-world phenomena. The challenge presented by the DR process lies mainly in its complexity, and it explores the frontier between collision physics and physical and theoretical chemistry. For this reason, together with the wide field of applications, DR is interdisciplinary in its best sense. For the physicists it opens an opportunity to delve into important questions about the basic mechanisms behind chemical reaction processes. But also on the applications side it gives them access to research areas that receive much attention and regularly make it into the newspapers, like astronomy and planetary science. Furthermore, understanding complex dynamical processes in atomic and molecular systems does not only pose computational problems. Especially DR requires the bridging of several orders of magnitude in space and time in the description of the nuclei and electrons, and is therefore much too complex to be treated in a real *ab initio* calculation. Thus theory relies heavily on experimental input. In that sense, the investigation of such processes gives the researcher the opportunity to advance the understanding of a particular subject, since theory and experiment are closely linked and profit from each other – a situation that is not always met in other fields of physics, where a lot of theoretical work is devoted to interesting but experimentally not yet accessible questions. It turns out that very fundamental aspects of the reaction mechanisms behind DR are not well understood. Progress in this field is achieved by unveiling these mechanisms step by step.

An excursion into the world of dynamical processes of molecular systems shows that they have played a central role in some of the most exciting research areas of the last decades. When the space age began in the 1950s, it also boosted the interest in the physics of the upper atmosphere and of the other bodies in our solar system.[2] Even more, it gave us access to the whole spectrum of electromagnetic radiation coming from sources outside the closer vicinity of the earth and thus stands for the advent of a new era in astronomy. All these subjects require a deep understanding of molecular processes, and accidentially we owe the interest in DR mainly to its relevance in the above mentioned environments.

[2] The first ICPEAC (International Conference on Photonic, Electronic and Atomic Collisions) was held in 1958 in New York, showing the big interest in atomic collision physics at that time. The reader may remember that the *International Geophysical Year* falls in the period from July 1 1957 to December 31 1958 and that the first *Sputnik* was launched at that time.

One can better appreciate the significance of DR if one is familiar with at least some of the cornerstones of its history. This section is meant to give an idea about the development of this research area. It cannot provide a detailed historical account, nor is it supposed to cover the various interrelationships with the general development of science.[3] Furthermore, it reflects the author's opinion about the most important aspects of DR and deliberately gives a taste of the rest of this work and how it fits in the whole picture.

Interestingly, this history starts with different questions about the upper atmosphere. When Guglielmo Marconi succeeded to make the first transatlantic radio transmission between Cornwall and Newfoundland in 1901, this was only possible due to an atmospheric layer that reflected the radio waves and enabled them to bridge the curvature of the earth on a zigzag path. Soon it was suggested that this could be an ionized and thus conducting layer, which is nowadays known as the Heaviside layer (or Kennelly-Heaviside layer, or simply E region). It was not until 1924 that Edward Appleton was able to prove the existence of this layer. For this work he received the Nobel Prize in 1947.

Once the existence of a plasma layer in the atmosphere had been established, it provided an explanation for a well known but so far not understood phenomenon: the auroral green line at 557.7 nm. The first step was the identification of atomic oxygen as the source of this line. In 1931, Kaplan proposed that the recombination of ionized molecular oxygen and an electron can lead to the dissociation into oxygen atoms in the excited ^1S state [4]. The transition $^1S - {}^1D$ is then responsible for emission of the green line. He also noticed that the green line is not only seen in aurorae, but also in the spectrum of the night sky (the *airglow*, as it is also called), and therefore proposed that the mechanism should be the same in both cases. As we know today, DR is not the dominant process behind the green line in aurorae[4], but it is still considered to be a significant part of the airglow.[5]

The work of Kaplan – probably the first appearence of DR in science – shows an important aspect of DR, which is still of interest in current research topics. Kaplan points to the property of DR of producing excited atoms by an exothermic process, i.e. it does not need an additional energy source to drive the process as soon as a system is ionized. If one

[3] The interested reader is referred to the introductory chapter of the excellent book by Larsson and Orel [1], on which this section partly relies, and to some of the original publications.

[4] Collisions of molecular oxygen with N^+ have been proposed instead [5].

[5] It should be mentioned that the so called red line emission, stemming from the transition $^1D - {}^3P$ in atomic oxygen, has also been identified as a component of the airglow, although much weaker than the green line [6].

transfers this idea from the ionosphere to interstellar molecular clouds, one immediately sees its importance. Having temperatures down to the order of 10 K, these clouds need exothermic processes for the formation and destruction of molecules – processes, that are apparently going on there – and the fact that they consist of a partly ionized plasma provides one possible candidate, namely DR.

It should be emphasized here that – in contrast to the low temperature environments in interstellar clouds – there was no need to establish the existence of exothermic processes in the ionosphere, which is a place of comparatively high temperatures. Consequently, the main point in Kaplan's work is not so much the fact that DR is exothermic and thus running without energy input, but that the available energy is used to produce excited atoms. This is in contrast to the common perception that this energy goes into the kinetic energy of the fragments rather than in their internal excitation. Although this is not so much an issue any more in the context of electronic excitation, where the production of excited states could be established in many cases, it is an undecided question especially in the case of ro-vibrational excitation of molecular fragments. The criteria governing the distribution of the available energy between kinetic energy release and internal excitation are currently of interest. In that sense, Kaplan's proposition is still a challenge.

It is not possible to review all the work about ionospheric processes in the 1930s and 1940s. As far as DR is concerned, some serious attempts have been made in order to unveil the reaction mechanism behind the process and estimate reaction cross sections, e. g. in [7], but it was evident that there was not yet enough understanding of the process. At the end of this period, new microwave experiments established a large cross section and paved the way to the understanding of the reaction mechanisms in the 1950s and 1960s. From the 1970s on, an increasing interest from astrochemistry was a further driving force pushing the research about DR. Some of these developments will be mentioned in sections 2.2.2 and 2.4 and chapter 6 in this thesis.

2.2 Basic concepts

2.2.1 The Born-Oppenheimer approximation and non-Born-Oppenheimer concepts

Molecules consist of a certain number of nuclei plus some electrons. All these constituents are charged and interact with each other via Coulomb forces. Thus, from the point of view of theory, a molecule is accurately described by a few-body Hamiltonian, which can only be treated numerically in an "exact" way.

It is however a common procedure to reduce the complexity of the problem by making simplifying assumptions. This leads to approximate but intuitive pictures about molecular processes. Such approaches are discussed in any textbook about molecular physics and shall not be discussed here in full detail (see e. g. [8]). It might however prove to be helpful for the reader if some of the basic ideas are repeated in this section.

A well known ansatz states that the light electrons move much faster than the heavy nuclei. For that reason, the kinetic energy of the nuclei is assumed to be small and the corresponding term in the Hamiltonian is treated perturbatively, i. e. the unperturbed Hamiltonian $\hat{H}_0$ includes the kinetic term of the electrons and all potential energy terms. The eigenfunctions ϕ_n pertaining to this Hamiltonian are sometimes referred to as *electronic wavefunctions*, although the corresponding eigenvalues E_n^0 also contain the repulsion of the nuclei. This is known as the *adiabatic* ansatz, since the electrons follow the slow motion of the nuclei adiabatically.

When solving the electronic problem, the positions of the nuclei are held fixed. For simplicity consider only diatomic molecules. The internuclear distance R appears as a parameter in $\hat{H}_0$. Thus, the eigenvalues depend on R. By expressing the eigenvalues of $\hat{H}_0$ as a function of R one obtains the so-called *adiabatic potential curves* $E_n^0(R)$. For polyatomic molecules this concept can be generalized to the *adiabatic potential energy surface* (PES). This is an extremely important concept, since it gives a pictorial representation of molecular processes.

The functions ϕ_n form a basis which is known as the adiabatic basis. The solutions of the eigenvalue problem for the full Hamiltonian $\hat{H}\psi = E\psi$, $\hat{H} = \hat{H}_0 + \hat{T}_N$, whereas $\hat{T}_N$ is the kinetic operator of the nuclei, can be expressed in the adiabatic basis as $\psi = \sum \chi_n(R)\phi_n$ with coefficients χ_n that depend only on the internuclear distance R. In the well known *Born-*

Oppenheimer approximation [9] this reduces to a single term, $\psi_{n,i}(\vec{r}, R) = \chi_i(R)\phi_n(\vec{r}, R)$ ($\vec{r}$ stands for all electronic coordinates), and $\chi_i(R)$ satisfies a Schrödinger equation with $E_n^0(R)$ as potential, i. e. the Born-Oppenheimer wavefunctions $\psi_{n,i}$ factorize in an electronic and a nuclear part. Electronic and nuclear motion are decoupled, and a mixing between different electronic potential energy surfaces is neglected.

The Born-Oppenheimer approximation is a useful concept if nuclear motions in the electronic ground state of the molecule are of interest. However, it is not appropriate in many other cases. Couplings between different potential energy surfaces become important when they come very close to each other, and a breakdown of the Born-Oppenheimer approximation is to be expected.

For dissociation processes, the kinetic energy of the nuclei can become large as compared to the other energies, and the adiabatic basis is not a convenient choice in order to describe them. Whereas the unperturbed Hamiltonian $\hat{H}_0$ is diagonal in the adiabatic basis, this is not true any more for the complete Hamiltonian $\hat{H}$, i. e. $H_{0,ij} = 0$ for $i \neq j$, but $H_{ij} \neq 0$ in general. Obviously, the non-diagonal elements describe couplings between different adiabatic states, which are induced by the nuclear kinetic term: $H_{ij} = \langle\phi_i|\hat{H}|\phi_j\rangle = \langle\phi_i|\hat{T}_N|\phi_j\rangle$. In the so-called *diabatic* basis $\{\phi_i^{diabatic}\}$, however, $\hat{T}_N$ is diagonal, which produces couplings described by a non-diagonal $\hat{H}_0$.

Diabatic potential curves for states with the same symmetry are allowed to cross – for adiabatic potential curves this is forbidden by the *Von Neumann-Wigner non-crossing rule* [10]. There, an *avoided crossing* would occur. Diabatic potential curves are smoother than their adiabatic counterparts and better suited for the description in the vicinity of (nearly) degenerate configurations.

2.2.2 The dynamics behind dissociative recombination

In order to explain the high DR cross sections, D. Bates proposed an efficient dissociation mechanism in 1950 [2], which is nowadays known as the *direct* mechanism (see fig. 2.1). The ion[6] AB^+ captures the incoming electron, which results in a doubly excited state AB** of the neutral molecule. Energetically, the energy is above the ionization limit, and autoionization, which is the reverse capture process, can occur. However, the (diabatic) potential curve of the doubly excited state can be repulsive, and the nuclei might follow

[6]For simplicity, consider diatomic ions.

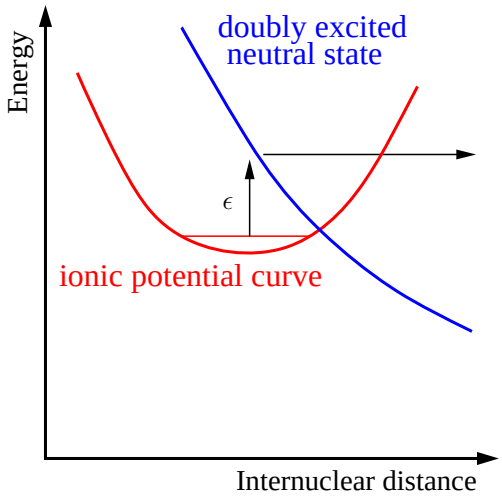

Figure 2.1: The direct process in the picture of diabatic potential curves. By capturing an electron with energy ϵ, the system is promoted to a doubly excited state AB^{**} of the neutral molecule, which has a repulsive potential curve (blue). The efficiency of the dissociation relies on a large overlap of the wavefunctions of initial and dissociative state. Here, the dissociative curve crosses the ionic ground state curve above the first vibrational level, i. e. the direct process would be inefficient for $\epsilon = 0$.

this curve until they gain as much energy that autoionization does not occur any more. In the limit $R \longrightarrow \infty$ two free atomic fragments are obtained. The *kinetic energy release* (KER), i. e. the kinetic energy of the fragments in the center-of-mass frame of the molecule, is the difference of the energy of the initial ionic state plus the electron energy ϵ and the asymptotic limit of the dissociative potential curve. Thus, the direct process can be written as:

$$AB^+(v, J) + e^-(\epsilon) \rightarrow AB^{**} \rightarrow A(n) + B(n') + E_{KER}(\epsilon, v, J, n, n'). \tag{2.1}$$

n and n' are representing *all* quantum numbers characterising the states of A and B.

In order to be efficient at low energies, the direct process usually requires a doubly excited state crossing the ground state curve of the ion close to its minimum. However, some systems, like He_2^+ [11], dissociate without such a favoured curve crossing. In 1968 Bardsley proposed the so-called *indirect* process [12], where the electron is captured in a highly excited bound Rydberg state of the neutral molecule, which is ro-vibrationally excited in order to maintain energy conservation (fig. 2.2). By internal energy conversion, this Rydberg state can be transformed to a dissociative state:

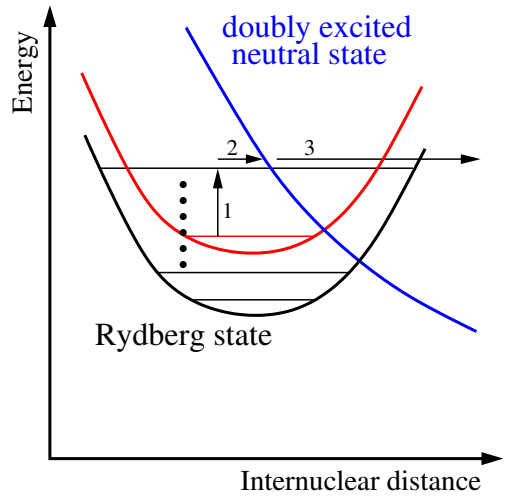

Figure 2.2: Schematic depiction of the indirect process. Only one potential curve from the Rydberg series converging to the ionic ground state curve is shown (black). By capturing the electron, the system reaches a ro-vibrationally excited level of this Rydberg state (1). From here, it can couple to the dissociative state in a second step (2), followed by dissociation along the repulsive curve (3).

$$\mathrm{AB}^+(v,J) + \mathrm{e}^-(\epsilon) \rightarrow \mathrm{AB}^*_{Ryd}(n_{Ryd},v',J') \rightarrow \mathrm{AB}^{**} \rightarrow \mathrm{A}(n) + \mathrm{B}(n') + E_{KER}(\epsilon,v,J,n,n'). \tag{2.2}$$

The dissociative state is in many cases the same as in the direct process; the indirect process is then a second alternative quantum path of the DR reaction, and interference between the two mechanisms occurs. On the other hand, the indirect process can give access to dissociative states with potential curves *below* the ionic ground state, for which the direct process would be inefficient.

So far, the fragments were assumed to be neutral, and this thesis is concerned with that case only. However, there are similar processes that yield charged fragments. The *dissociative excitation* (DE) is a dissociation in a neutral and a positively charged fragment, while there is still an electron in the final state:

$$\mathrm{AB}^+ + \mathrm{e}^- \rightarrow \mathrm{A}^+ + \mathrm{B} + \mathrm{e}^-. \tag{2.3}$$

In the *ion-pair formation* (IPF) the electron is captured, but the resulting molecule decays in two ions:

$$\mathrm{AB}^+ + \mathrm{e}^- \rightarrow \mathrm{A}^+ + \mathrm{B}^-. \tag{2.4}$$

Usually, the term DR implies that the fragments are neutral. This convention will be used throughout this work.

2.3 Some considerations regarding polyatomic ions

This work deals with the dissociative recombination of small polyatomic ions. In contrast to other fields of physics, chemistry, and biology, where "polyatomic" refers to a large number of atoms, say a few hundred, the convention used here is that every ion that consists of at least three atoms is called a "small polyatomic ion". This sets no upper limit to the number of atoms, and it rises the question where "small" ends. Without a strict definition, it will be assumed to imply that the fragmentation channels can still be distinguished one by one in a suitable DR experiment. This is in contrast to "large" polyatomic ions, where every imaginable real experiment could at best be expected to obtain more general statements about classes grouping several dissociation channels together. On the other side, this definition makes clear that the DR of polyatomic ions is considered to be different from the case where one only has diatomic ions. This difference will now be discussed.

As an example take a generic triatomic ion ABC^+. For this ion, there can be four different decay channels[7]:

$$\begin{aligned} ABC^+ + e^- &\rightarrow A + B + C \\ &\rightarrow AB + C \\ &\rightarrow A + BC \\ &\rightarrow AC + B. \end{aligned}$$

The most important difference is obvious: Whereas diatomic ions produce always the same fragments, small polyatomic ions can dissociate in different ways, leading to different fragment species. This rises the question which of the four possible final states are actually populated, and how likely their production is.

A further peculiarity of polyatomic ions can be observed. Diatomic ions can only dissociate into atomic fragments. In contrast, small polyatomic ions can also produce molecular fragments. This has implications regarding the energetics of the process. Obviously, the

[7] Not all of these decay channels must be exothermic. Whether all of them can occur as a final state may depend on the energy of the incoming electron.

energy that is released in the reaction (the *exothermicity*) goes – in the diatomic case – either into the kinetic energy release or into electronic excitations of the atomic fragments. As discussed already, some diatomic ions, like O_2^+, can decay into electronically excited fragments. However, since both the exothermicities in DR as well as atomic excitation energies are in the same order of magnitude ($\sim$ eV), there is usually only a small number of final states with different excitations. A standard example is HD^+: If this ion is in its vibrational ground state, the only final states that are accessible in collisions with electrons at a relative energy $E = 0$ eV are $[H(n = 1) + D(n = 1)]$ and $[H(n = 1) + D(n = 2)]$ or $[H(n = 2) + D(n = 1)]$, respectively. The experiment [13] shows that only events with one atom in an $n = 2$ state are observed, according to the theoretical prediction that dissociation proceeds to this final configuration via the lowest lying $^1\Sigma_g^+$ state. This means that all events in the DR of HD^+ have the same KER.

The situation is different for the DR of polyatomic ions. In this case, it is possible to produce molecular fragments in states with excited nuclear motions, i. e. ro-vibrationally excited states. Since the energy spacings between these states are considerably lower, there is usually a huge number of energetically accessible final state configurations with different internal energies and thus different KERs. Consider one of the decay channels with a molecular fragment of the generic triatomic example:

$$ABC^+ + e^- \rightarrow AB(J, v) + C.$$

For the moment electronic excitations are neglected. The parent ion ABC^+ is assumed to be in a well defined state, say its electronical and ro-vibrational ground state. The molecular fragment AB is in an excited state with rotational quantum number J and vibrational quantum number v. The KER for that dissociation event is

$$E_{KER}\,(ABC^+ + e^- \;\rightarrow\; AB(J, v) + C) = E_0 - E_{rot}(J) - E_{vib}(v),$$

where E_0 is the exothermicity:

$$E_{KER}\,(ABC^+ + e^- \;\rightarrow\; AB(0, 0) + C) = E_0.$$

Thus, one gets information about the excitation of the fragments by measuring the KER, provided the initial state of ABC^+ is known. In a typical experiment the knowledge about

the latter is usually incomplete, since the ions are produced in excited states by the ion source. Infrared active vibrational modes may relax to the vibrational ground state in a reasonable time, especially in a storage ring experiment, where the ion beam is given some seconds to cool before the measurement starts. For the rotational motion relaxation times can be considerably longer (see appendix B). In addition, the room temperature environment of many experimental apparatuses can at best allow the ions to be in thermal equilibrium with their surrounding[8] and thus prohibits that all of them reach the rotational ground state.[9]

Despite the incomplete knowledge about the initial state, this method is very practicable when it comes to the determination of ro-vibrational excitation energies of the fragments. It was already mentioned that these states are very dense in energy. Even if rotational substates are neglected and only the vibrational states are considered, there is sometimes a huge number of them in the energetically accessible region. One is therefore usually not interested in the population of some specific states. Instead one would ask e. g. for the *distribution* of (ro-vibrational) excitation energies of the fragments. The measurement of the KER yields this information easily within the uncertainty limits given by the incomplete knowledge about the excitation of the initial ion. However, the identification of specific states fails naturally due to the small energy spacings (and to the experimental scheme used to measure KERs, which does not resolve these energy spaceings, as will be discussed later).

This shows now the whole complexity of the DR of small polyatomic ions:

- the fragmentation can yield different fragment species (sometimes called *chemical* branching);
- as a special case of chemical branching, fragments can be produced as different isomers;
- the fragments can be in different electronically and/or ro-vibrationally excited states (sometimes called *physical* branching).

[8] Here, the possibility of so called super-elastic collisions (SEC) [14] is neglected. They are inelastic electron-ion collisions, where the electron carries away a part of the initial internal energy of the ion.

[9] One can turn the argument around: If the states of the fragments are known, the KER provides the excitation of the parent ions.

For diatomic ions one is only concerned about physical branching, and there only between different electronically excited states. This is the reason why the DR of small polyatomic ions is much more complex than that of diatomic ions.

Once there are different possible final configurations, one may ask about their *branching ratios*. The chemical branching is especially interesting from the point of view of interstellar chemistry (see section 2.4). DR is an important process in chemical reaction networks of interstellar clouds, since the abundances of many chemical species depend sensitively on the yield of different fragments in DR reactions. Naturally, there is a strong interest in DR branching ratios from the side of people who are modelling these reaction networks. However, their theoretical prediction is a challenge. There is actually no general way to calculate them with satisfying results. Different general approaches have been made using a statistical phase space model [15] or more intuitive arguments dealing with the reconfiguration of chemical bonds [16, 17], but none of them gives a convincing insight in the fundamental processes, nor are the predictions always in agreement with the experimental results. Quantum chemical calculations can in principle be used to solve the problem, but their application is not straightforward. Such calculations have been done only in a few cases.

When it comes to physical branching ratios, the situation is not much better. Considering only electronic excitations, predictions can be made by identifying the dissociation pathway(s), i. e. the dissociating state(s) that can be accessed from the ionic ground state. E. g. in the case of the theoretically and experimentally well understood ion HD^+ only the channel [H($n = 1$) + D($n = 2$)] or [H($n = 2$) + D($n = 1$)], respectively, occurs, whereas the channel with both fragments in the $n = 1$ state, which is energetically allowed, cannot be accessed from the ground state of the ion. This changes with the energy of the incoming electron. For more complex ions, similar effects can be observed. However, their interpretation is not as straightforward, because they can have a rich structure of different potential curves and even interference of different fragmentation pathways towards the same products is possible. Complete switching between dissociation pathways leading to different states of the fragments within a small energy region has been observed in the DR of CF^+ [18]. For small polyatomic ions one has to know the geometry of all involved potential energy surfaces – a very complex problem, requiring time consuming calculations. The increasing complexity with increasing number of nuclei and/or electrons makes precise predictions practically impossible.

The worst situation is that of the understanding of ro-vibrational excitation. So far, the experimental database is very limited, and the processes leading to ro-vibrational excitation of the fragments are unclear. A simple statistical model has been developed in order to describe fragment excitations in the DR of H_3^+ [19]. To the author's knowledge, no further attempt has been made so far to predict ro-vibrational branching ratios or energy distributions, respectively.

In chapter 6 we will face a very special case of different final states: One of the possible fragments can show up in two different isomeric configurations. In some sense, the two isomers are different chemical species, since different chemical bonds are involved, and this can be considered as an example of chemical branching. However, one could argue that both isomers are made of the same atoms and represent two geometrically different states of the same molecule, corresponding to different local minima in the same PES. In that sense, the energetically higher lying isomer could be seen as an "excited" state, and one would rather speak of physical branching. In any case, additional vibrational excitation can allow the nuclei to move around violently, making it difficult to attribute one of the two isomeric states to the fragment. This shows that chemical and physical branching are not completely independent from each other; the distinction between them is somehow artificial. It will be shown that the question about the isomeric branching cannot be answered without considering the vibrational excitation.

2.4 The role of DR in interstellar chemistry

About 150 molecules have been found in interstellar and circumstellar environments so far, plus further molecules in comets, planetary atmospheres, brown dwarfs and stellar atmospheres [20]. Very fascinating objects are the dense cloud 'cores', some of them being quiescent, others containing active star forming regions. The temperatures can be as low as 10 K. These "dense" regions of molecular gas contain about 10^4 particles per cm^3, and it is fascinating that molecules can form in such cold and dilute gases. However, many of the molecules are ions, and it is the *ion chemistry* that drives many of the formation and depletion processes.

The first models of interstellar chemistry have been developed in the 1950s, e. g. by Bates and Spitzer [21]. The role of ions has further been clarified in the 1970s by Herbst and Klemperer [22] and, independently, by Watson [3]. One of the processes they considered

is DR. By DR molecular ions are destroyed, while new molecules can be formed as decay products of polyatomic ions. Furthermore, many fragments are radicals, i. e. DR provides reactive atoms and molecules for further reaction processes. Since DR is exothermic and needs no energy input in order to overcome a reaction barrier, it can easily occur even in the coldest places within interstellar clouds.

In order to simulate the chemical evolution of such clouds, the main processes have to be identified and reaction cross sections as well as branching ratios have to be known as good as possible. These information are listed in databases, e. g. in the UMIST database [23]. However, many of the data are still not known or have only been estimated.

An example showing how molecules are formed by DR and why accurate data about DR branching ratios are needed will be discussed in chapter 6.

3 Fragment imaging in storage ring experiments

This chapter deals with the experimental side of dissociative recombination. While different experimental techniques have been used in the last decades to study this process, the most common being investigations with stationary or flowing afterglow plasmas, but also single-pass merged-beam experiments, the experimental schemes discussed here are exclusively those based on heavy ion storage rings. Other methods are reviewed in [1, 24, 25].

3.1 Storage ring investigations of dissociative recombination

Since the beginning of the 1990s, heavy ion storage rings like CRYRING in Stockholm, Sweden, ASTRID in Aarhus, Denmark, and TSR in Heidelberg, Germany, have boosted our understanding of DR. They allow to study this process under well controlled conditions [1].

A storage ring is in fact an ion trap. It consists at least of an evacuated beam tube that allows the ions to move on a closed orbit, where they are confined using magnetic and/or electrostatic fields. All of the above mentioned storage rings use magnetic fields and allow to store beams of singly charged ions with an energy of a few MeV.

In particle physics, storage rings are normally used as *colliders*, i. e. two counterpropagating particle beams are stored in the same or in two different beam pipes, while at specific points the two beams overlap and eventually produce collisions. The goal is to obtain as much collision energy as possible in the center-of-mass frame of the colliding partners. In contrast, the experiments presented in this work require very low collision energies, extending down to the meV range, or one even wants the reaction partners to be

at rest relative to each other. This is limited by the beam temperatures, as will be discussed below and in section 3.4, but can be achieved sufficiently well regarding the demand to simulate the conditions in cold interstellar environments.

Obviously, performing collision experiments at such low energies is an experimental challenge. Ironically, it is again the storage ring that allows to realize such ultra-low energy collisions. This requires of course to use a different scheme than the collider. Instead of studying head-on collisions of counterpropagating beams, one uses overlapping electron and ion beams that move in the *same* direction. Whereas the velocity of the ion beam is usually fixed, the velocity of the electrons can be chosen accordingly, allowing them to move at the same velocity as the ions or at a slightly different velocity.

In practice, such merged-beam sections have a length of about one meter. The ion beam circulates in the storage ring and passes the merged-beam section once in every revolution, while the electron beam is constantly produced and destroyed after one pass (see fig. 3.1). The merging and demerging is achieved using toroidal magnetic fields. Since the mass of the ions is much higher than the electron mass, the motion of the ions is hardly disturbed by these fields.

Assume now that electrons and ions move in the same direction with speed v_e and v_i, respectively, with $v_e \geq v_i$. Their kinetic energies are $E_e = \frac{m_e}{2} v_e^2$ and $E_i = \frac{m_i}{2} v_i^2$, the collision velocity[1] as seen from the rest frame of the ion is $v_{coll} = v_e - v_i$. Hence we get

$$\sqrt{\frac{2E_{coll}}{m_e}} = \sqrt{\frac{2E_e}{m_e}} - \sqrt{\frac{2E_i}{m_i}},$$

where E_{coll} is the collision energy, i. e. the kinetic energy of the electron with respect to the ion rest frame. Finally, we obtain

$$E_{coll} = \left(\sqrt{E_e} - \sqrt{\frac{m_e}{m_i} E_i} \right)^2 . \tag{3.1}$$

This reduces to

$$E_e = \frac{m_e}{m_i} E_i \tag{3.2}$$

if we require the collision energy to be zero. For a real experiment the velocities have to be

[1] Sometimes, the collision velocity v_{coll} is called *detuning velocity* v_d, because the velocity of the electrons is *detuned* from the ion beam velocity: $v_e = v_i + v_d$. At least in a zero temperature beam, v_{coll} and v_d are the same – for finite electron beam temperatures, however, they should be distinguished.

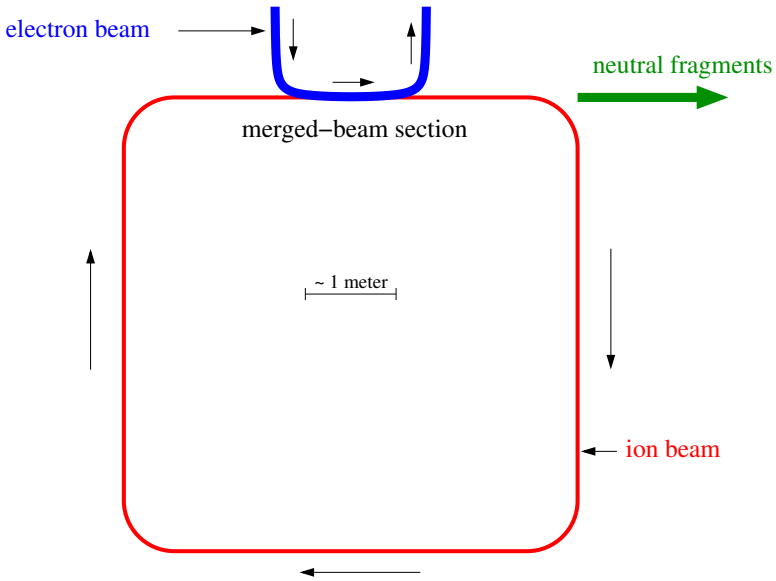

Figure 3.1: Schematic depiction of the general setup of a DR experiment using a storage ring. The reaction takes place in the merged-beam section, where electron and ion beams overlap at a length of about one meter. The neutral fragments are not deflected by the magnets and keep the momentum they have after dissociation, thus allowing to separate them from the ion beam in the upper right corner. Electron and ion beams always move in the same direction; the electrons can be chosen to be both faster and slower than the ions. Same velocity of the electrons and ions corresponds to lowest possible collision energies, limited only by the temperature of the electron beam.

understood as averaged velocities.

The overlapping velocity-matched electron beam is also capable to reduce the velocity spread of the ions. This process, the *phase space cooling* of the ion beam, is applied after the injection of the ions into the storage ring and precedes the measurement phase. It is a prerequisite to perform the experiment at a well defined collision energy. How this is achieved in practice will be explained in section 3.4.

The phase space cooling is one reason for the great success of the storage ring method. Another one is the possibility to give the ions time to relax internally. Ions coming from an ion source usually show high vibrational and rotational excitation. Infrared active ions can relax radiatively while they are stored, allowing them to equilibrate with their room temperature environment. In many cases the vibrational ground state is reached within a reasonable time, usually within milliseconds. However, the cooling of the rotations to the room temperature level (which means that the rotations are still excited to some degree)

can last significantly longer. The experiments discussed in this thesis demonstrate that it is not guaranteed that even ions with a permanent electric dipole moment are capable of that within the timescales on which the measurements have to be performed (see also appendix B).

Besides the advantage to prepare a both internally as well as translationally cold ion beam, the storage ring method offers rather simple detection schemes. Due to the high beam velocity of a few thousand kilometers per second (beam energies between a few hundred keV and more than one MeV per nucleon), the fragments created in an DR event (energy release: about one eV) leave the merged-beam section always in forward direction, confined within a narrow cone. At the next dipole magnet, they are separated from the ion beam and enter a beamline which contains detectors capable to record them with an effective 4π sensitivity.

Before some of these detectors are discussed, it should be reviewed what kind of observables one might be interested in. The following list gives at least the most important ones:

- the absolute reaction cross section at $E_{coll} = 0$;
- the reaction cross section as a function of E_{coll};
- the branching ratios for chemically different decay channels;
- the kinetic energy release, containing information about both parent ion and fragment excitations and branching ratios or energy distributions thereof;
- the geometry of the breakup.

This spectrum of different observables usually requires different detectors. They are discussed in the next section.

3.2 Detectors for storage ring experiments

3.2.1 Solid state detectors

The solid state detector [26], usually made of silicon and designed as a *surface barrier* [27] or a *fully depleted p-n junction detector* [28], respectively, has intensively been used in storage ring experiments aimed at the investigation of DR and related processes due to its simplicity.

It is basically a diode operated in reverse-biased mode.[2] Charged particles penetrating the detector material create free charges in the form of electrons and holes in an amount proportional to their kinetic energy. This requires that these particles are completely stopped within the detector. The free charge can be measured after amplification.

The different fragments stemming from the same dissociating molecule arrive at the detector within only a few nanoseconds and can thus not be resolved in time. Consequently, a signal proportional to the total kinetic energy of all fragments of the same dissociation event is produced in an unsegmented solid-state detector covering the fragmentation cone completely.

Let the velocity in the ion rest frame be $\vec{v}_i'$ for the i-th fragment. In the laboratory frame, the ion moves with velocity $\vec{v}_{beam}$, and we get $\vec{v}_i = \vec{v}_{beam} + \vec{v}_i'$ as the fragment velocity in the laboratory frame. Since we have $|\vec{v}_i'| \ll |\vec{v}_{beam}|$, we get $|\vec{v}_i| \approx |\vec{v}_{beam}|$, i. e. all fragments hit our detector with the same velocity. Thus, for a single fragment i,

$$E_{kin,i} \propto m_i. \tag{3.3}$$

Regarding the signal measured by the unsegmented detector, this means

$$\text{pulse height} \propto E_{kin} = \sum_i E_{kin,i} \propto \sum_i m_i,$$

where the sum has to be taken over all fragments that actually hit the detector. Thus, the solid state detector measures the mass of all fragments hitting it simultaneously.

The mass-sensitivity of the solid state detector allows to discriminate between DR and other events, such as DE or fragments from collisions with the residual gas. For a DR event (in the narrower sense), only neutral fragments occur. Thus, one would expect to measure the mass of the whole dissociating molecule, provided all fragments hit the detector. This is possible due to the fast beam scheme as discussed in the previous section, while relatively large detectors are used[3]. In summary, the solid state detector identifies DR events mass-spectroscopically. As long as it is not segmented (see chapter 4) or used in conjunction with further devices such as grids (see below), it does not provide any details like fragment species or even the number of fragments.

[2] The operation of solid state detectors will be discussed in more detail in chapter 4.
[3] The author knows of detectors of quadratic shape with a size of up to 10 cm.

Being a very fast detector with a sensitivity close to one, the solid state detector is the first choice when reaction rates have to be determined. From these rates the cross sections can be deduced. The actual observable in these experiments is the number of events in a time interval – the mass-sensitivity is only used to identify DR events.

Besides of its main application as a counter used to determine cross sections, the solid state detector can – in conjunction with a grid with known transmission – obtain chemical branching ratios [29]. The grid stops a part of the fragments, so that even for DR events the observed mass is not always equal to the mass of the dissociating molecule. This leads to a measured pulse height spectrum with different peaks between the mass of the lightest fragment (for the case that all fragments except for the lightest one are stopped by the grid) and the total mass (if all fragments pass the grid). From the number of events in each peak together with the known transmission of the grid, the branching ratios can be deduced by solving a set of linear equations. In order to eliminate the influence of background events stemming from collisions with the residual gas, the electron beam is usually switched on and off on a relatively short time scale (switching rates ~ 50 Hz), allowing to determine signal and background almost simultaneously. The pulse height spectrum recorded with no electrons has then to be subtracted from the one with electrons "on", leaving a pure DR spectrum.

Although this has been the only successful methode so far to study chemical branching ratios in storage ring experiments, it has its limitations. Due to background reasons, it is mainly applied at low collision energies, where the DR rate is quite high. For some molecules, the results of different experiments differ by about 10 % for the yield of some channels, like in the case of H_3O^+ [30, 31]. The agreement with afterglow experiments can even be worse. Different transmissions of the *same* grid for light and heavy fragments have been reported [32]. This shows that some initial problems in the application of the grid method had to be solved. In recent years, the results seem to be more reliable, but, nevertheless, it would be desirable to have an independent technique to check them, e. g. to have better diagnostic tools like an online monitoring of the phase space cooling.

3.2.2 Fragment imaging detectors

Whereas cross sections and chemical branching ratios can be measured in a storage ring experiment using solid state detectors, a tool for the investigation of the internal states of

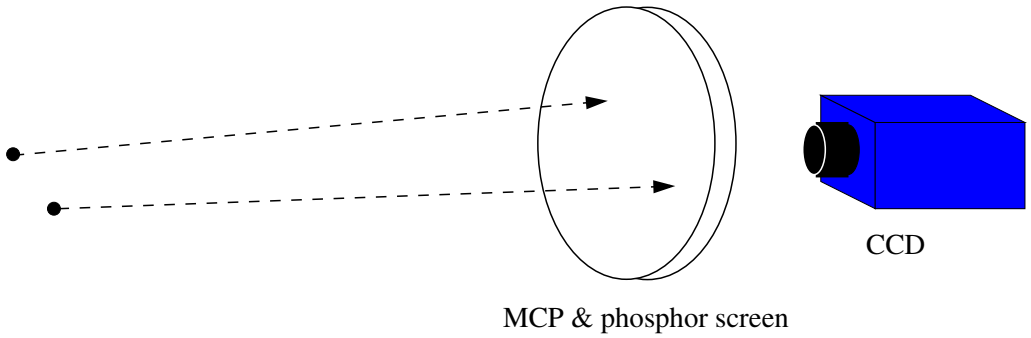

Figure 3.2: A simple fragment imaging detector, consisting of a micro-channel plate (MCP), a phosphor screen (anode), and a CCD camera. A fragment hitting the MCP creates an electron cloud which is accelerated towards the phosphor screen and produces a light spot. Since all fragments stemming from the same dissociation event arrive within a few nanoseconds, they are seen on the same camera image (exposure time $\sim$ 10 ms). Fragment masses cannot be recorded!

the fragments and the breakup geometries is still needed. Such a tool is introduced in the following; it is called *fragment imaging detector* [33].

The fragment imaging detector (see fig. 3.2) is a position sensitive detector, capable to detect the individual fragments. Its goal is to reconstruct the asymptotic momenta of the fragments after dissociation, either completely (*3D imaging*) or at least in the plane perpendicular to the flight direction (*2D imaging*). This is achieved by recording the impact positions of the fragments on the detector, allowing to reconstruct the momenta in the transversal direction. The momenta along the flight direction are obtained from the measurement of impact times. Such detectors have been used in investigations of different dissociation processes, like photodissociation [34], dissociation in atom-molecule collisions [35], or dissociative charge exchange [36] (for a review see [37]).

Typically, a fragment imaging detector consists of a micro-channel plate[4] [38] in the first place, together with some kind of anode in order to extract the position and time information. Nowadays, phosphor screens are frequently used as anodes. Light spots on the screen mark the impact positions of the fragments and allow to record them with a CCD[5] camera, which has the advantage that both data acquisition and analysis can make use of well tested commercial equipment and image analysis software conforming to industry standards. Other setups include multi-wire [39] or delay line anodes. These detectors

[4] http://en.wikipedia.org/wiki/Microchannel_plate_detector
[5] charge coupled device

are partly capable of performing 3D imaging measurements. For this application, even segmented photomultipliers have been used [40]. Time resolutions as good as 140 ps [41] have been achieved with these devices, while the spatial resolution lies typically at about 100 μm.

The fragmentation of small polyatomic ions is a challenge regarding possible fragment multiplicities. Whereas a CCD camera can record in principle an unlimited number of light spots on a phosphor screen, the methods applied to obtain time information fail or become very costly for more than two fragments. In the last years, a new approach has been followed which makes use of a second CCD camera equipped with a light intensifier that acts as a fast optical shutter [42, 43, 44, 45]. Very short exposure times of about 10 ns allow to extract time differences from the brightnesses of the different light spots on a single camera frame. This method overcomes the limitation of other detection schemes and is suited for multi-fragment imaging. Although the timing information is obtained with sub-nanosecond resolution, it is not yet as good as for other detectors and often prohibits to gain an additional benefit compared to the 2D information. For that reason, 2D imaging techniques are still the preferred method for the investigation of the breakup of small polyatomic molecules.

3.3 Fragment imaging techniques

3.3.1 Fragmentation of diatomic molecules

The 2D imaging technique will be discussed now, first for the simpler case of the fragmentation of a diatomic molecule. In a 2D imaging experiment, only the impact positions of the fragments on the detector are recorded, allowing to reconstruct the kinematics of the fragmentation in the *transversal* direction (i. e. perpendicular to the flight direction). No information is gained about the *longitudinal* motion of the fragments.

The basic idea behind an imaging experiment is depicted in fig. 3.3. When hitting the detector, the fragments have attained a macroscopic distance d_{3D}, which is a direct measurement of the kinetic energy release E_{KER}, as will be shown now.

In the center-of-mass frame, we have

$$E_{KER} = E_{kin,A} + E_{kin,B} = \frac{1}{2} m_A v_A'^2 + \frac{1}{2} m_B v_B'^2 = \frac{1}{2} \frac{m_A m_B}{m_A + m_B} v_{rel}^2, \tag{3.4}$$

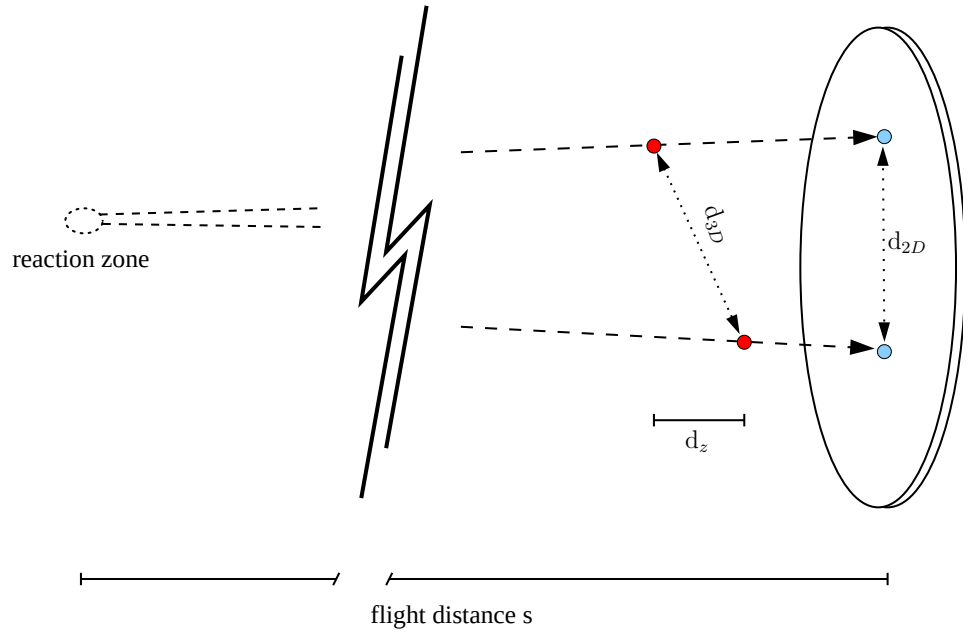

Figure 3.3: A dissociation event with two fragments. Their impact positions on the detector are separated by the distance d_{2D}. In a 2D imaging experiment, the information about d_z is not recorded.

where m_A and m_B are the masses, v'_A and v'_B the velocities of the two fragments A and B in the center-of-mass frame, and $v_{rel} = |\vec{v}_{rel}| = |\vec{v}_B - \vec{v}_A| = |v'_B - v'_A|$ is their relative velocity. In the laboratory frame, the dissociating molecule moves with the velocity v_{beam}. After a time t, the distance of the fragments is $d_{3D} = v_{rel}t$. The distance when hitting the detector can be expressed in terms of the flight distance s:

$$d_{3D} = v_{rel}\,\frac{s}{v_{beam}}. \tag{3.5}$$

Finally, this has to be related to the kinetic energy release:

$$E_{KER} = \frac{1}{2}\frac{m_A m_B}{m_A + m_B}\left(\frac{d_{3D}\,v_{beam}}{s}\right)^2 = \frac{1}{2}\frac{m_A m_B}{m_A + m_B}\left(\delta \cdot v_{beam}\right)^2, \tag{3.6}$$

where $\delta = d_{3D}/s = v_{rel}/v_{beam}$ is the maximal angle between the flight paths of the two fragments.

A 3D imaging detector would measure the distance d_{3D} and obtain the KER for each event using eq. 3.6. 2D imaging detectors, however, yield only the *projected* distance d_{2D},

as shown in fig. 3.3, which in addition depends on the angle under which the two fragments are ejected in the center-of-mass frame. From the projected distance alone the KER cannot be extracted for a single event.

A further complication comes from the fact that the flight distance s is not known exactly, because the dissociation could have taken place anywhere in the merged-beam section. However, one can assume that the probability to get a DR event is constant over the whole reaction zone[6].

The KER can be extracted from the projected distances d_{2D} of many events under the following assumptions:

- all events have the same KER,
- the reaction rate is constant over the reaction region, the length of this region is known.

Under these circumstances, d_{2D} has a maximum that obviously corresponds to the KER, taking the largest possible flight distance s in eq. 3.6. In many cases, it also is a good approximation to assume an additional condition to hold:

- the angular distribution of the fragment paths in the center-of-mass frame is isotropic.

This holds well in the case of zero average collision energy, where the incident electron directions are statistically distributed. Although not all directions in the angular distribution are equally frequent in general, the effective anisotropies of the DR rates for small average collision energy have been found to be small. In that case, the normalized distribution of the projected distances for $E_{KER} = E_j$ is known and can be given as an analytical expression [47]:

$$P_0(d_{2D}, j) = \begin{cases} \frac{1}{\delta_j L}\left(\arccos\frac{d_{2D}}{\delta_j s_2} - \arccos\frac{d_{2D}}{\delta_j s_1}\right) & \text{for } 0 \le d_{2D} \le \delta_j s_1 \\ \frac{1}{\delta_j L}\arccos\frac{d_{2D}}{\delta_j s_2} & \text{for } \delta_j s_1 \le d_{2D} \le \delta_j s_2 \\ 0 & \text{otherwise.} \end{cases} \tag{3.7}$$

s_1 and s_2 are the minimum and maximum flight distances, and $L = s_2 - s_1$ is the length of the interaction region.

[6] Except for the merging and de-merging sections, where toroidal effects sometimes have to be considered [46]. For imaging measurements, however, corrections are usually not applied.

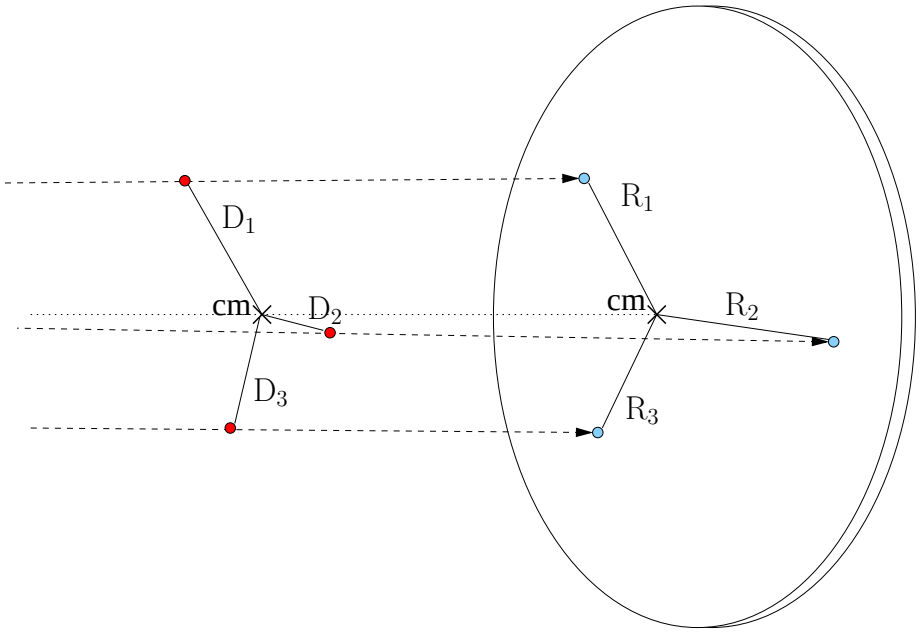

Figure 3.4: A dissociation event with three fragments. The distances R_i of the impact positions from the center-of-mass (cm) are needed in order to reconstruct the transversal KER, as explained in the text.

For different final state configurations with differing kinetic energy releases, the expected distribution is a sum of such distributions:

$$P_0(d_{2d}) = \sum_j b_j P_0(d_{2d}, j), \tag{3.8}$$

where b_j with $\sum b_j = 1$ is the branching ratio of the j-th decay channel. By fitting such a function to the measured data, the branching ratios can be extracted.

More information about imaging of the breakup of diatomic molecules, especially for anisotropic angular distributions, can be found in [47] and [45].

3.3.2 Fragmentation of small polyatomic molecules

Small polyatomic molecules can decay in two fragments, and these decay channels are treated in the very same way as diatomic molecules. However, once the number of fragments exceeds two, different techniques have to be applied. Some basics will be reviewed here. A comprehensive discussion can be found in [48].

As in the diatomic case, the KER is $E_{KER} = \sum_i E_i$, with $E_i = m_i v_i'/2$. The sum has now to be taken over all fragments. After the flight distance s, the fragments have gained the macroscopic distance

$$D_i = v_i' \frac{s}{v_{beam}},$$

measured with respect to the center-of-mass. The detector, however, can observe only the projected distances R_i (see fig. 3.4). Following the conventions in [48], we define

$$\varepsilon_i^{\perp} = m_i R_i^2 \tag{3.9}$$

and

$$E_i^{\perp} = \frac{E_{beam}}{M\, s^2}\, \varepsilon_i^{\perp}, \tag{3.10}$$

where $M = \sum m_i$ is the total molecular mass. The *transversal kinetic energy release* is defined as

$$E_{KER}^{\perp} = \sum_i E_i^{\perp}. \tag{3.11}$$

It depends on the orientation of the fragment paths and can obviously not exceed the KER. In the case of three fragments, the transversal KER equals the KER if the plane of the fragments is parallel to the detector plane.

The flight distance s is not known exactly, as mentioned before. It would be desirable to have expected distributions available for similar assumptions as in the case of two fragments. Unfortunately, these distributions are not known for the general case. For *three* fragments, one usually proceeds as follows: In the center-of-mass frame, the paths of all three fragments lie in the same plane. The orientation of this plane is assumed to be isotropically distributed with similar justification as described in section 3.3.1 for the diatomic fragmentation. The transversal KER distribution is obtained by a Monte-Carlo simulation. As shown in [48] (see fig. 4.9 there), there is an additional dependence on the geometry of the fragmentation in the plane. A linear geometry and a triangular fragmentation pattern would cause different distributions. Therefore, additional considerations regarding the distributions of fragmentation geometries are necessary[7]. However, all resulting distributions of $E_{KER}^{\perp}$ have the same energetic end point, corresponding to the KER at maximum flight distance. Since

[7] For example, one would like to have these geometries equally distributed over the available phase space, i. e. one would assume a constant phase space density. The available phase space can be parametrized using *Dalitz coordinates* [49]. For details see [48].

$E^{\perp}_{KER}$ cannot be reconstructed for a single event due to the unknown flight distance s, only $\varepsilon^{\perp} = \sum \varepsilon^{\perp}_i$ is usually plotted.

It should be noted that it is not sufficient to know the impact positions of the fragments, but that their masses are also required in order to determine $\varepsilon^{\perp}$. For diatomic molecules, this is no problem at all; the masses of the two fragments are known anyway, and it is not necessary to distinguish between them in the observation, since the only required quantities in the analysis of the energy release are their projected distance d_{2D} and the reduced mass. For three or more fragments, however, the projected distance of each fragment with respect to the center-of-mass as well as its mass are required in order to calculate $\varepsilon^{\perp}$. For a well cooled beam, the center-of-mass is always at about the same position on the detector, resulting in a distribution of the center-of-mass positions with a width below one millimeter in the present experiments. This can help to assign masses to the fragments (by testing all possible mass assignments and choosing the one whose center-of-mass position fits best), but it is not always sufficient for a non-ambiguous mass assignment. Therefore, an independent mass determination is desirable. Actually, the lack of mass-sensitivity for common imaging detectors presents a problem in two ways:

- For more than two fragments, the individual fragment masses are needed in order to determine $\varepsilon^{\perp}$, as discussed above.

- Small polyatomic ions can have more than one decay channel with two fragments (e. g. AB + C and A + BC), which can in most cases be distinguished by the masses of the fragments. Data sets for these channels must be separated through the knowledge of the fragment masses for any kinematical analysis to be performed.

For these reasons, a mass-sensitive 2D fragment imaging detector would be of great value in the investigation of the fragmentation of small polyatomic molecules.

3.4 The storage ring TSR and the beamline BAMBI

The experiments presented in this thesis have been performed at the heavy ion storage ring TSR (*Testspeicherring* or *Test Storage Ring*[8]) at the Max-Planck-Institut für Kernphysik

[8]The abbreviation is nowadays preferred, since the original meaning does not quite fit the scope of application of this device.

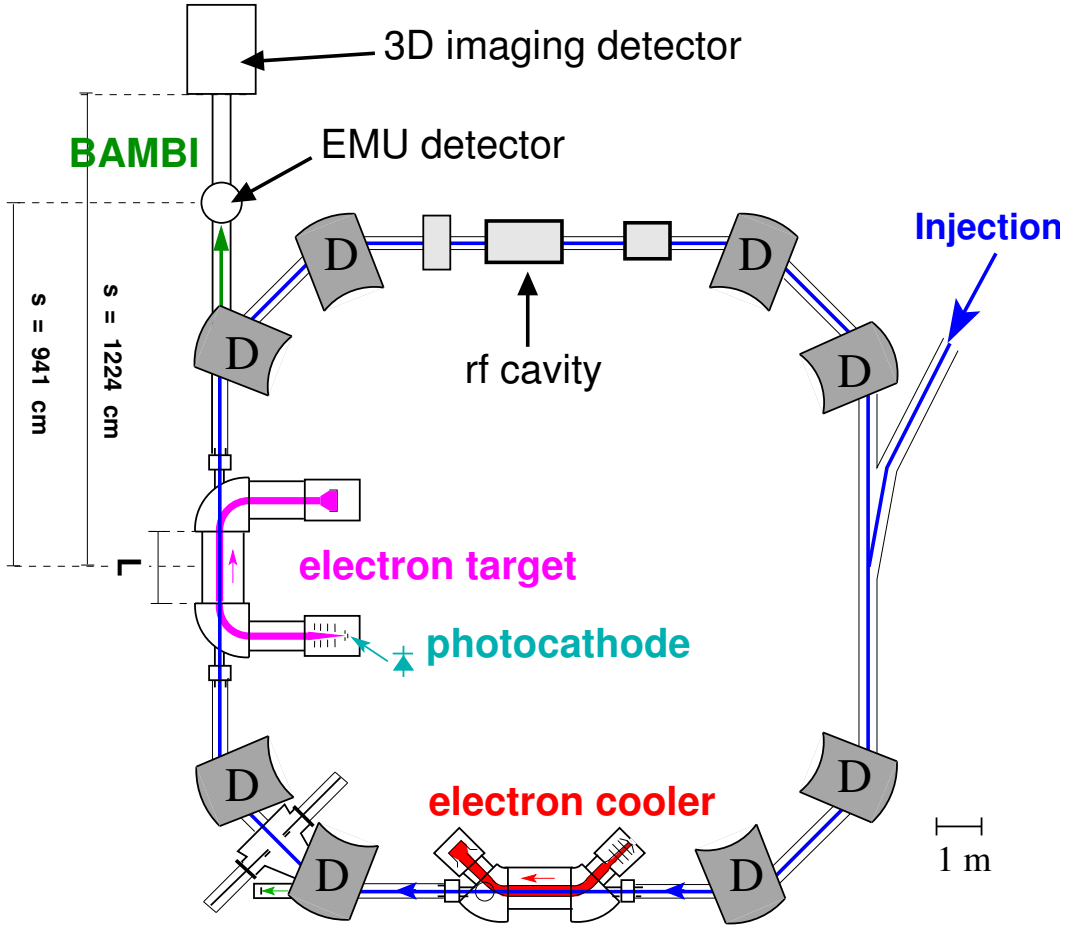

Figure 3.5: A simplified picture of the TSR and the experimental beamline BAMBI. Of the beam guiding devices only the dipole magnets (D) are shown. The 3D imaging detector (see section 3.2.2) and the new EMU detector (chapter 4) are located at distances 1224 cm and 941 cm, respectively, behind the center of the electron target. Both electron target and electron cooler provide merged-beam sections that can be used for phase space cooling of the ion beam as well as recombination experiments.

in Heidelberg, Germany (see fig. 3.5). As already mentioned, this is a magnetic storage ring with the possibility to store singly charged molecular ions with energies of a few MeV.

The TSR is in operation since 1988 [50] and has been used in many experiments with atomic and molecular ions. It did also serve as a tool to study experimental techniques such as phase space cooling of ion beams. Its beam pipe has a circumference of 55.4 m and can be evacuated to a pressure of $\approx 3 \cdot 10^{-11}$ mbar, with the residual gas consisting mainly of hydrogen. The good vacuum conditions allow to store molecular beams for several seconds up to about one minute – long enough to apply phase space cooling before the measurement.

Several ion sources and accelerators are available for the production of the ion beams, among them a tandem accelerator, a single stage van de Graaff accelerator, and the so-called *High Current Injector* (HSI, *Hochstrominjektor*) [51], an RF linear accelerator. They are able to provide a broad spectrum of different ion beams, like highly charged atomic ions or molecular ions with masses up to at least 31 u [9].

The TSR (fig. 3.5) has an octagonal shape with dipole magnets in the corners, allowing to store beams with a rigidity of up to 1.5 Tm. Higher order multipole magnets serve as focusing elements.

There are four long straight sections. The ion beam is injected into the TSR at one of them, and another one is occupied by beam diagnostics tools as well as an rf cavity that can be used to accelerate or decelerate the beam.

The specialty of the TSR compared to similar storage rings is the fact that there are *two* merged-beam sections at the two remaining sides. Both of them provide cold electron beams for phase space cooling of the ion beam and electron-ion recombination experiments. The *electron cooler* [52] produces electrons using a thermionic cathode, whereas the *electron target* [53] takes advantage of a photocathode yielding even colder beams. This twin-beam setup opens new opportunities. For example, the beam can first be cooled by both cooler and target. The measurement can then be performed with a different velocity of the electron beam in the target, corresponding to some nonzero collision energy, while the cooler still maintains the velocity of the electrons matched to the ion beam velocity and thus prevents the ion beam from heating up again. Especially for systems with long cooling times, doubling the beam cooling power can be advantageous. On the other hand, using two electron beams reduces the lifetime of the ion beam by increased recombination rates.

[9] unified atomic mass units

The low temperatures of the electron beams are achieved by slow acceleration as well as adiabatic expansion in the transversal direction [54]. This leads to different temperatures in longitudinal and transversal direction, $T_\parallel$ and $T_\perp$, respectively, in the co-moving frame of the electrons. The velocity distribution of the electrons is described by an anisotropic double Maxwellian distribution [55]

$$f(\vec{v_e}) = \frac{m_e}{2\pi k T_\perp} \left(\frac{m_e}{2\pi k T_\parallel} \right)^{1/2} \exp\left(-\frac{m_e v_\perp^2}{2kT_\perp} - \frac{m_e v_\parallel^2}{2kT_\parallel} \right) \tag{3.12}$$

(for the case $v_d = 0$, i. e. same average velocities of electron and ion beam), where $v_\parallel$ and $v_\perp$ are the electron velocities in the beam direction and perpendicular to it, respectively, in the rest frame of the ion beam. Using a liquid nitrogen cooled GaAs-photocathode [56] as electron source in the electron target, temperatures as low as $kT_\perp \approx 1\,\mathrm{meV}$ and $kT_\parallel \approx 50\,\mu\mathrm{eV}$ can be reached [57]. For comparison, the electron cooler, which is only equipped with a thermionic cathode, produces beams with $kT_\perp \approx 10\,\mathrm{meV}$ and $kT_\parallel \approx 0.1\,\mathrm{meV}$.

The experimental beamline *BAMBI* (**B**eamline for **A**dvanced **M**olecular **B**reakup **I**nvestigations) is located downstream the electron target, behind the next dipole magnet. It contains detectors for neutral fragments, aimed at the investigation of DR. A 3D imaging detector, based on MCP, phosphor screen and two CCD cameras [43], is situated at the very end of the beamline, at a distance of 1224 cm behind the center of the electron target (see fig. 3.5). Two solid state detectors can be inserted directly in front of the imaging detector. The new *EMU detector*, to be discussed in chapter 4, has been installed closer to the reaction zone at a distance of 941 cm behind the center of the electron target. Since June 2008, it completes the detectors at the TSR, about 20 years after its starting.

Thus, the TSR offers outstanding opportunities to study questions related to DR. Both the twin-beam setup with the worldwide coldest electron beam in the electron target as well as the range of available detectors are unique and allow to perform experiments with unprecendented precision and to tackle new aspects of the DR process, paving the way to new insights into molecular dissociation processes.

4 The EMU detector

4.1 General considerations

As discussed in chapter 3, different detectors are needed in order to address different aspects of the DR process in a storage ring experiment. While they perform quite well within the application range they are aimed at, they are still not able to answer all the questions that have been envisaged hitherto, in particular with a focus on polyatomic ions:

- The grid method [29] has so far been the only way to measure chemical branching ratios in a storage ring experiment. Since the results obtained in afterglow experiments often differ quite a lot from the storage ring results [24] (while of course in many cases they might also be attributed to different internal excitations of the ions as well as to "hotter" collisions), it would be desirable to have at least one different technique. The grid method inherently suffers from background problems – which is one of the reasons why it is usually only applied at zero collision energies. Although the results obtained nowadays seem to be reliable, it is obvious that the application of the grid method is not as straightforward as originally expected, e. g. as observed for the DR of H_3O^+ [30, 32, 31]. The published results differ between 18 % and 33 % yield for the decay channel H_2O + H.

- As discussed in chapter 3, the fragment imaging methods used to investigate the fragmentation of diatomic molecules can in principle also be applied for two-body fragmentation channels of polyatomic molecules. This requires, however, that the different two-body channels can be distinguished from each other and from incompletely detected three-body channels. Since the common imaging detectors are insensitive to fragment masses, this is not possible in general.

- The fragmentation channels with more than two fragments pose another challenge even if the decay channel is known, since one has to assign the correct mass to the

impact position of each fragment in order to reconstruct the kinetic energy release. The lack of mass-sensitivity for the so far available detectors prohibited this in many cases.[1]

These problems lead to the conclusion that the insensitivity to fragment masses is the main drawback of the common experimental schemes. This applies to the usual non-segmented solid state detectors as well, since they can measure only the total mass of all fragments hitting them (see chapter 3).

The ideal solution would be a pixelized solid state detector with fully individual readout of each pixel. However, such a detector is not available in the size needed (about 10×10 cm^2). A more realistic concept is a *silicon strip detector* with strips in x-direction on the front and in y-direction on the back side, with individual readout of each strip. The impact position of each fragment then lies at a crossing point of a vertical and a horizontal strip; the two strips measure a signal proportional to the kinetic energy of that fragment. As already discussed in chapter 3, the kinetic energy is proportional to the mass (see eq. 3.3). Thus, one can find the mass of the fragment, as well as its impact position given by the individual strip readouts.

This concept will be discussed now with regard to the analysis of DR events. Two very simple examples are shown in fig. 4.1. The *geometrical arrangement* of the fragments causes a certain *signal pattern* (or *hit pattern*, as will be said from now on), i. e. an arrangement of strips yielding a set of mass readouts. One is interested in the relation between geometrical arrangement and hit pattern. As seen in the figure, the geometry can be assigned to the hit pattern without difficulty for the two examples shown. A non-ambiguous assignment of hit pattern and geometry of the event can be made under the following conditions:

- the mass of each fragment occurs only once;
- all fragments hit different strips in both x- and y-direction.

These conditions are sufficient but not necessary. If the first condition is true and it is allowed that two (or more) fragments hit the same strip in either horizontal or vertical direction (fig. 4.2), the corresponding geometrical arrangement can again be extracted immediately from the hit pattern.

[1] Obviously, this is not a problem in some special cases like the three-body decay of H_3^+, where all fragments have the same mass.

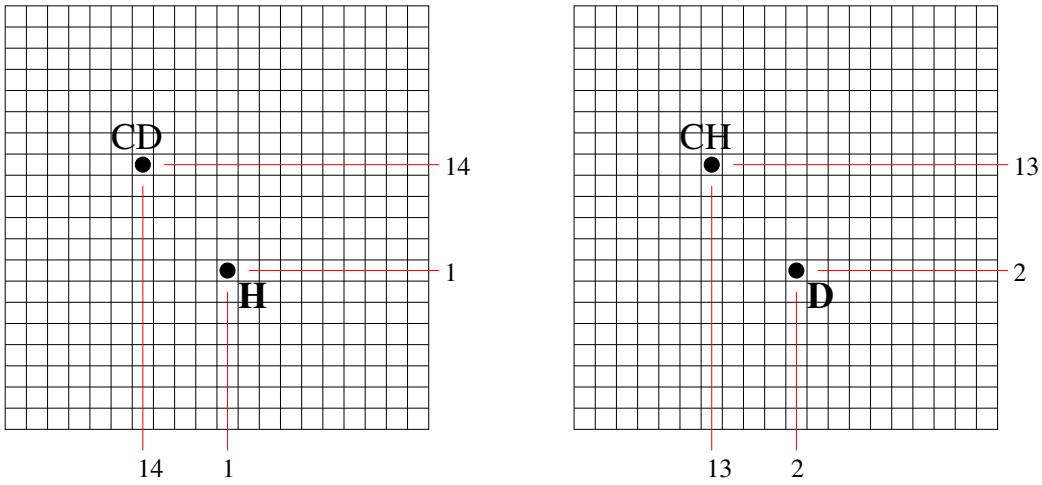

Figure 4.1: Left: An event belonging to the channel CD + H of the DR of CHD^+ as it would be seen by a silicon strip detector with both horizontal and vertical strips. Each strip that was hit by a fragment measures a signal proportional to the mass of the fragment, as depicted by the numbers. In this case, the two fragments hit different strips in both x- and y-direction, allowing to determine the fragment masses as well as the impact positions. Right: An analogous event for the channel CH + D. Obviously, the two events can be distinguished.

Dropping the requirement that each fragment mass occurs only once reveals the first type of geometrical ambiguity (see fig. 4.3). Assume that there are ν fragments with the same mass and that all of them hit different strips with coordinates $x_1,\ x_2, \ldots, x_\nu$ and $y_1,\ y_2, \ldots, y_\nu$, respectively, implying $x_i \neq x_j,\ y_i \neq y_j$ for $i \neq j$. Pick the fragment with x-coordinate (vertical strip) x_1; the corresponding y-coordinate y_{x_1} can be *any* of the available y-coordinates $y_1,\ y_2, \ldots, y_\nu$, i. e. there are ν possible pairings (x_1, y_{x_1}) as coordinates of the first fragment. Once the coordinates of the first fragment have been assigned, there are $\nu - 1$ possibilities (x_2, y_{x_2}) for the second fragment. In total, there are $\nu!$ geometrically different arrangements with the same hit pattern. In reality, the case $\nu = 2$ occurs frequently (e. g. in D_2H^+, D_3O^+, $DCND^+$), i. e. it is *not unusual* that there are *two* different interpretations of the geometry of some events, as shown in fig. 4.3. It should be stressed, however, that this ambiguity affects only the impact positions, not the masses of the fragments.

Fortunately, the observables that are needed in an energy-related imaging analysis, namely the position of the center-of-mass and the transversal KER (or rather $\varepsilon^\perp$), are not affected by this ambiguity, as will be shown now. Assume that there are N fragments with masses

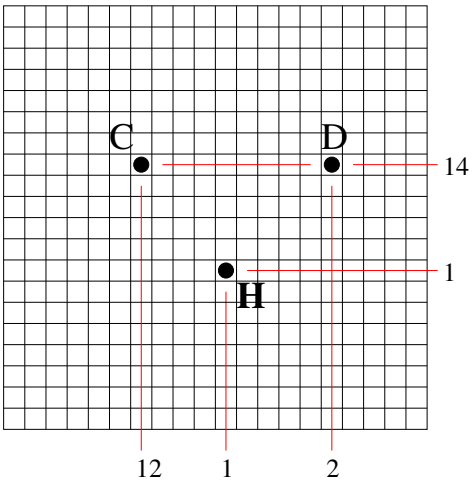

Figure 4.2: An event with three fragments, two of them hitting the same horizontal strip. The fragment masses as well as the impact positions can be assigned to the hit pattern.

$m_1, \ldots, m_N$ and that n_x vertical and n_y horizontal strips have been hit, while $n_x,\ n_y \leq N$, i. e. the possibility of multiple hits on the same strip is taken into account. The masses recorded by these strips are $m_{x_1}, \ldots, m_{x_{n_x}}$ and $m_{y_1}, \ldots, m_{y_{n_y}}$, respectively. Furthermore, we obviously have to require that

$$M = \sum_{i=1}^{N} m_i = \sum_{i=1}^{n_x} m_{x_i} = \sum_{i=1}^{n_y} m_{y_i},$$

i. e. that the total mass of all fragments is seen on the horizontal as well as the vertical strips. The positions of the strips are $x_1 \ldots,\ x_{n_x}$ and $y_1 \ldots,\ y_{n_y}$, and the coordinates of the individual fragments are $(X_1, Y_1), \ldots, (X_N, Y_N)$ with $X_i \,\epsilon\, \{x_j | j = 1, \ldots, n_x\}$ and $Y_i \,\epsilon\, \{y_j | j = 1, \ldots, n_y\}$ for all i. It follows that

$$m_{x_i} = \sum_{\text{all } j \text{ with } X_j = x_i} m_j$$

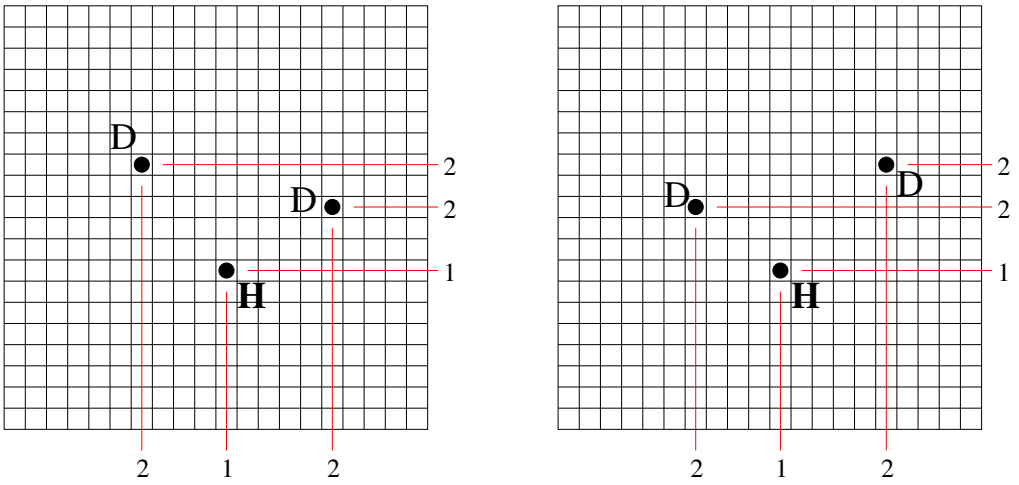

Figure 4.3: A hit pattern that can be interpreted two different ways, corresponding to two different geometrical arrangements of the fragments. The reason is the occurrence of two fragments with the same mass. Although the positions are ambiguous, it should be noted that the masses of the fragments and thus their chemical species are the same in both interpretations!

and the same for m_{y_i}. For the center-of-mass, we get

$$\begin{aligned}(x_{cm}, y_{cm}) &= \frac{1}{M}\left(\sum_{i=0}^{N} m_i X_i, \sum_{i=0}^{N} m_i Y_i\right) \\ &= \frac{1}{M}\left(\sum_{i=0}^{n_x} m_{x_i} x_i, \sum_{i=0}^{n_y} m_{y_i} y_i\right). \end{aligned} \tag{4.1}$$

The last expression contains only the strip positions and the masses recorded by these strips. Thus, the determination of the center-of-mass is independent of the assignment of fragment positions to the hit pattern. Now consider $\varepsilon^{\perp}$:

$$\varepsilon^{\perp} = \sum_{i=1}^{N} m_i[(X_i - x_{cm})^2 + (Y_i - y_{cm})^2].$$

Again, this can be expressed in terms of the hit pattern:

$$\varepsilon^{\perp} = \sum_{i=1}^{n_x} m_{x_i}(x_i - x_{cm})^2 + \sum_{i=1}^{n_y} m_{y_i}(y_i - y_{cm})^2. \tag{4.2}$$

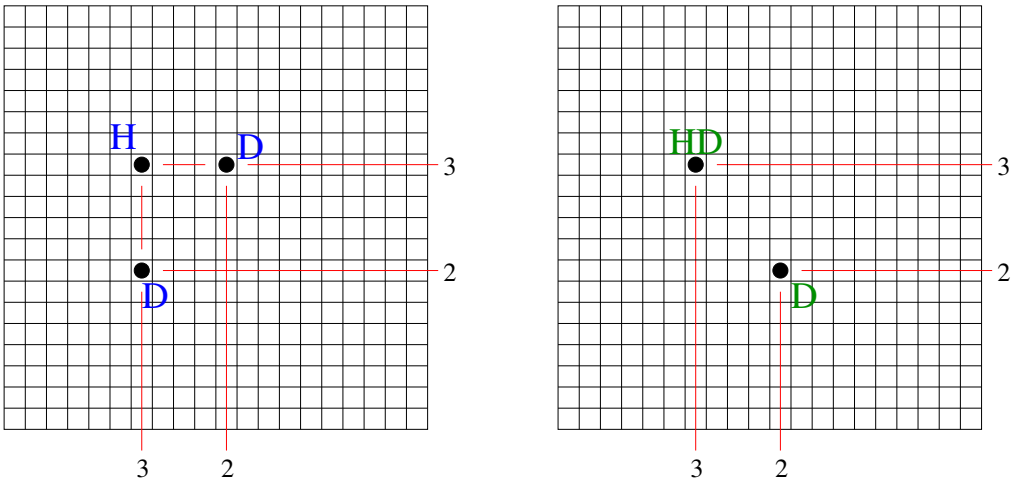

Figure 4.4: A hit pattern that can be interpreted two different ways, corresponding to two different fragmentation channels with chemically different fragments. Obviously, this ambiguity is caused by a possible "L-shaped" (here rather "Γ-shaped") geometrical arrangement, i. e. by double hits on both a vertical and a horizontal strip, while two fragments with the same mass are involved.

This leads to the conclusion that, as for the position of the center-of-mass, the information on the transversal KER depends only on the hit pattern and not on the assigned geometrical arrangement of the fragments.

Thus, we obtain the most important statement regarding imaging measurements with a silicon strip detector: *The position of the center-of-mass as well as $\varepsilon^{\perp}$ depend only on the hit pattern, i. e. on the masses recorded by the strips and the strip positions, and are not affected by ambiguities in the interpretation of the hit pattern in terms of fragment masses and impact positions.* This allows to perform energy-related analysis of imaging experiments even for systems where fragments with the same mass occur, like the one shown in fig. 4.3. Nevertheless, the fragmentation *geometries* are ambiguous.

Considering now again the case of multiple hits on the same strip, more severe additional ambiguities are met. A very prominent example is the occurence of "L-shaped" (or "Γ-shaped") events with fragments of the same mass in the corners (fig. 4.4), which are misinterpreted as events of a chemically different decay channel. Thus, these events will have an influence on the measured branching ratios. This effect can only be accounted for using a Monte-Carlo simulation. However, the probability of getting such an event can be reduced by using narrow strips with small pitch and choosing the ion beam energy such

that the impact positions of the fragments cover almost the entire detector. There are other ambiguities in L-shaped events with fragments of different mass in the corners (see fig. A.4 in appendix A).

Apart from these special cases, a silicon strip detector yields all the information necessary to obtain branching ratios and KERs for the different decay channels and is thus ideally suited for experiments with small polyatomic ions. The reconstruction of these observables will be discussed once some further aspects related to the actual implementation of such a device have been discussed (see section 4.3.2).

4.2 The physics of silicon detectors

Solid state detectors [26] are sometimes also called *semiconductor diode detectors*, and this name probably reflects best their working principle[2]. They consist of a crystalline semiconductor like silicon. Silicon is tetravalent, i. e. the four valence electrons usually form covalent bonds with the neighbouring atoms. These electrons, which are bound to specific lattice sites, belong energetically to the *valence band*. They can be excited to the *conduction band*, where they can freely move around within the semiconductor, leaving behind an open position or *hole* that can be filled by other electrons. Thus, the formation of an electron-hole pair provides two charge carriers, that can drift around until they recombine with their corresponding counterpart. By applying an external electric field, these charge carriers preferably drift along the field lines, i. e. a current is flowing through the semiconductor material.

The density of charge carriers depends on the temperature as well as the band gap between conduction and valence band. However, the conduction properties can be influenced by *doping*. A small impurity of a pentavalent element will provide electrons very close the conduction band, which can easily be excited without leaving a hole. Such impurities are called *donor impurities*, and the resulting semiconductor material with electrons as *majority charge carriers* is called an *n-type material*. A trivalent impurity (*acceptor impurity*) would create energy levels just above the valence band. Electrons can be excited to these levels, leaving a hole without being excited to the conduction band. Such a semiconductor is called a *p-type material*. Heavily doped materials with almost metallic properties are refered to

[2]Solid state detectors and the properties of semiconductors are treated in many textbooks about solid state physics.

as n^+ and p^+, respectively.

Having both a p-type as well as an n-type region in the same silicon crystal results in a *p-n junction*. The majority charge carriers can migrate across the border between n-type and p-type material towards the zone of smaller concentration and recombine there with their respective counterpart, leaving the fixed centers (donor and acceptor atoms) behind in the junction. Thus, a space charge builds up, resulting in an electric field pointing from the n-type to the p-type material. This field establishes a barrier for the majority carriers. An equilibrium is reached once the diffusion current of the minority charge carriers compensates the one of the majority charge carriers.

The diffusion of the majority charge carriers into the region of lower concentration reduces their concentration in the region of their origin, which results in a *depletion zone*. Due to the low charge carrier concentrations, the depletion zone has a high resistance. By increasing the potential barrier height between p-type and n-type side, i. e. by reverse-biasing the p-n junction, the depth of the depletion zone can be increased. Typically, a p-n junction detector is operated with a much higher bias voltage than the contact potential that builds up without external voltage. Since the resistivity of the depletion zone is higher than in the remaining material, almost the whole voltage that is applied will occur across the depletion zone.

Once a fast charged particle penetrates the detector, it creates electron-hole pairs within the detector material. The high electric field in the depletion zone separates the two types of charge carriers. Thus, the depletion zone serves as the active volume of the detector. In a *fully* (or *totally*) *depleted* detector, it extends practically through the whole size of the detector.

For example, consider an n-type silicon wafer with a thin p^+ doped layer at one surface (fig. 4.5). Due to the large hole concentration in the p^+ layer, the depletion zone will extend far in the (lightly doped) n-type material. By reverse-biasing the detector, i. e. by applying a negative voltage on the surface with the p^+ layer with respect to the other side, the depletion zone can be increased until it extends basically through the whole detector. Only the p^+ layer and the n^+ layer at the opposite side have that high impurity concentrations that the respective majority charge carriers are always present, while the minority charge carriers are strongly suppressed. Thus, both layers serve as blocking contacts and prevent the occurence of leakage currents due to the flow of the minority charge carriers.

At the front side of the detector, both the heavily doped layer and the electrode represent

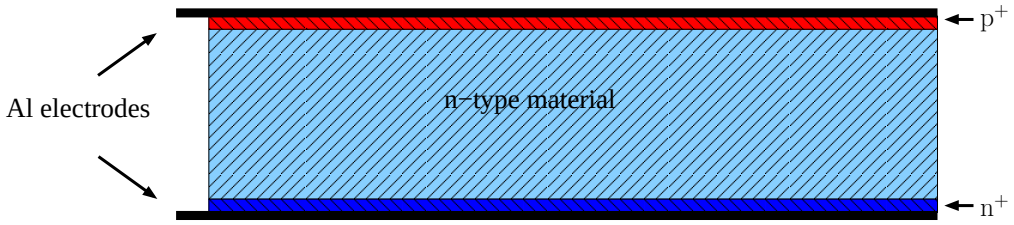

Figure 4.5: Cross section of a typical fully depleted p-n junction detector, as it is found in many applications. The bulk material is n-type silicon. At the upper surface, the p^+ layer provides a high concentration of holes with the result of creating a large depletion zone in the n-type material. By reverse-biasing the detector, the thickness of this depletion zone can be increased until it extends to the n^+ layer at the lower surface, which serves as a "blocking" contact between silicon and aluminum electrode.

a dead layer, where penetrating particles lose energy which is not detected (lack of a field that separates the charge carriers). It is therefore a design goal to make this *entrance window* as thin as possible, especially for low energy particles with high charge, as they occur in a DR experiment[3]. E. g. the range of 200 keV protons in silicon is less than 2 μm [58]. A thickness of the entrance window well below one μm is therefore essential.

The small ranges of DR fragments in silicon (μm) guarantee that all their kinetic energy is deposited within the detector. On the other hand, this occurs very close to the front surface, and the free electrons that are created have to drift quite a long distance to the electrode at the back side (assuming that the p^+ layer is at the front side). On their way, they can freely drift perpendicular to the electric field lines. When the electron cloud arrives at the back side, it is spread over a larger area than it was occupying in the beginning. This has to be taken into account, if a position sensitive readout is intended.

4.3 The EMU project: Implementation of a mass-sensitive fragment imaging detector

The goal of having a silicon strip detector available as a tool for the investigation of the DR of small polyatomic ions has been realised at the TSR with the **E**nergy-sensitive **MU**lti-strip detector (**EMU**) [59]. Since this thesis focuses on the application of the detector rather

[3]The fragments are neutral, but once they penetrate the detector, the electrons are broken away from the nuclei.

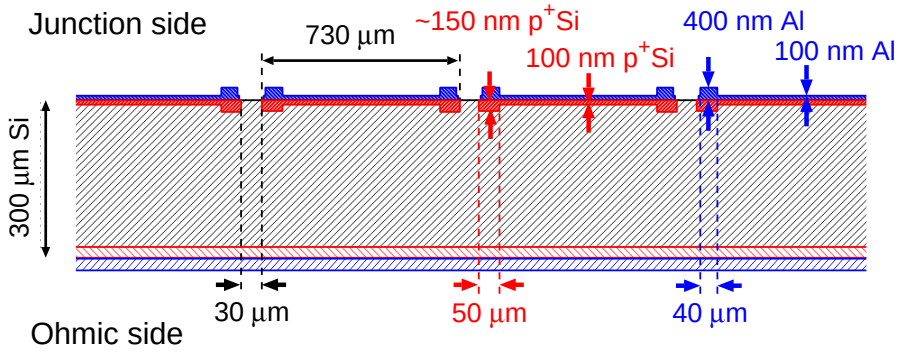

Figure 4.6: A cross section through the EMU detector (schematically). The entrance window, consisting of a p^+ layer with an aluminum coating at the junction side, was made as thin as possible. However, it is thicker at the edges of the strips, which results in a bigger undetected energy loss for fragments hitting these spots [59]. (Picture credit: H. Buhr)

than its design, the description of the physical components will be compact. However, the handling of the data and especially the reconstruction of the observables of interest ("event reconstruction") will be discussed in a more comprehensive manner.

4.3.1 Detector hardware

The EMU detector, acquired by the Max-Planck-Institut für Kernphysik and developed in a collaboration with the Weizmann Institute of Science in Rehovot, Israel, has been assembled at the Weizmann Institute and was moved to Heidelberg in May 2008. The detector itself has been manufactured by Micron Semiconductors Ltd. [60], while the electronics have been delivered by Mesytec GmbH [61].

The detector structure applied is a fully depleted p-n junction silicon strip detector with an active area of 97.3 mm × 97.3 mm. A cross section is shown in fig. 4.6. The junction side is the front side of the detector and therefore needs a very thin entrance window. The p^+ doped layer has a thickness of only 100 nm and is covered by 100 nm aluminum. At the edges of each strip, however, both the p^+ as well as the aluminum layer are thicker, as shown in fig. 4.6. These edges, applied by Micron Semiconductors in order to well delimit the strip regions, affect about 14 % of the area. In total, there are 128 strips with a width of 730 μm on the front side, separated by gaps of 30 μm (760 μm pitch). The back side is in the company's standard design; the number of strips is again 128, but with a width of

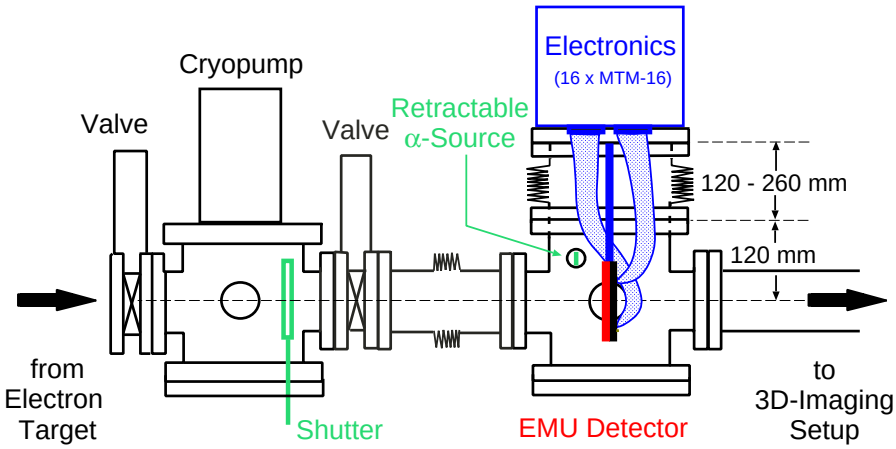

Figure 4.7: Schematic view of the EMU setup in the beamline BAMBI with the cryopump chamber and the new EMU chamber [59]. (Picture credit: H. Buhr)

700 μm and 60 μm gaps. The total thickness of the detector is 300 μm. It is biased with about 70 V.

The detector is mounted in a dedicated chamber in the beamline BAMBI downstream the electron target at a distance $s = 941(1)$ cm from the center of the target (see fig. 4.7). Horizontally, it is located directly on the centerline of the beam tube, whereas it can be moved vertically thanks to a large bellows. This allows to retract it completely out of the beamline in order to perform experiments with the detectors behind the EMU setup. A retractable alpha source can be used for testing or calibration purposes. During operation, the EMU chamber is only pumped by cryopumps in neighbouring chambers, especially the one in the next chamber upstream. The detector chamber is decoupled from the cryopump by a bellows in order to protect the detector from mechanical vibrations. A mechanical shutter is located upstream in the cryopump chamber and can be placed in front of the detector in order to protect it during the phase of injection of the beam.

The 256 strips are read out by 16 highly integrated MTM-16 modules (fig. 4.8), each of them containing preamplifier, main amplifier, pulse shaper and a hold stage for 16 strips. All 16 modules are controlled by a single MDI-2 VME unit. The MTM-16 modules as well as the MDI-2 are developed by Mesytec. The eight MTM-16 boards for the front side of the detector are serially connected to one of two function blocks of the MDI-2, and so are the eight modules of the back side to the other. The controlling, timing and read out of the MTM-16 modules is done by the MDI-2 unit. Each MTM-16 compares the input

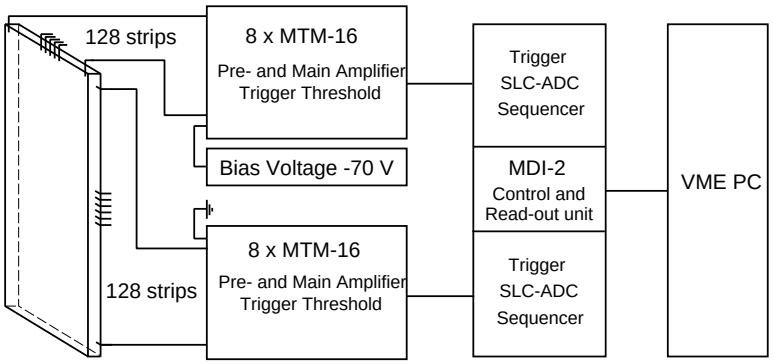

Figure 4.8: Schematic view of the electronic setup for the EMU detector [59]. (Picture credit: H. Buhr)

signal to an individually adjustable discriminator level (trigger threshold), while the signals of four input channels are added, and in case one of the discriminators responded the charge integrated signals are stored in the hold stage and the readout sequence is started by the MDI-2. There, the individual pulse heights are digitized by a sliding scale ADC and – if above a second programmable threshold independent from the trigger threshold – stored together with the strip number in a FIFO, which is read out via the VME interface. Currently, the maximum readout speed is limited to about 2000 events per second.

4.3.2 Event reconstruction and data analysis procedure

Definition of goals

The EMU detector can deliver a wealth of information, and a proper handling and management of the data is essential in order to efficiently extract all the information content. This is especially important in the light of the high event rate of about one kHz, which can lead to a huge amount of data; one has to keep in mind that every event typically contains a whole "hit pattern", i. e. the ordinal numbers of the responding strips as well as their pulse heights. As already pointed out in chapter 3, the interesting quantities connected with such an event are

- the number of fragments and the fragment species (or masses, respectively),
- the position of the center-of-mass,
- the KER in transversal direction (or $\varepsilon^{\perp}$, to be precise),

- the positions of the individual fragments, if possible, in order to extract fragmentation geometries,

- furthermore: time after injection, electron collision energy etc.,

and all these quantities characterise a *single* event. Hence, these values have to be determined in an event-by-event analysis. Afterwards, they can be analyzed statistically.

All the interesting quantities – as long as they are not measured independently, like the time after injection, or derived from independently measured variable, like the electron collision energy – can be obtained from the fragment masses and the impact positions. However, the assignment of this geometrical arrangement is sometimes ambiguous, as already discussed in section 4.1. On the other hand, by choosing *some* possible assignment, one would in any case obtain the correct center-of-mass position and $\varepsilon^{\perp}$, since these quantities are independent of the interpretation of the hit pattern, i. e. any valid interpretation would yield the same values (see section 4.1). The advantage of assigning fragment masses is that the chemical branching ratios can be extracted, although the results may be slightly influenced by the misassignments discussed. Their effect, however, can be estimated, e. g. by using a simulation, and the results can be corrected and a systematical error can be stated. Furthermore, it is necessary to determine the fragment masses in order to distinguish between different fragmentation channels. Hence, it is indispensable to interpret the hit pattern in terms of fragment masses in a well defined way.

The event-by-event analysis procedure which interprets the raw data in terms of fragment masses and impact positions will be referred to as *event reconstruction* and can be subdivided into two steps:

- the signal of each responding strip is assigned to an integer number representing a mass (*mass assignment*), which in some cases may represent that of several incident particles;

- the thus obtained hit pattern (strip numbers and the masses assigned in the first step) is interpreted in terms of fragment masses and impact positions (*fragment assignment*).

Mass assignment

The masses of the fragments are to a very good approximation integer multiples of the atomic mass unit, and the precise masses are usually not needed for the analysis[4] (and can actually not be determined with the EMU detector). The reconstruction of the KER is limited by uncertainties in the impact positions (strip width) and the overlap lenght of electron and ion beam anyway. Thus, it makes sense to use integer numbers for the masses involved.

The mass recorded by a strip is usually the mass of all fragments hitting the strip (for the case of signal splitting see below). Hence, different peaks corresponding to the masses of the fragments and all possible sums of fragment masses are seen in the pulse height spectrum (see fig. 4.9). The smallest pulses correspond to the mass of the lightest fragment, and the largest pulses belong to the mass of the whole molecule. Since in DR a breakup of the molecule is always expected, the latter case can only happen if all fragments hit the same strip (either horizontally or vertically).[5] This is normally much less probable than hitting different strips, and consequently the peak corresponding to the total mass is smaller than the other peaks.

Once the masses corresponding to the peaks in the pulse height spectrum are known, it is possible to define *mass windows* along the pulse height axis, with each of the windows containing a single peak. In the event-by-event analysis, each pulse which falls within one of the mass windows is identified with the corresponding mass, using integers for the denomination. This procedure will be called *mass assignment* in the following; the outcome is the hit pattern, as already defined in section 4.1. It should be stressed again that at this stage there is not yet any assignment of masses for the individual fragments.

Beyond the case demonstrated in fig. 4.9, it can happen that the charge carriers of one fragment are collected by two neighbouring strips, especially when the fragment is hitting a gap or the edge of a strip (when the impact position is projected to the back side; gap hits on the front side are probably not seen; see chapter 5). This effect is enhanced by diffusion in the transversal direction. The two strips share the total signal of the same fragment in basically any ratio. Thus, pulses are generated which can lie outside the mass windows. In many cases, however, it is possible to reconstruct the signal by adding the pulse heights of

[4] For simulations of raw data, however, the precise masses are taken into account.

[5] For heavier systems with masses around 30 u, however, neutralization in residual gas collisions without breakup have been observed.

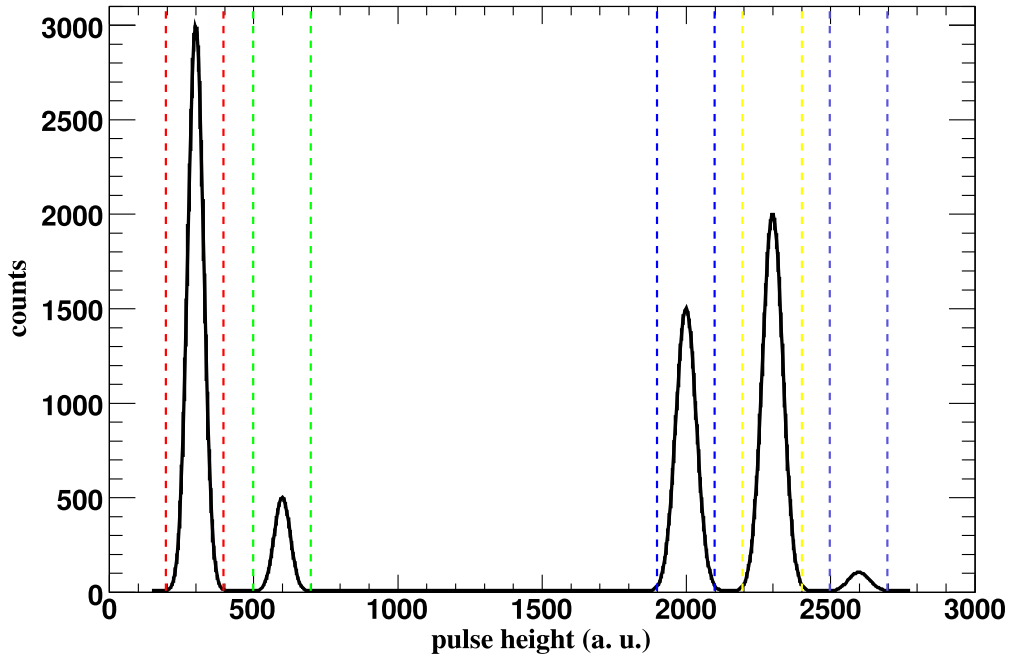

Figure 4.9: Schematic depiction of a pulse height spectrum on a single strip obtained from fragments of the generic ion A_2B^+ (e. g. D_2N^+) with $m_A < m_B$, assuming that the fragments A, B, AB, and A_2 are produced. A possible choice of the "mass windows" is given by the vertical dashed lines. The corresponding masses are: m_A (red), $2m_A$ (green), m_B (blue), $m_B + m_A$ (yellow), and $m_B + 2m_A$ (purple). Note that these masses are not necessarily the masses of single fragments, but that they correspond to the total mass of all fragments hitting the same strip in a single event. Such a pulse height spectrum is obtained by accumulating pulses for many events.

the two neighbouring strips.

The mass assignment is then conducted in two stages (see fig. 4.10): In a first attempt, the pulse heights of all answering strips are compared towards the mass windows. If they lie within a mass window, the corresponding mass is assigned to that strip. At the second stage, all strips with mass signals that could not yet be assigned are compared among each other with respect to their sequence number. If they are adjacent, their pulse heights are added and the sum is compared with the mass windows. If it lies within a mass window, the corresponding mass is assigned to the strip with the larger signal. Since the signal of the answering strips can also be caused by noise, the procedure is applied only for strips

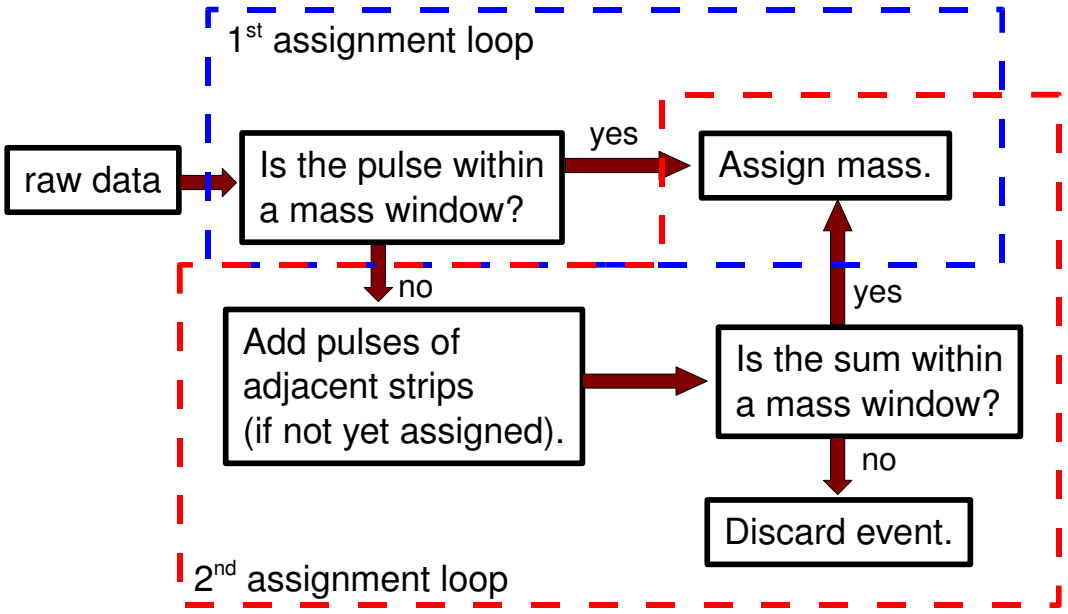

Figure 4.10: Schematic visualization of the mass assignment procedure. The first loop is applied for all responding strips in an event. The pulses that could be assigned are not considered in the second loop, which is executed after the first loop is finished.

with pulse heights above a software threshold value that can be chosen accordingly. This means that those signals which are split in such a way that almost the whole signal appears at one strip (but not enough to be still in the mass window) and whose remaining portion is below the threshold are not assigned, and therefore the event has to be discarded. For this reason, the mass assignment ends with a check for strips with pulse heights *above* the threshold not assigned to any mass; if there are any, the event is discarded.

Obviously, there is a chance that a signal is split between two strips in such a way that the two proportions fall into mass windows. E. g. in the DR of $DCND^+$ one would have – among others – mass windows for masses 28 (DCN or D + CN on the same strip), 26 (CN), and 2 (D). The signal of a DCN (28) can split such that masses 2 and 26 are seen on neighbouring strips. However, the same pattern can be obtained from real fragments CN + D. Therefore, two fragment configurations can lead to the same hit pattern, and consequently the two events cannot be distinguished! Hence, in a small number of events a

similar ambiguity occurs as by L-shaped events (see section 4.1). The mass identification procedure, however, always leads to the explanation using two separate fragments, as shown in fig. 4.10.

Fragment assignment

The next step in the event reconstruction is the interpretation of the hit pattern in terms of fragment masses and impact positions. This is described in detail in appendix A. Only the important cornerstones of this procedure are mentioned here.

Obviously, a valid interpretation is only possible if the total masses on front and back side of the detector (i. e. the sum of the masses of the vertical and the horizontal strips) are the same. If not, the event is discarded.

If the total masses of front and back side are the same, the individual masses recorded by the strips of front and back side are compared. If the same masses occur on strips on the front and on the back side, these strips are assigned to the same fragment, i. e. the corresponding mass is interpreted as the mass of a fragment, whose position is given by the two strips. (This assignment is not necessarily unique, as e. g. in fig. 4.3.) However, the masses do not always appear pair-wise, e. g. when two fragments hit the same strip. In that case, the number of responding strips on the side where the double hit occurs is the number of fragments minus one, and no fragment has yet be assigned to the strip with the double hit. On the other side two strips ahave not yet received a fragment assignment. The sum of their masses equals the mass of the strip with the double hit. If this condition is found to be fulfilled, the masses and positions of the remaining two fragments are obtained (see example in fig. 4.2, where a double hit on a horizontal strip is shown).

The situation gets more complicated, if there are more strips with multiple hits, especially if there are multiple hits on both front *and* back side (e. g. L-shaped events with fragments of *different* mass in the corners, like the one shown in fig. A.4). The different techniques that are successively and/or alternatively used in order to try an assignment in these cases are explained in appendix A.

It should be pointed out that complicated hit patterns like multiple L-shaped structures represent rather exotic cases and that in the great majority of all events the fragments hit different strips on both front and back side, or a double hit on a single strip occurs, and the assignment is straightforward. For small polyatomic ions the number of fragments is

typically ≤ 3 (see examples in this thesis, chapters 5 and 6), i. e. the most complicated hit pattern is a simple L-shaped event. It seems therefore not necessary at the present stage to implement an even more sophisticated event reconstruction routine.

The coordinates of the impact positions are given by the respective strip numbers. The width of the strips represents the uncertainty of the impact positions. It is not possible to use only the strip numbers as coordinates in the further analysis (e. g. to determine the distance of impact positions), since that would mean the replacement of a continuous variable by a discrete variable, resulting in binning problems. Therefore, a position on the strip (including the gap) is chosen randomly by adding a random number between 0 and 1 to the strip number and storing the result as a floating point value.

Every *event* is now labeled according to the outcome of the fragment identification. The label distinguishes between

- invalid events, i. e. events where the mass assignment or fragment identification failed,
- valid events which could not be related to a DR channel, e. g. DE events, and
- DR events with each fragmentation channel being assigned a unique label.

This label allows to pick only events of interest in the following analysis.

One last example shall demonstrate the limits of the event reconstruction procedure in exceptional cases (see fig. 4.11). Consider the DR of CHD^+. One possible fragmentation channel would be C + H + D. The signal of the D (mass 2) can be split between two horizontal strips in the ratio 1:1, i. e. mass 1 is seen on two adjacent horizontal strips. Consequently, all responding strips of this event are assigned to existing mass windows in the first stage of the mass assignment process. In the subsequent fragment assignment, this hit pattern is interpreted as an event with a C and an H on their own strips, and two additional hydrogen fragments on the same vertical strip and on adjacent horizontal strips. This is a valid event, since all strips can be assigned to mass windows, the total masses on front and back side of the detector are the same, and the hit pattern can be interpreted in terms of fragment masses and impact positions. However, it would not be recognized as a DR event, since the number of fragments and fragment species obtained that way do obviously not correspond to a decay channel of CHD^+. One has to be cautious with the interpretation of such an event: It could be that the beam does not only contain CHD^+, but also some contamination of CH_3^+, and one would get events which are actually C + H

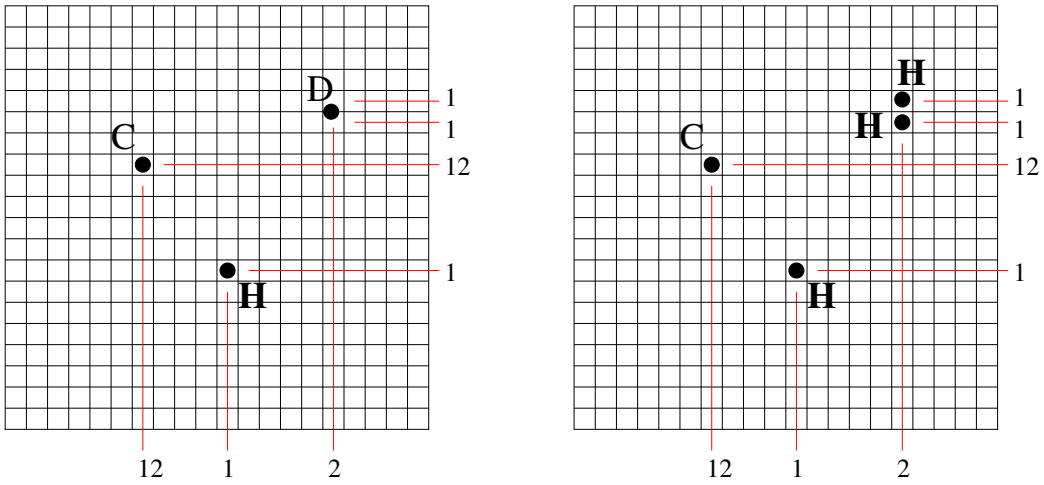

Figure 4.11: A case of *signal splitting*, where the hit pattern can be interpreted as a decay channel of a different ion. Although the fragments are produced in the DR of CHD^+ (left), it seems that there are three hydrogen atoms, suggesting that the fragments are produced from CH_3^+ (right).

+ H + H. On the other hand, if one knows that the event must be stemming from CHD^+, one can say that a misassignment must have occured and count it as a DR event. The event reconstruction procedure, however, identifies such an event as C + H + H + H by virtue of its design.

This example shows that there is no perfect event reconstruction procedure covering all special cases that can occur, since the event reconstruction is always following the philosophy that is applied during data analysis. For this reason, one has to make sure that priority is given to the most important interpretation of ambiguous events. Obviously, the two events in fig. 4.11 cannot be distinguished by the detector, and in some sense, the interpretation depends on what one *expects* to see in that case. E. g. one could change the mass assignment procedure in such a way that the signals of neighbouring strips are always added before they are compared against the mass windows. In that case one would get the correct interpretation of the above mentioned event, but one would misassign events with hits of fragments on adjacent strips. The probability to get such a signal splitting is in the order of a few percent (see chapter 5), and the probability to get a splitting in the ratio 1:1 (or in any ratio that results in two pulses within existing mass windows) is much lower. It is therefore probably better to leave the procedure as it is instead of dropping the separation between mass assignment and fragment assignment, as explained above in this

section, leading in that case to a preference of the explanation without signal splitting.

Data format, data processing, and analysis

The event reconstruction and data analysis routines are written in C^{++} and rely heavily on the ROOT framework [62]. ROOT offers a data structure called *TTree* (or simply *tree*). Among the advantages of using trees are structured storage of the variables, internal data compression, and fast access. A tree is divided in different *branches*. The variables assigned to a branch are called *leafs*. Each entry in a tree corresponds to an EMU event, and each variable has its own branch, while some branches contain arrays. Three different trees are used:

1. a tree containing the raw data (branches for number of responding strips, ordinal numbers of responding strips, pulse heights, and other relevant information, like time after injection);

2. a tree containing the outcome of the event reconstruction (branches for number of fragments, fragment masses, fragment positions (as floating point values), the label characterising the event, and other data which are just copied from the raw data tree);

3. a tree containing center-of-mass positions and – in the newest version of the analysis software – $\varepsilon^{\perp}$.

The tree containing the raw data is obtained by translating the original raw data file, which is in ASCII format, into a tree. In this step, the pulse heights of the different strips are cross-normalized such that for all strips the same ADC channel corresponds to the same fragment energy. It proves to be sufficient to describe the relation by a first order polynomial, i. e. a gradient and an offset obtained from the measured peak positions of data that were not subjected to the cross-normalization procedure. All further steps are conducted using a graphical user interface (GUI) called *EMU_GUI* (fig. 4.12). First, the mass assignment and fragment assignment are performed (event reconstruction), and the resulting tree is stored in a separate file. After this, the positions of the center-of-mass are calculated from the fragment positions (as floating point numbers), and the corresponding tree is stored again in its own file. Besides the calculation of $\varepsilon^{\perp}$, the center-of-mass position is used for diagnostics of the phase-space cooling of the ion beam and for cuts on the data

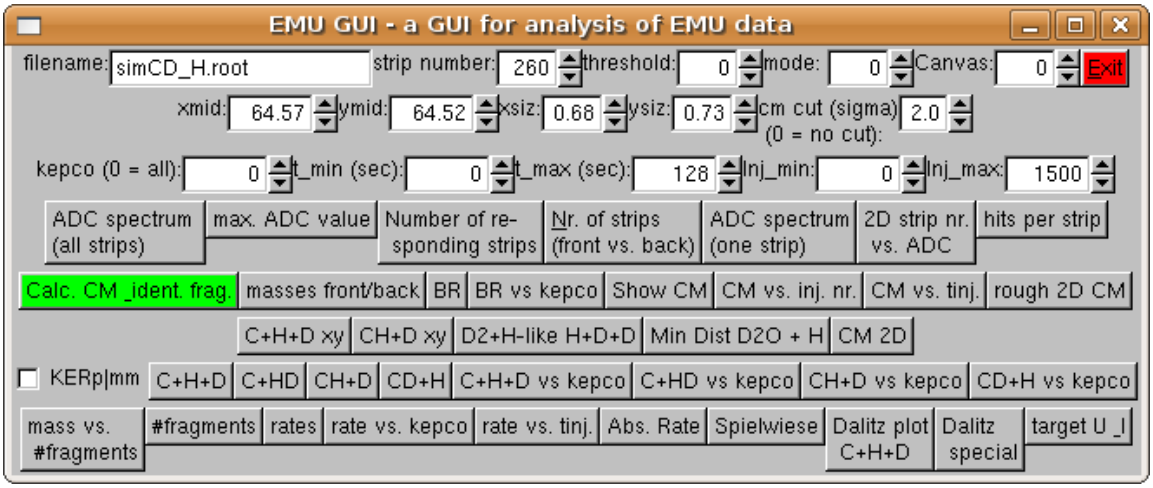

Figure 4.12: The *EMU_GUI*, written by H. Buhr and the author. The appearance changed many times – here a current version is shown. Note that some buttons have to be adapted to the ion under investigation and to the different decay channels, respectively. The green button performs the event reconstruction, consisting of the mass assignment and the fragment assignment, followed by the calculation of the center-of-mass positions.

in order to suppress possible background. It is only calculated for DR events, since for all other events (DE, collisions with residual gas) a sharp center-of-mass position is not expected and shall not be used as a criterion.

In the analysis the events are usually filtered according to specific requirements. Any variable in one of the branches can be used for that purpose. Assume that a histogram containing distances of the impact positions of the fragments in a specific decay channel with two fragments is required. First, one would filter out all events with the label assigned to the decay channel. These events are then filtered by their center-of-mass position. For the remaining events, the distance can easily be calculated from the impact positions. Further conditions can be established, e. g. regarding the time of the occurrence of the event with respect to the time of the injection of the beam (contained in the raw data tree). Each of these analysis queries are possible without reading the events completely into memory, allowing for faster access to the data.

4.4 Concluding remarks on the performance of the EMU detector

The goals and the working principle of the EMU detector have now been discussed in detail. Although from its idea and layout it comes close to an "all-in-one device suitable for every purpose", some performance limits have also to be pointed out, and its capabilities should be put into context.

The EMU detector is the first mass sensitive fragment imaging detector used in a DR experiment, and it is therefore the only device so far to perform fragmentation channel specific imaging on small polyatomic ions in a storage ring experiment without far-reaching limitations to specific systems. This capability is limited by the mass resolution between heavier fragments, to be discussed in the remaining chapters. The analysis procedure described so far assumes that the mass windows do not overlap, i. e. that the mass peaks in the pulse height spectrum are clearly separated. An example where this is not the case any more will be discussed in chapter 6.

A strength of the EMU detector is certainly the fact that it can perform 2D imaging measurements with a rate of up to approximately 2 kHz, as compared to $\sim$ 100 Hz for CCD based imaging systems. This allows to study more questions in the same time, while statistics is much better. In addition, the detector allows to combine imaging measurements with determination of the branching ratios, i. e. two measurements which have always be done separately can now be performed *simultaneously*. As a surplus, the data quality can easily be monitored due to the various information included in the data. One example is the distribution of the center-of-mass, which helps to judge the quality of the phase-space cooling. Thus, the EMU detector combines 2D fragment imaging capability with the important concept of a new branching ratio detector.

These applications are further studied in the next chapters, where the performance and also the performance limits are further pinned down. A possible further application, which is beyond the scope of this thesis, is the measurement of reaction cross sections. Suffice it to say that currently the maximum readout rate limits this possibility.

5 Dissociative recombination of CHD^+

5.1 Introduction

Given the complexity and the innovative concept of the EMU detector, its capabilities have been explored and the necessary analysis procedures have been developed stepwise in a series of beamtimes with appropriate ions. As a first proof-of-concept experiment following the setup of the detector, the DR of the relatively simple ion D_2H^+ has been studied. The results are presented in [59] and shall not be repeated here. The ion CHD^+ is discussed instead in order to illustrate the performance of the EMU detector.

As compared to D_2H^+, CHD^+ has the advantage to produce heavier fragments up to mass 14 (CD). Since their nuclear charge is higher than for the light fragments, they are expected to behave differently as they penetrate the detector material. It is especially important to know if not only masses 1, 2, and 3 can be distinguished, but also how good the mass resolution is between masses 12 to 15.

5.2 Experiment and results

5.2.1 Pulse height spectra

The experiment has been performed with a CHD^+ beam at a beam energy of 6.22 MeV. After injection into the TSR, the beam was cooled with the photocathode-produced electron beam in the electron target section. In some runs, the electron cooler has been used in addition.

Pulse height spectra for front and back side of the detector are shown in fig. 5.1. The spectra of the individual strips have been 'calibrated' (cross-normalized) such that the peaks fall on top of each other. The calibration data are based on the measurements performed so far (as of fall 2009). The ions investigated to date are listed in table 5.1.

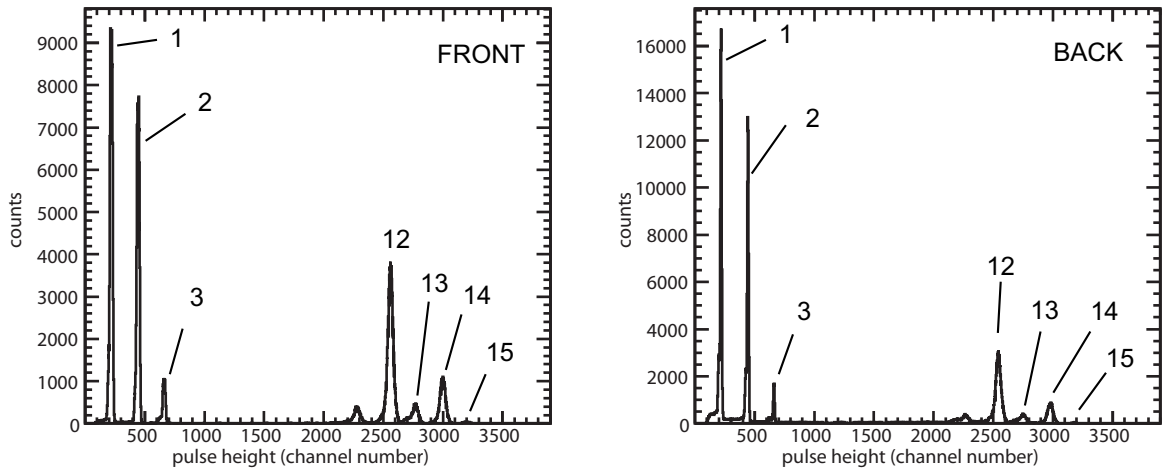

Figure 5.1: Calibrated pulse height spectra for the front (left) and the back side (right) of the detector. The pulse height is in ADC channel numbers obtained from the MDI-2 VME unit.

Ion	Data	References
D_2H^+	June and July 2008	[59]
CF^+	November 2008	
CHD^+	November 2008	
D_3O^+	December 2008	[63, 64]
$DCND^+$	January 2009	
DCO^+	November 2009	
D_2HO^+	December 2009	

Table 5.1: Ions already investigated with the EMU detector.

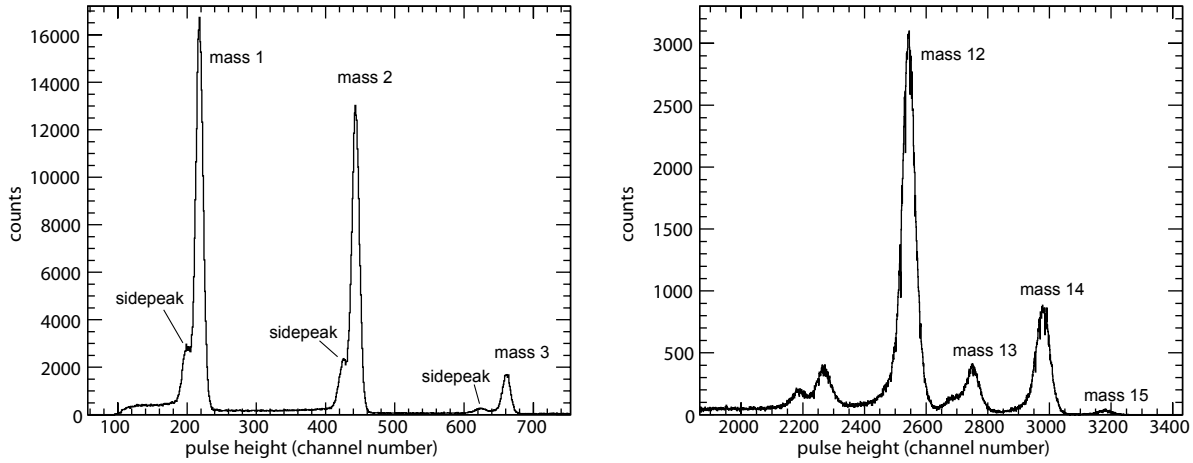

Figure 5.2: Detailed views of the low energy (left) and high energy (right) regions of the back side spectrum, showing the "side peaks" and a constant "background" due to events with signal splitting.

Fig. 5.2 shows a detailed view of both the low-mass peaks (masses 1, 2, 3) and the high-mass region (masses 12 to 15) of the pulse height spectrum of the back side. The low-mass peaks are clearly separated, and there is no problem to distinguish the different masses and chose the mass windows accordingly. On the other hand, two features are seen which complicate the analysis:

- Each peak has a smaller "side peak" at lower peak height. For masses 1 and 2, the side peak almost completely overlaps with the main peak, whereas for mass 3 the peaks are placed just next to each other.
- The space between the peaks is also filled with events. They are distributed as a constant "background" between two peaks, and the background level rises below each peak.

Looking at the high energy region, more peaks than expected are found. The small peak at mass 15 is expected due to hits of all DR fragments on the same strip, which can happen, although it is rather unlikely. This is the reason why the peak is so small. Starting from there, the masses 12, 13 and 14 (C; CH, or C and H on the same strip; CD, or C and D on the same strip) can be assigned to peaks which are equidistantly distributed, as shown in fig. 5.2 (right). However, there are additional peaks between masses 12 and 13 (overlapping

with the mass 13 peak) and below the mass 12 peak. Furthermore, it can be seen that there is no "background" above mass 15.

The interpretation is as follows: The side peaks are due to hits of the strip edges with the increased dead layer (see also fig. 4.6). The energy that is lost in this layer cannot contribute to the ionization signal, resulting in smaller peak heights. It can be seen that the distance to the main peak rises with increasing fragment mass. This can be explained with a higher energy loss in the dead layer due to the increased nuclear charge – the ionisation density rises. The high-energy peaks must also have side peaks, and this is the reason why the actual number of peaks exceeds the expected one. The peak between masses 12 and 13 must be one of them, and so is the double peak structure below mass 12 (at around 2200). Since the side peak must be considerably smaller than the main peak (about 15 % of the events should be in the side peak), this can only be the mass 12 side peak. However, it is unclear why there is a smaller peak in the double peak structure at even lower energies. It could be that the thicknesses for the entrance windows at the strip edges differ slightly for the different strips, leading to different energy losses. The side peaks of the other masses (> 12) accidentially overlap with other main peaks and can therefore not be seen.

This rises the question how the side peaks affect the event reconstruction. Should there be windows defined for them, and what happens if they overlap with main peaks, like in the high mass region? If the windows are chosen such that the side peaks fit in the windows of the main peaks, there is no problem at all. This can be achieved for the low mass peaks. In the high energy region, however, where side peaks overlap with other main peaks, a pulse can fall into a mass window although it would belong to a side peak and therefore corresponds to a *higher* mass. On the other hand, the identification of a DR event requires that the *whole mass of the entire molecule* is detected. The missing mass for such a side peak event would mean that – if the event is a DR event and only DR events are of interest – the event is discarded due to wrong total mass. For CHD^+ there is exactly one heavy fragment in each possible DR channel (C, CH, or CD), and therefore the possibility that the event is discarded for that reason does not depend on the fragmentation channel, i. e. even a determination of branching ratios would be possible without paying attention to that problem. However, one should be careful if one is interested in DE channels!

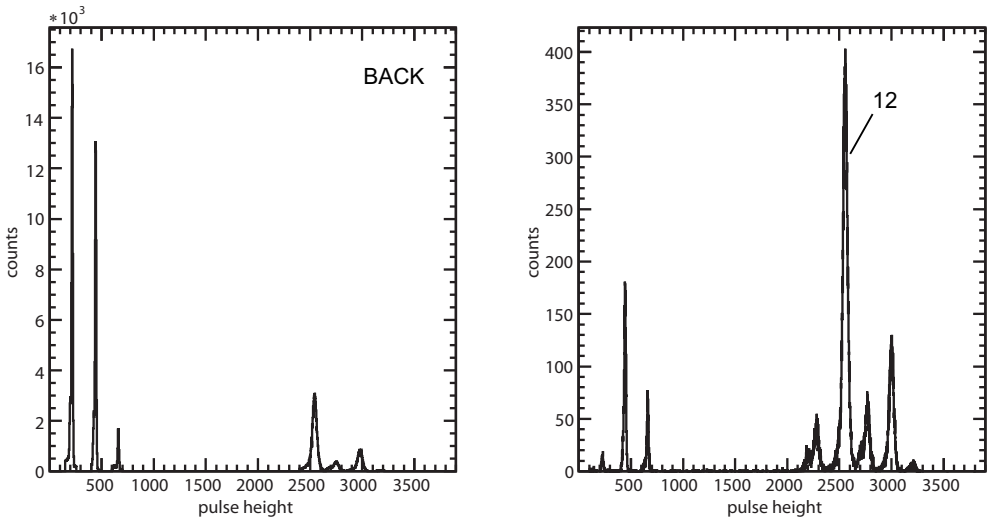

Figure 5.3: Pulse height spectra for pulses within mass windows (left) and for the *added* pulse heights for adjacent strips, whereas the individual pulse heights are outside the mass windows (right), for the back side of the detector. The appearence of the peaks in the right spectrum proves the signal splitting hypothesis.

5.2.2 Signal splitting

The "background" of pulses between the peaks is a possible hint for signal splitting, i. e. the charge carriers produced by a fragment are collected by two strips. These pulses are not seen in runs without ion beam, which means that they are related to hits of real fragments. The flat distribution of these pulses shows that the signal can be split between the strips in any ratio. Note that the level rises *below* each peak and that there are no events above the mass 15 peak.

In order to prove the signal-splitting hypothesis, the pulses outside the mass windows have been added for neighbouring strips. Figs. 5.3 and 5.4 show pulse height spectra for pulses within mass windows and for added pulses which where outside the mass windows and on adjacent strips before addition. It can be seen that the pulse height sums form again the different peaks corresponding to the different fragment masses, as can be seen at the back side of the detector. Even the side peaks are visible. The effect is much weaker on the front side[1]. Whereas the low-mass peaks are clearly seen and can easily be assigned,

[1]This is seen for the peaks corresponding to high masses, which are lower. For the low mass peaks signal splitting cannot contribute so much due to the threshold below the mass 1 peak at 50.

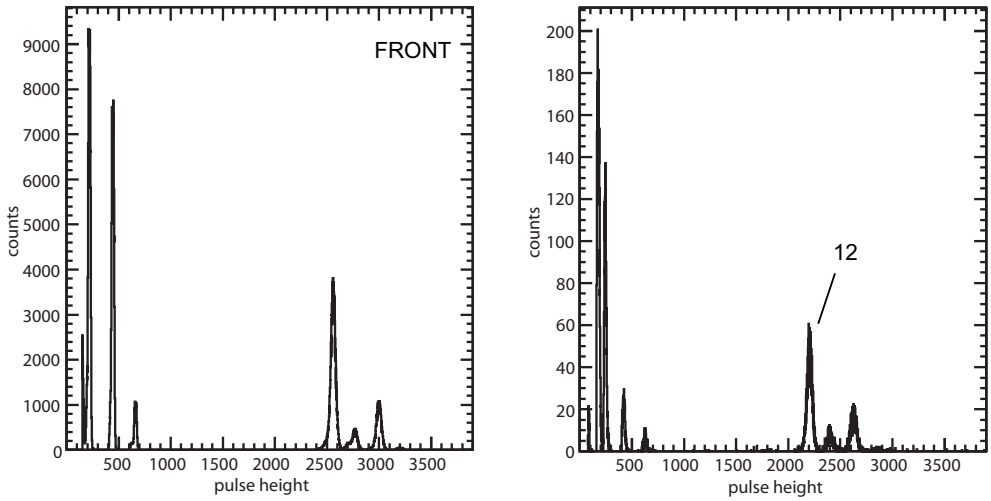

Figure 5.4: The same as fig. 5.3, but now for the front side. Note that the signal splitting effect is much weaker here (mass 12 peak about a factor of 7 lower than for the back side) and that the high-mass peaks are shifted.

since they appear at about the same positions, the peaks in the high energy region are shifted towards lower pulse heights. E. g. the mass 12 peak is now at about 2200 instead of 2550. This can be explained in two ways: Either the signal splitting affects hits in the gaps between strips, and the collection efficiency for the charge carriers is probably much lower there, especially for heavy fragments which do not penetrate the detector material so deeply, resulting in lower pulse heights due to recombination of electrons and holes, or the gap hits are not seen at all, and signal splitting on the front side is an issue for hits at the strip edges where they experience an non-observable energy loss, and therefore the added signals appear in the side peaks. The fact that the positions of the shifted peaks in fig. 5.4 agree well with the side positions of the side peaks (as far as they are visible) supports the latter interpretation.

It is obvious that the strong effect at the back side is due to the long diffusion paths of the charge carriers, which are produced close to the front surface and spread over a larger region transversally while they travel to the back side. By adding pulse heights outside the mass windows for adjacent strips, additional events can be identified. However, the procedure obviously fails for the front side due to the shifted high-mass peaks (although it works for the low-mass peaks). Since the effect is negligible there and affects only pulses

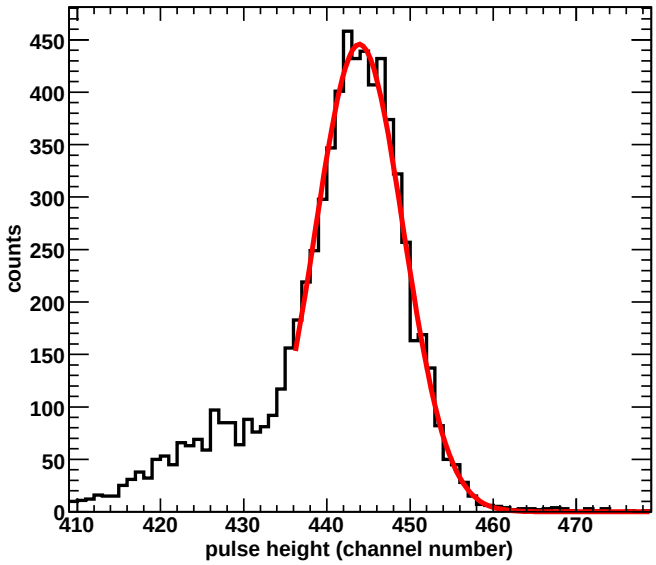

Figure 5.5: The mass 2 peak, including its side peak, for one single strip close to the center of the detector on the back side (strip number 63). The width of the main peak alone is 12.5 channels FWHM, corresponding to an energy resolution of 23 keV for deuterons with a kinetic energy of 830 keV.

which would without signal splitting lie in the side peaks anyway, this is not considered to be a problem.

5.2.3 Mass resolution

It can be seen that the mass resolution depends on the fragments (see fig. 5.2). For the fragments with high mass, the resolution is obviously worse. The average number of electron-hole pairs created in the detector by a fragment is approximately proportional to its kinetic energy, i. e. the high energy peaks correspond to a larger number of charge carriers and therefore show a larger width. In addition, the energy loss experienced in the entrance window is larger for the heavy fragments; thus, the energy deposited in the active volume of the detector is scattered over a larger range.

An order-of-magnitude statement about the performance of the detector regarding the mass resolution can be gained from the mass 2 peak (fig. 5.5). The width is about 23 keV for 830 keV deuterons. For the mass 12 peak, the FWHM is about 100 keV. However, this peak could be broadened by the overlapping mass 13 side peak.

5.2.4 Event reconstruction

The event reconstruction has been performed as explained in chapter 4. From the 403895 events in the file (run 51), 249814 events are identified as DR events in the channels

- CD + H,
- CH + D,
- C + HD, and
- C + H + D.

In addition, 96 events are found which can be interpreted as "CHD", i. e. in about 0.4 % of the DR events all fragments hit the same "pixel", i. e. the same strip both in horizontal and vertical direction, if it is assumed that a breakup will always occur.

Surprisingly, some events are found which are interpreted as "C + 3H". Since they were found to amount up to more than one percent of the DR events, this rises the question whether the beam consisted of or contained some contamination of CH_3^+.[2] However, almost all of these events can be explained with signal splitting. E. g. two mass 1 fragments (H) are found on the same vertical strip (front side) and on two adjacent horizontal strips (back side). This can also be interpreted as a mass 2 fragment (D), whose signal is split with the ratio 1:1 between the two adjacent strips. Such events show a strong asymmetry between front and back side (splitting effect is higher on back side). Very few events with mass 1 particles on adjacent strips at both sides are found, which can be explained as signal splitting on both detector sides. Altogether, there is no evidence for "real" C + 3H events.

5.2.5 Center-of-mass

Fig. 5.6 shows the evolution of the center-of-mass in time. It can be seen that the shutter, which protects the detector during injection, opens at about 5.5 s after injection and closes at about 13.5 s. After about 8 s, the cooling process is finished. The time interval between 8 s and 13 s is used for time cuts.

Fig. 5.7 shows the center-of-mass distribution for the time interval between 8 and 13 s. The distribution has a very sharp peak, indicating that the result of the phase-space cooling

[2] The four-body breakup is energetically forbidden at 0 eV collision energy. These events can only come from collisions with the residual gas.

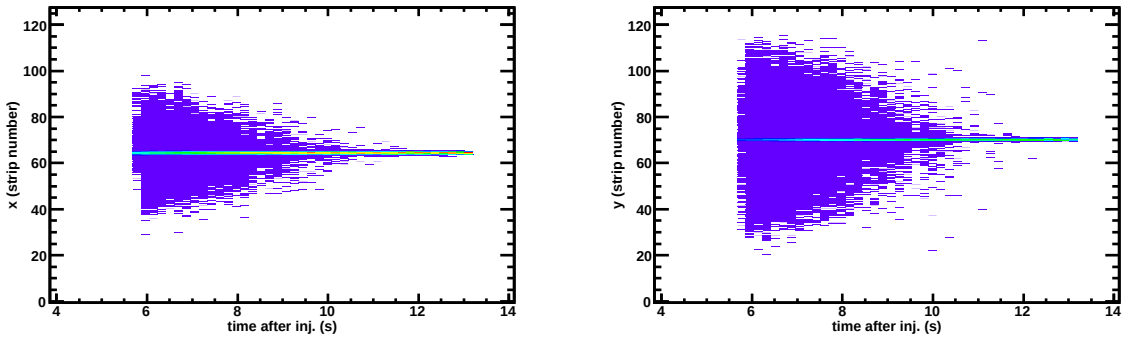

Figure 5.6: The time evolution of the center-of-mass distribution in x (left) and y (right). The content of each time bin has been normalized in order to show only the cooling effect and not the decay of the beam.

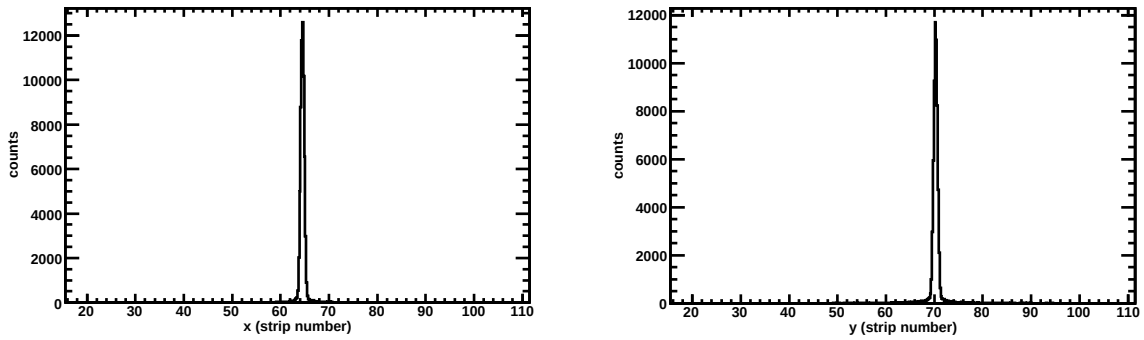

Figure 5.7: The center-of-mass distribution between 8 s and 13 s in x (left) and y (right).

Channel	Br. Ratio (%)
C + HD	8.65(0.12)
CD + H	20.14(0.17)
CH + D	6.78(0.10)
C + H + D	64.43(0.20)

Table 5.2: Branching ratios, obtained by counting events in each channel, without any correction of detector effects. Errors are statistical errors only.

is a well cooled beam. The width is about 1.4 strips FWHM ($\approx 1\,\mathrm{mm}$). An elliptical area corresponding to a 2σ deviation from the maximum is chosen as cut area. Only events inside this cut region are considered in the further analysis.

5.2.6 Distribution of fragments

The different fragmentation channels can be distinguished after the event reconstruction. One interesting question would be how the fragments are distributed over the detector area. Since there are no channels with two fragments of the same mass, the impact positions can be determined unambiguously for all channels and all fragments.

Fragment distributions for all four channels are shown in fig. 5.8. Time and center-of-mass cuts have already been applied. The most critical channel is CD + H, since it has the largest "explosion cone". However, the edge of the distribution is well away from the detector edges. No geometrical losses are expected in that case.

5.2.7 Branching ratios

Since the different channels can be distinguished, it is possible to deduce branching ratios by counting the events in each channel. The results are shown in table 5.2. Note that the errors stated there are purely statistical, as given by a multinomial distribution. However, detector effects and the limitations of the event reconstruction procedure dominate the overall error.

In order to account for systematic effects, a simulation[3] is used, which takes detector effects such as signal splitting and side peaks partly into account. Simulated data files,

[3] developed mainly by H. Buhr, and based on techniques presented in [48]

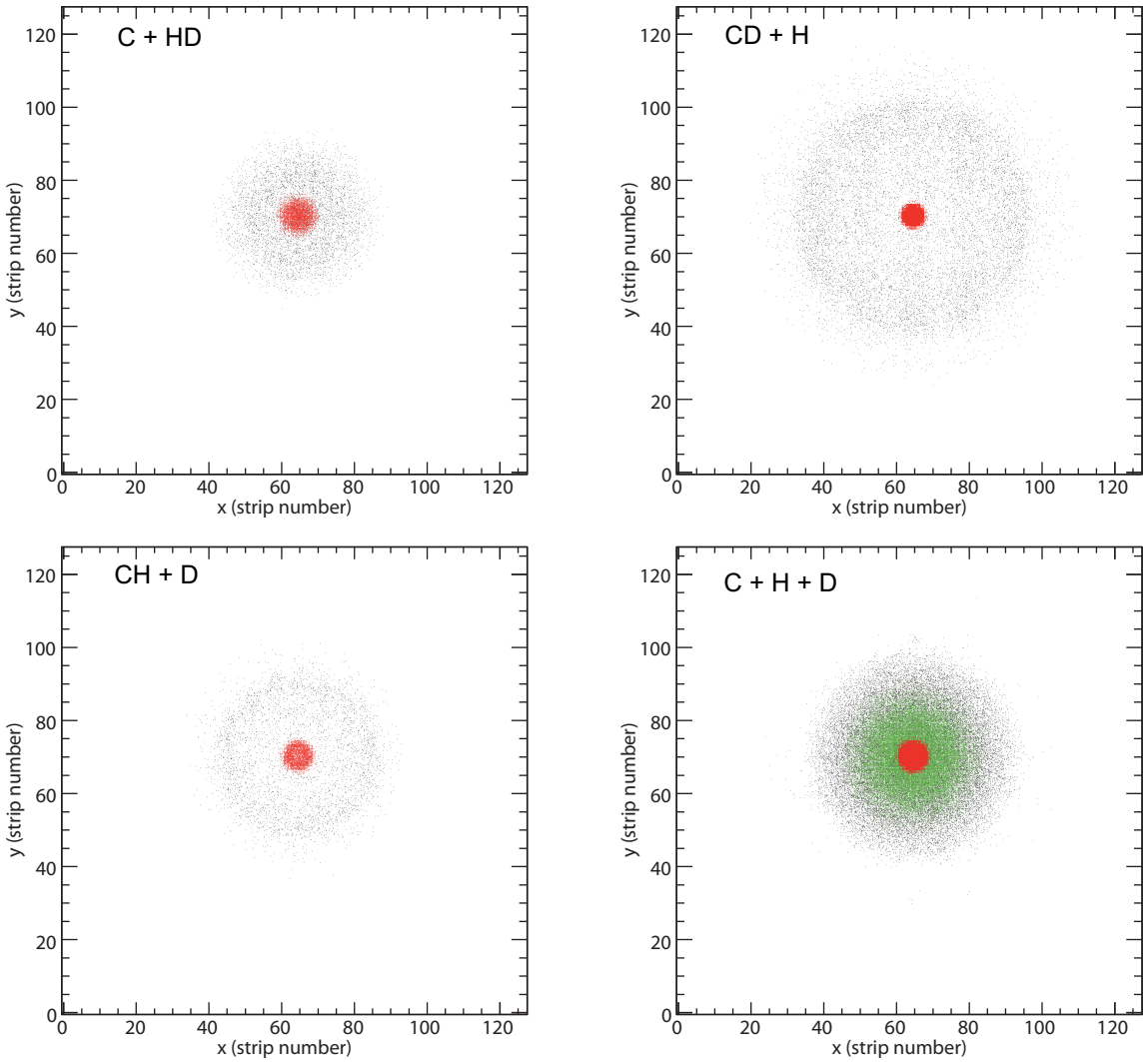

Figure 5.8: Distribution of fragments on the detector for four different channels. The heaviest fragment is always in red, the lightest in black. Note that not all hits can be seen, since they are partly shadowed, especially by the red area in the center.

C + H + D:

Channel	Br. Ratio (%)
C + HD	0.06
CD + H	0.21
CH + D	0.05
C + H + D	99.68

C + HD:

Channel	Br. Ratio (%)
C + HD	98.02
CD + H	0.00
CH + D	0.00
C + H + D	1.98

CD + H:

Channel	Br. Ratio (%)
C + HD	0.00
CD + H	99.28
CH + D	0.00
C + H + D	0.72

CH + D:

Channel	Br. Ratio (%)
C + HD	0.00
CD + H	0.00
CH + D	97.79
C + H + D	2.21

Table 5.3: Branching ratios that have been "measured" for the simulated decay channels, showing the order of magnitude of false assignments, which can be about 2 % in this example. Each table shows branching ratios obtained with the EMU analysis software for a simulated data set containing only the corresponding channel as input.

CHD^+:

Channel	Br. Ratio (%)
C + HD	8.79
CD + H	20.15
CH + D	6.90
C + H + D	64.16

CH_2^+ [65]:

Channel	Br. Ratio (%)
C + H_2	12(2)
CH + H	25(4)
C + H + H	63(6)

Table 5.4: The corrected branching ratios measured with the EMU detector, compared with the branching ratios for CH_2^+ [65]. Systematical errors for the EMU results are estimated to be around 1–2 % (absolute error of percentage).

each of them containing only events from one single channel, are analysed with the same software that is used in the analysis of real data. However, some assumptions have to be made in order to make the simulation as realistic as possible. Isotropic angular distributions as well as uncorrelated breakup of the three-body channel are assumed, and reasonable assumptions have to be made about the energy distribution of the fragments (i. e. their internal excitation, affecting the KER). These information can partly be extracted from the measured data. E. g. the 3-body channel was assumed to show about 50 % population of each of the two states with C(^3P) and C(^1D), respectively [66], while for the 2-body channels very simple energy distributions have been assumed, which reproduce the cone sizes shown in fig. 5.8 very well. The results for the branching ratios obtained from the analysis of pure simulated channels are shown in table 5.3. It can be seen that about 98 % of the events are correctly identified. However, these results depend on many parameters, like the choice of the mass windows. Due to the imperfection of the model of the detector employed in the simulation, the results should be regarded with care. Nevertheless, such a simulation can be used in order to correct the measured data for misassignments. The data in table 5.3 provide a linear relation between measured and real branching ratios. By exploiting this relation, a correction of the measured data can be obtained. The results are shown in table 5.4, where they are also compared to the DR branching ratios for CH_2^+ [65]. The systematical errors are estimated to be around 1–2 % (absolute error of percentage).

An interesting aspect of the results in table 5.2 is the strong isotope effect. The number of events going to CD + H is about three times as high as the number going to CH + D. Although the D is more tightly bound than the H due to a lower zero-point energy, such a strong effect is surprising. However, a similar result has been obtained for the DR of D_2H^+ in another recent experiment with the EMU detector [59]. These results are of interest due to the observed enhancement of deuterium in molecules and the detection of multiple deuterated species in the interstellar medium [67].

The analysis of the DR of CHD^+ is not yet finished. Once the detailed distributions of the excitation energies of the fragments are understood, the simulation can be improved. A further question which has still to be studied in more detail concerns the possibility of contaminations with other ions (e. g. CH_3^+, NH^+).

5.3 Conclusions

The data from the DR of CHD^+ at 6.22 MeV give a feeling for the performance of the detector. The mass resolution is superb for light fragments like H and D, and it is still good enough to distinguish between masses 13 (CH) and 14 (CD) with kinetic energies of 5.4 MeV and 5.8 MeV, respectively. One concern would be the occurrence of side peaks due to different thicknesses of the entrance window. This can result in the "loss" of a fragment if its signal does not fall in a mass window, or a wrong mass can be assigned if it falls into one of the other mass windows. For DR events only, this would lead to the rejection of the event. One has to make sure that the rejection probability due to this problem is about the same for all channels if one wants to determine branching ratios, or the effect has to be taken into account otherwise. For CHD^+, every DR channel has exactly one heavy fragment (C, CH, CD), and the side peaks for them are outside the corresponding mass windows. If it is assumed that the probability to end up in a side peak does not depend on the fragment (it should not, since it is caused by the detector geometry), this leads to the same rejection probability for all DR channels.

Another critical point is "signal splitting". This can lead to wrong event identifications, like the one shown in fig. 4.11. Such events show a strong asymmetry between front and back side: It is much more likely that the signal splits between two strips at the back side. Whenever a feature is related to such events and a difference between front and back side is seen, it should be regarded as an artefact.

These effects can partly be accounted for using a Monte-Carlo simulation, which is still under development. Such a simulation is especially important for the determination of branching ratios with high accuracy. The branching ratios for CHD^+ show a strong isotope effect: The probability that the H is ejected in the two-body decay is almost three times as high as the ejection probability for the D.

6 Dissociative recombination of $DCND^+$

6.1 Isomers in space – a challenge for contemporary astrochemistry

One of the most puzzling and challenging problems in contemporary astrochemistry is the HNC/HCN abundance ratio observed in dense interstellar clouds. In order to explain the unusually high abundance of the less stable HNC it has been proposed already in 1974 that both molecules are produced *with about the same efficiency* in the dissociative recombination of $HCNH^+$ [3]. Thus, the observed *abundance ratios* would strongly depend on the DR *branching ratios*. However, the experimental confirmation of this hypothesis is still absent. There is only one published work by Amano *et al.* [68] (see the discussion at the end of this section), which provides at least some experimental evidence pointing in that direction.

The $J = 1 - 0$ transition of the linear molecule hydrogen cyanide (H−C≡N) at 88.6 GHz has been observed in June 1970 in different interstellar sources, among them Orion A and Sgr A [69]. Hydrogen isocyanide (H−N≡C) has been detected a few years later [70]. In the model of interstellar chemistry established by Herbst and Klemperer [22], the main formation mechanism of HCN is dissociative recombination of H_2CN^+:

$$H_2CN^+ + e^- \longrightarrow HCN + H,$$

assuming that this yields HCN only, although they mention the possibility to obtain HNC as well. Pearson and Schaefer [71] showed that the structure of H_2CN^+ in its electronic ground state is linear ($H-CN-H^+$). This suggests the possibility of producing HNC via

the reaction

$$HCNH^+ + e^- \longrightarrow HNC + H,$$

which was first clearly stated by Watson [3]. He concluded from his model (including also other chemical reactions involving ions) that the abundance ratio for these isomers should be mainly determined by the efficiencies of their production in DR.

The abundances of HCN and HNC have been measured for different astrophysical environments. The abundance ratios [HNC]/[HCN] are of the order of one for most dense clouds. Results as high as 4.4 in L134 have been reported [72].[1] Such high values are typically observed in cold environments with temperatures of $\sim$ 10 K. In slightly hotter places like OMC-1[2] the ratio is between 0.01 and 1 [74].

These abundance ratios are surprising, since HNC lies energetically about 0.63 eV higher than HCN [71, 75, 76]. In a thermochemically equilibrated system, where collisions and reactions lead to isomeric changes, one would expect to find only a negligible abundance of HNC with respect to HCN. On the other hand, the potential barrier between the two minima in the triatomic potential energy surface of H/C/N has a height of about 1.31 eV from the HNC side (1.26 eV to the first delocalized state below the barrier) [75] and strongly suppresses any spontaneous isomerization to HCN. If Watson's suggestion is correct and a considerable amount of HNC is produced in the DR of $HCNH^+$, it could survive for a long time. The detection of $HCNH^+$ in the 1980s [77] is a further hint supporting the proposed production mechanism of the two isomers.

The first attempt to predict branching ratios for the DR of $HCNH^+$ theoretically is the statistical phase-space model by E. Herbst [15]. He obtained an HNC/HCN ratio of 0.9, supporting the assumption that both isomers have similar production efficiencies. However, he predicted that in 50 % of the events the fragment CN is produced, whereas experimentally a lower fraction of 33 % was measured [76].

Towards the end of the 1990s, several papers have been published that took advantage of the progress in the application of modern quantum chemical methods. Talbi and Ellinger [78] calculated adiabatic and quasi-diabatic potential energy surfaces for N-H and C-H bond dissociation, corresponding to the production of HCN and HNC, respectively, while the geometry of the other atoms was fixed. They found that the lowest dissociative states of

[1] However, these high values have recently been put into question [73].
[2] OMC: Orion Molecular Cloud

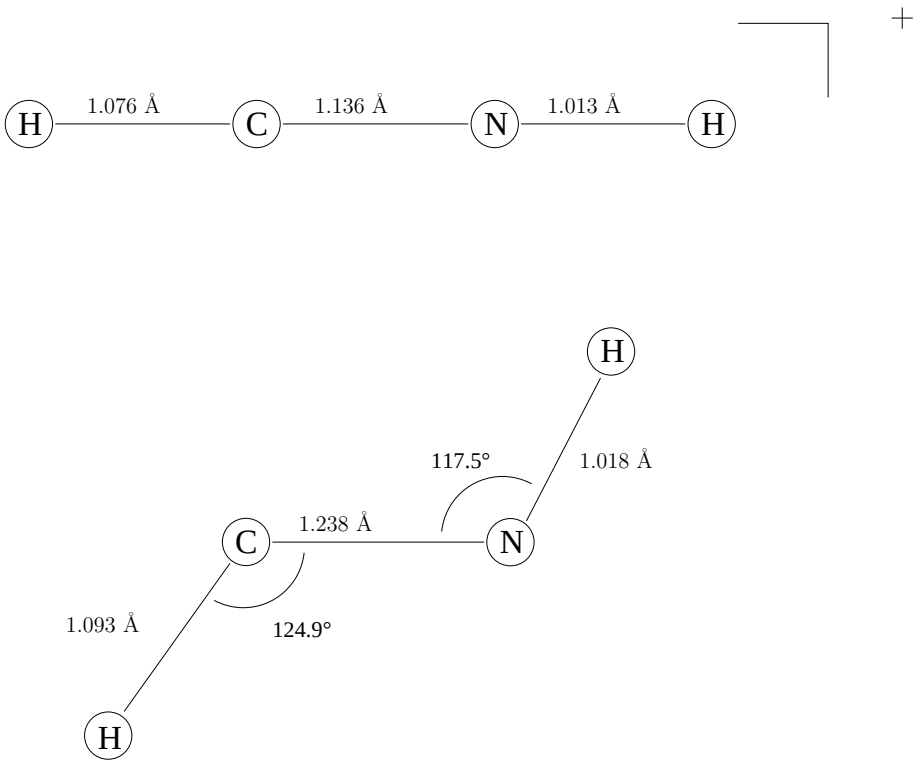

Figure 6.1: Ground state equilibrium geometries for $HCNH^+$ and HCNH [79].

$^2\Sigma^+$ symmetry cross the ionic ground state close to the minimum, below the first vibrational level. They concluded that the direct process should be very efficient for both N-H and C-H dissociation, leading to an equal formation of HCN and HNC. In the indirect process (and by virtue of the procedure applied in the calculation of the potentials), the nuclear geometry should be weakly perturbed (apart from the separation of the H atom), letting low vibrational product excitation appear likely. The indirect process is supposed to be strongly suppressed due to the efficiency of the direct channel; regarding the branching ratio, the indirect process would lead to about the same probabilities for the production of the two fragments as well.

A similar approach has been followed by Shiba *et al.* [79], but the results are quite different. They also found $^2\Sigma^+$ states resulting in C-H and N-H bond dissociation, but their two-dimensional diabatic potential energy surfaces do not cross the ground state surface of the ion; instead they lie well below. Consequently, they proposed an indirect dissociation mechanism, where the wavefunction after electron capture collapses in a coherent non-

radiative way through the Rydberg states below the ionic ground state, until non-adiabatic couplings are strong enough and the molecule dissociates via one of the repulsive states. Alternatively, radiative relaxation down the Rydberg ladder could be important. They concluded that the HNC/HCN branching ratio should be of the order of one with a slightly higher preference for the production of HNC. The indirect path should produce considerable vibrational excitation in various degrees of freedom of the molecular system.

In both papers, the conclusions are based on the geometries of the involved potential energy surfaces. However, both approaches do not in a very detailed way consider the dynamics of the dissociation process. Therefore, Tachikawa used a different approach in order to elucidate the reaction mechanism [80]. Starting from the $HCNH^+$ ion in the equilibrium geometry of its ground state, he chose in a first step the initial velocities of the atoms according to a temperature of 10 K and calculated classical trajectories, yielding the classical Franck-Condon region. For 50 different configurations of the ion obtained that way, he considered in a second step "vertical" electron capture and followed the subsequent trajectories of the atoms by solving the classical Hamiltonian equations of motion while assuming the potential energy surface of ground state HCNH. Some trajectories lead to the dissociation into HNC + H within less than 0.1 ps. On the other hand, most trajectories form a "long-lived HCNH complex" with a lifetime of more than 2 ps, which might dissociate later (indirect process). Tachikawa's work leaves many questions open and even contradicts some of the results obtained otherwise. For example, he obtains only the two channels HNC + H and the HCNH complex, but not channels with the fragments HCN or CN. Nevertheless, his results are very interesting, since they show that the fragments are produced in vibrationally excited states. Especially the long lived complex can show a large bending motion. The average translational energies found in the direct dissociation channel account for only 40 % of the available energy.

Recently, some updated results have been published. Hickman *et al.* [81] confirmed the results of Talbi and Ellinger and calculated rates for the channels HCN + H and HNC + H, which are found to be of the same order of magnitude. Ishii *et al.* [82] performed a wave packet dynamics study based on their previous findings (Shiba *et al.*). Their conclusion concerning the branching ratios, however, confirms again the results anticipated by Hickman *et al.* In summary, all these theoretical studies came to the conclusion that the production of both isomers happens with about the same probability, while they were not able to agree about the electron capture and subsequent dissociation mechanism. However, they were

Channel	Max. KER (eV)	Branching Ratio
HCN(HNC) + H	5.9(5.3)	0.675 ± 0.016
CN + H + H	0.6	0.325 ± 0.032
CN + H_2	5.1	0 ± 0.017

Table 6.1: Maximum KERs and experimental results on the branching ratios for the different decay channels in the DR of $HCNH^+$ [76]. Note that HCN and HNC could not be distinguished in the CRYRING experiment.

still yielding valuable hints to the importance of microscopic reaction mechanisms for the outcome of astrochemical reaction chains.

Compared to the effort put into these questions by theory, there are only few published experiments about the DR of $HCNH^+$. The most important one is certainly a study at CRYRING in 2001 [76]. Both the branching ratios at 0 eV collision energy and the absolute cross section between 0.01 meV and 0.2 eV have been measured. Since the branching ratios have been determined using the grid method, which is essentially implementing a mass spectroscopical observation, it was not possible to distinguish between HCN and HNC. The results are shown in table 6.1. The channel CN + H_2 does not seem to be present at all. This would be expected from the linear structure of the $HCNH^+$ molecule, where the two hydrogen atoms are attached to the CN by different bonds at opposite sides. It can be stated that – somewhat different from the prediction by Herbst [15] of 50 % for the three-body channel – the two-body decays are dominant, whereas the three-body channel (CN + H + H) occurs only in one third of the events. The energy dependence of the cross section ($\propto E^{-1.13}$) between 0.1 and 40 meV deviates from what is expected from the direct process ($\propto E^{-1}$). This indicates that the indirect process could be involved, although it is not excluded that the direct process might still be the more efficient one.

Recently, the DR of $HCNH^+$ and $DCND^+$ has been studied in an extended negative glow discharge [68]. Rotational transitions have been detected for different vibrational states of the products. In these spectroscopic observations, it was found that the [HNC]/[HCN] ratio is 1/3, whereas the [DNC]/[DCN] ratio was found to be 2/3 with an estimated uncertainty of 20 %. The vibrational temperature for the stretching modes of HNC was about 2200 K, compared to 400 K for the bending mode. The corresponding values for HCN were 2000 K for the ν_1 mode, 600 K for the bending mode, and 1300 K for the ν_3 mode. However, the following aspects should be born in mind interpreting these observations:

- HCN and HNC can also be produced in neutral-neutral reactions. The authors claim that this should be a minor contribution since the experiments have been performed at liquid nitrogen temperature. However, they cannot completely exclude the possibility of a contribution from the neutral reaction channel.

- The role of collisional isomerization at pressures of more than 15 mTorr is unclear. The different ratios for HNC/HCN and DNC/DCN could indicate that this isomerization path might be important.

- It is not clear how much time the fragments had to relax following the DR, but since HCN and HNC have large dipole moments, radiative relaxation can be very efficient. The vibrational excitation directly following the formation of HCN/HNC may well be higher than found in equilibrium.

It is therefore not possible to infer that the measured abundance ratios directly reflect the DR branching ratios, and that the situation in such a discharge experiment simulates the conditions in cold dense clouds sufficiently well in order to draw conclusions about their chemical properties.

6.2 Experimental procedure

As in the experiment at CRYRING [76], the EMU detector is not able to obtain directly the HNC/HCN branching ratio, because it adopts a mass-spectroscopical fragment identification and can therefore not directly distinguish between HCN and HNC. However, it can measure kinetic energy releases and deduce statements about the energies of the internal states of the fragments. Since the decay channels HCN + H and HNC + H have different exothermicities (differing by about 0.63 eV), it could be possible to make a conclusion about the production of the isomers from the observed energy releases.

The experiment at the TSR has been performed with $DCND^+$ instead of $HCNH^+$ for two reasons:

- The maximum diameter for the circle that delimits the possible fragment impact positions at maximum KER for $DCND^+$ is about 10.5 cm for the ion beam energy of 3.01 MeV (assuming ground state ions and a maximum flight distance of 10 m) and thus only slightly exceeds the size of the detector (9.73 cm). Only a small part of the

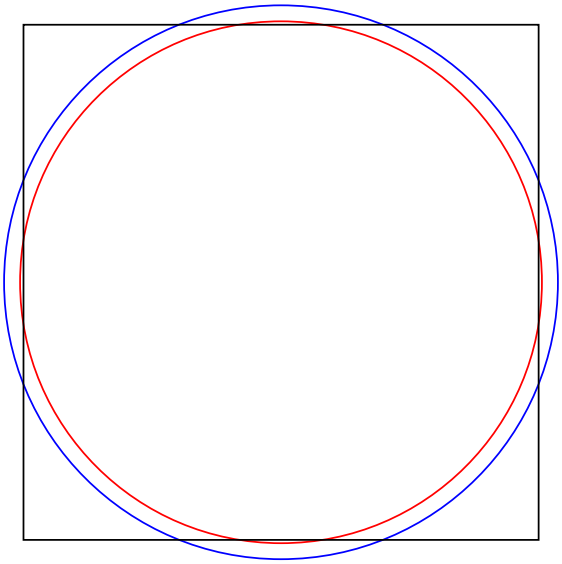

Figure 6.2: Comparison of the sizes of the EMU detector and the "explosion cone" for the most critical channel for the DR of $DCND^+$, which is DCN + D, assuming a maximum flight distance of 10 m (9.41 m to the center of the target, overlap of the two beams $\approx$ 1.2 m) and taking the beam energy of 3.01 MeV (blue). The red circle corresponds to a flight distance of 9.41 m. It is possible that some fragments miss the detector. However, the circles can be considerably smaller if the fragments are excited. On the other hand, any excitation of the parent ion and broadening of the center-of-mass due to imperfect phase space cooling would tend to increase the diameters.

fragments risks to be lost by this reason (see fig. 6.2). For $HCNH^+$, however, the size of the circle would be much larger.

- The peaks corresponding to masses 26 (CN) and 28 (DCN) in the pulse height spectrum have a considerable overlap (see fig. 6.9 and later discussion) and can be resolved only partially. Much less mass separation would exist for masses 26 (CN) and 27 (HCN) in the case of $HCNH^+$.

The ion was produced in a Penning source from a gas mixture of D_2 and completely deuterated acetonitrile ($D_3C{-}C{\equiv}N$) and accelerated to an energy of about 2 MeV in a Van-de-Graaff accelerator. The beam was then injected into the TSR and further accelerated by the rf cavity to the final energy of 3.01 MeV within $\approx$ 2 sec.

It turned out that $DCND^+$ was not the only ion that was produced by the source. According to the pulse height spectra, different ions have been observed at different times,

Ion	Mass (u)
NO^+	30.0006
DCO^+	30.0167
N_2D^+	30.0279
$DCND^+$	30.0390

Table 6.2: Masses of the relevant ion species. The nuclear masses have been taken from [84]. Electron masses are included.

which were tentatively identified as NO^+, N_2D^+, and DCO^+, all of them having masses around 30 like the desired ion $DCND^+$ (the masses are stated in table 6.2). It became apparent that the tiny mass differences between them (down to $\Delta m/m \approx 3.7 \cdot 10^{-4}$) were not sufficient to separate all of them at the separation magnet directly behind the source or in the transfer beamline (except for NO^+), and the acceptance of the TSR allowed to store them simultaneously. For that reason, a new mass specific acceleration scheme in the TSR had to be adopted, which allowed to extract the desired ion species sufficiently well [83].

Fig. 6.3 shows a Schottky spectrum of the beam after injection into the TSR. Three peaks are seen at different revolution frequencies. The differences of the revolution frequencies are related to the mass differences of the stored ions by $\frac{\Delta f}{f} = -\frac{1}{2}(1+\alpha)\frac{\Delta m}{m}$, with the momentum compaction factor α describing the change of the closed orbit length with the momentum. In the standard mode of the TSR the momentum compaction factor is $\alpha = 0.1$. From the measured frequencies follows $\Delta f/f \approx 2.01 \cdot 10^{-4}$ for two neighbouring lines in the Schottky spectrum (fig. 6.3), resulting in a mass difference of $\Delta m/m \approx 3.7 \cdot 10^{-4}$, which is in agreement with the masses of the ions $DCND^+$, N_2D^+ and DCO^+. The idea is to set the start frequency of the rf exactly to the revolution frequency of $DCND^+$. In fig. 6.4 the evolution of the longitudinal phase-space during the start phase of the acceleration process is shown, based on a simulation (performed by M. Grieser) and taking the measured Schottky spectrum into account. $\Delta f_0 = f_0 - f_s$ is the deviation of revolution frequency f_0 with respect to the revolution frequency of the *synchronous* particle f_s, $\Delta\phi = \phi - \phi_s$ is the deviation of the rf phase with respect to the rf phase of the synchronous particle, while the synchronous particle – as the name implies – is synchronous with the accelerating rf. Whether a particle is accelerated on a stable orbit or if it is lost during the acceleration process depends on its deviations Δf_0 and $\Delta\phi$. All particles that are accelerated are captured in a *bucket*, in which they experience a synchrotron motion. The line that separates the bucket from

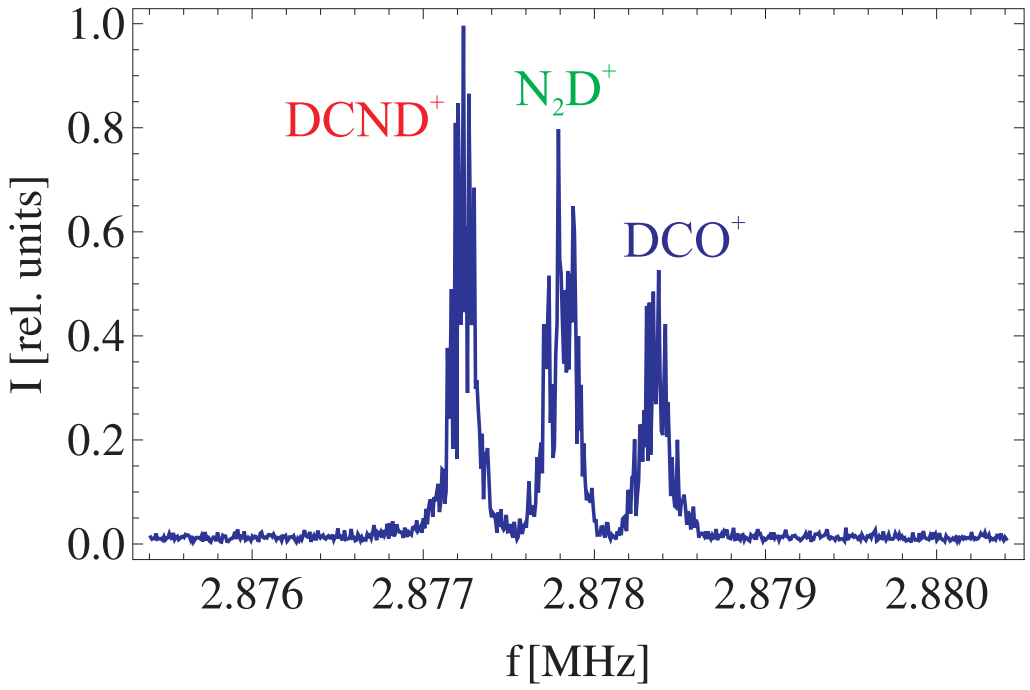

Figure 6.3: Schottky spectrum of the beam directly after injection (no electron cooling), taken at the 44^{th} harmonic [83]. It can be seen that the TSR is storing three different ion species at the same time. They can be distinguished by slightly different revolution frequencies. (Picture credit: M. Grieser)

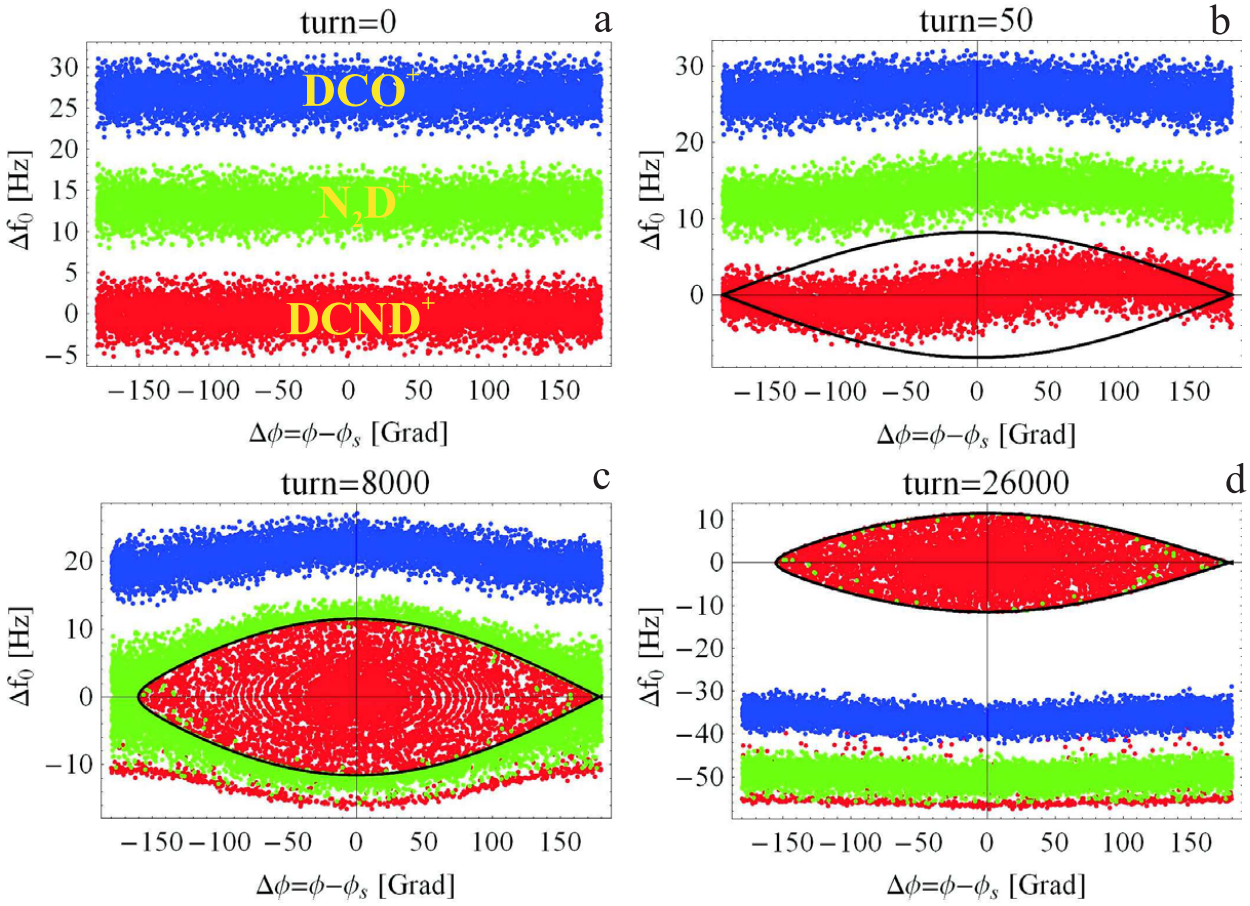

Figure 6.4: The evolution of the transversal phase-space at the beginning of the mass sensitive acceleration, obtained from a simulation [83]. The separatrix is shown as a black curve. The frequency f_0 is that defined to the nominal orbit in the magnetic field, which is ramped between the plots (a) to (d). See text for further explanations. (Picture credit: M. Grieser)

the part of the phase-space which is not accelerated is called *separatrix*. If accelerating frequencies and voltages are chosen accordingly, the bucket contains mainly $DCND^+$ and only a minor contribution of N_2D^+ ions. The sequence in fig. 6.4 shows how this bucket forms and is accelerated through the other beams at the beginning of the acceleration phase. This procedure is very sensitive to the initial energy of the beam, and any drift e. g. in the acceleration voltage of the electrostatic accelerator can change the finally selected ion species.

Apart from different ions, there is the possibility that the ion consists of the correct atoms, but in the wrong isomeric configuration. This has been discussed by Semaniak *et al.* [76]. They produced $HCNH^+$ in a hollow cathode-type ion source, operating at room temperature, by glow discharge ionization of CH_3CN gas, followed by a number of chemical reactions. In order to study the question whether another isomer can be produced, they calculated the energies for different states. In its ground state, which is of $X^1\Sigma^+$ symmetry, the ion has the linear $HCNH^+$ structure. The lowest $^1A_1$ state of the formaldehyde-like H_2CN^+, which is by 3.26 eV higher in energy than the ground state of $HCNH^+$, is unstable against isomerization into the linear form (without barrier). The triplet states are at least 5.3 eV above the ground state. All other states are even higher in energy. Hence, they concluded that – for thermodynamic reasons – other isomers should not be present in considerable amounts.

This argumentation should in principle also apply in the present experiment with $DCND^+$. However, the slightly different production process and possible differences in the source parameters should be kept in mind, and it cannot completely be excluded that some fraction of the isomers is in a different isomeric configuration. Especially, we cannot claim that the production process is understood, since in particular as the identified ions include even some species related to contamination of the source. On the other hand, the high excitation energies of other isomers are expected to lead to higher exothermicities for the different decay channels. If the observed KER is higher than expected, this could be a hint that higher energy isomers are present.

After the acceleration in the TSR, the beam was cooled in the electron target with a photocathode produced electron beam. The measurement started about 10 s after injection, i. e. after ≈ 8 s of precooling. During injection and acceleration of the beam, the detector was protected by a shutter (see also chapter 4), which was removed at the end of the precooling phase following each injection. The measurement cycle ended 20 s after injection

by placing the shutter again in front of the detector in order to prepare for a new injection cycle. For the results shown here, the electron beam remained at the electron energy for cooling throughout the measurement, i. e. the velocity of the electron beam always matched the ion beam velocity.

6.3 Data analysis and results

Selection of the correct ion species

As mentioned in section 6.2, the ion source produced different ion species, and in each injection three of them were injected into the TSR and stored simultaneously. However, not all of these ion species can be accelerated simultaneously in the subsequent acceleration phase. The simulation of the acceleration process (see fig. 6.4) shows that it is possible to extract basically only one ion species – given appropriate settings of the acceleration voltage and the start frequency (see also [83]). In order to prove that by changing the rf start frequency the different species can be selected and that the assignment shown in fig. 6.3 is correct, the recorded pulse height spectra have to be considered. Figs. 6.5 and 6.6 show pulse height spectra (only front side of the detector) obtained after acceleration with start frequencies set to the peaks labeled N_2D^+ and DCO^+, respectively, in the Schottky spectrum shown in fig. 6.3. These pulse height spectra have to be compared with the spectrum obtained by setting the start frequency to the value corresponding to $DCND^+$ (fig. 6.7). The most evident differences are the number of D atoms involved (peak at mass 4 for two D atoms), the double peak at mass 26/28 for $DCND^+$ (only one peak identifiable for the others), and the mass 12 peak for the carbon-containing ions (missing for N_2D^+). These differences are evidence for a clear separation of the different species during acceleration in the TSR.

However, since the spectrum of $DCND^+$ contains all relevant peaks (masses 2, 4, 12, 14, 16, 26, 28), it is possible that some contamination – especially by N_2D^+ – cannot be seen in the pulse height spectrum. The simulation (fig. 6.4) suggests that the contamination is negligible. However, a drift in the initial ion beam energy would change the conditions and could mix up the different ion species, if the starting frequency of the rf does not match any more the initial revolution frequency of the $DCND^+$. This has also been observed in the experiment. A first longer run (Run 000) took place the day after the mass specific

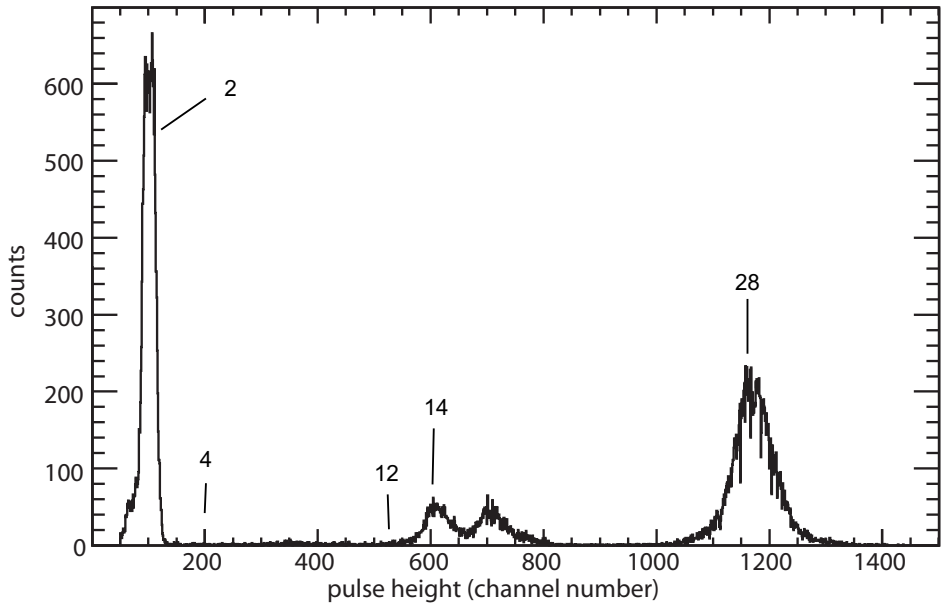

Figure 6.5: Pulse height spectrum recorded after acceleration of the ions corresponding to the central peak in fig. 6.3 (only front side of the detector). There are no peaks at masses 4 and 12, suggesting that only one D and no C are contained in the ion. Only one single peak is seen at mass 28 – there is no second peak attached to it, which would correspond to mass 26 (see fig. 6.7). The peak structure confirms the assumption that the ion species is N_2D^+.

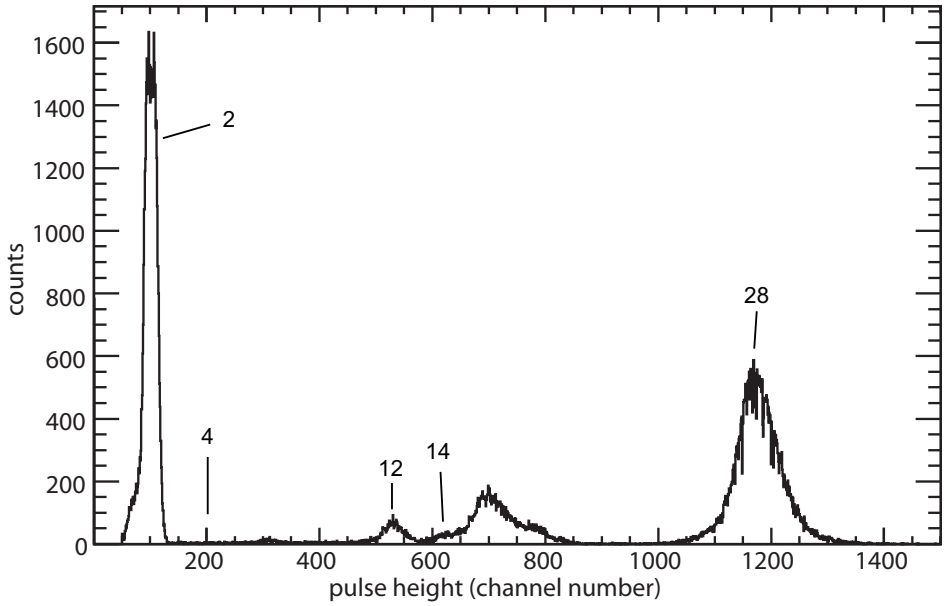

Figure 6.6: Pulse height spectrum recorded after acceleration of the ions corresponding to the right peak in fig. 6.3 (only front side of the detector). As in fig. 6.5, there is no peak at mass 4, indicating that the ion contains only one D atom. However, there is now a peak at mass 12, and the peak at mass 14 is considerably smaller (or consists only of the mass 16 side peak). The mass 12 peak is interpreted as carbon. As for N_2D^+, there is only a peak at mass 28 and no peak at mass 26. The pulse height spectrum confirms the assumption that the ion species is DCO^+. (Note that the mass 14 peak must stem from either DC or D and C on the same strip. The DR channel DC + O, however, is strongly suppressed. Data from a recent experiment are currently being analyzed [85].)

acceleration had been tested. After a second run (Run 001) in the afternoon, the experiment had to be suspended until the next day due to a technical problem. When the measurements were resumed, no attention has been payed to the rf settings, and only at the third day it was evident that the content of the beam had completely changed to N_2D^+. However, when analyzing the data, it could be seen that the conditions already changed in Run 001. For that reason, only the results of Run 000 are discussed comprehensively in the following, and the differences in the two runs are shown only when appropriate in order to justify the choice of Run 000. If not mentioned explicitly, all data shown are from Run 000. Under the given circumstances, hints for a possible contamination with N_2D^+ can only be obtained in retrospect once the data are analyzed.

Pulse height spectra for $DCND^+$

A pulse height spectrum for the front side of the detector is shown in fig. 6.7. The pulse heights of the individual strips have been cross-normalized in order to move the peaks on top of each other. This allows to use global mass windows, instead of defining them for each single strip separately.

A large peak at mass 2 (D) is seen, accompanied by a much smaller peak at mass 4 (D_2 or D + D on the same strip). At the other end of the spectrum (high masses), there is a double peak structure, made up of a large mass 28 peak (DCN/DNC, or CN + D on the same strip) and a smaller overlapping mass 26 peak (CN). A mass 30 peak (all fragments on the same strip) cannot be clearly seen. Since it is expected to be very small anyway, it is probably swallowed by the mass 28 peak. Since a breakup of the CN is energetically not allowed (see also table 6.1), further peaks in the pure DR spectrum are not expected. The structures between the low mass and the high mass peaks must be due to collisions with the residual gas and contain the side peaks of the mass 26/28 double peak structures, caused by hits at places on the detector where the entrance window is thicker.

Fig. 6.8 shows a pulse height spectrum of the back side of the detector. Because of imperfections of the calibration data, the mass 2 peaks of the different strips could not be moved on top of each other. For this reason, windows for mass 2 have been defined for each strip individually. Due to signal splitting, the space between the peaks is completely filled with pulses.

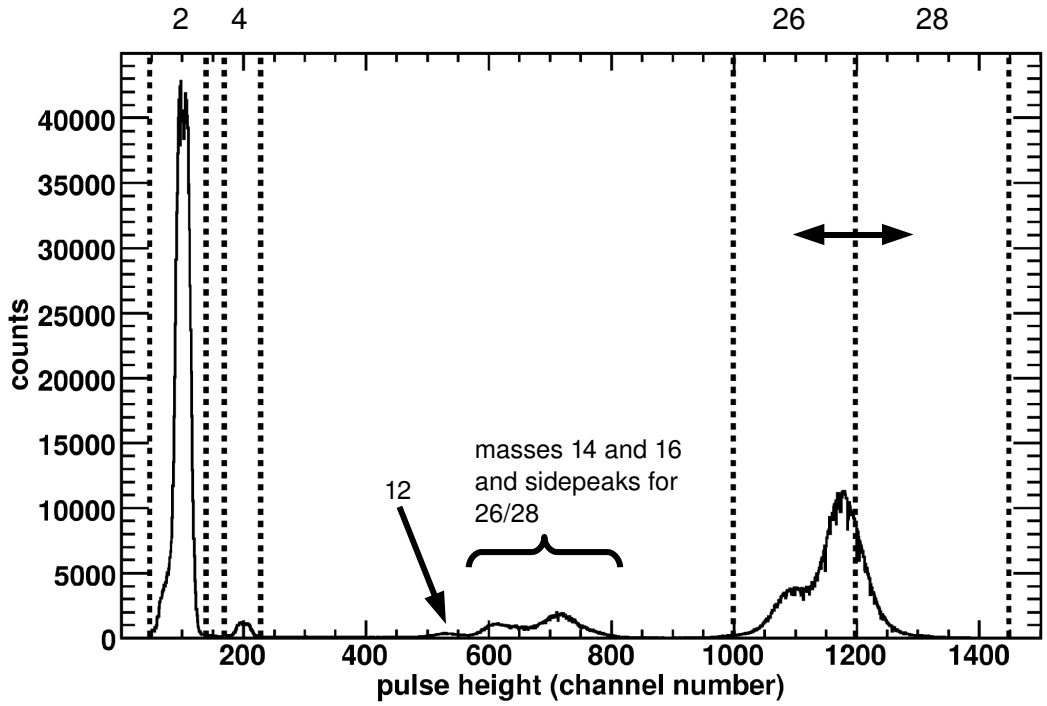

Figure 6.7: The 'calibrated' (cross-normalized) pulse height spectrum for the front side of the detector for 3.01 MeV $DCND^+$ ions. The borders of the mass windows for masses 2, 4, 26, and 28 are depicted by the vertical dashed lines. Note that the mass 26/28 peaks overlap, and that the border between the two mass windows is changed during the analysis in order to study the effect. (For the choice shown here, the mass 26 window covers almost the whole mass 26 peak, and only the right half of the mass 28 peak is within the corresponding window.) The ion species DCO^+ and N_2D^+ would not create peaks at mass 4 and – in the latter case – at mass 12. These two peaks together with the double peak at masses 26/28 are strong evidence for $DCND^+$.

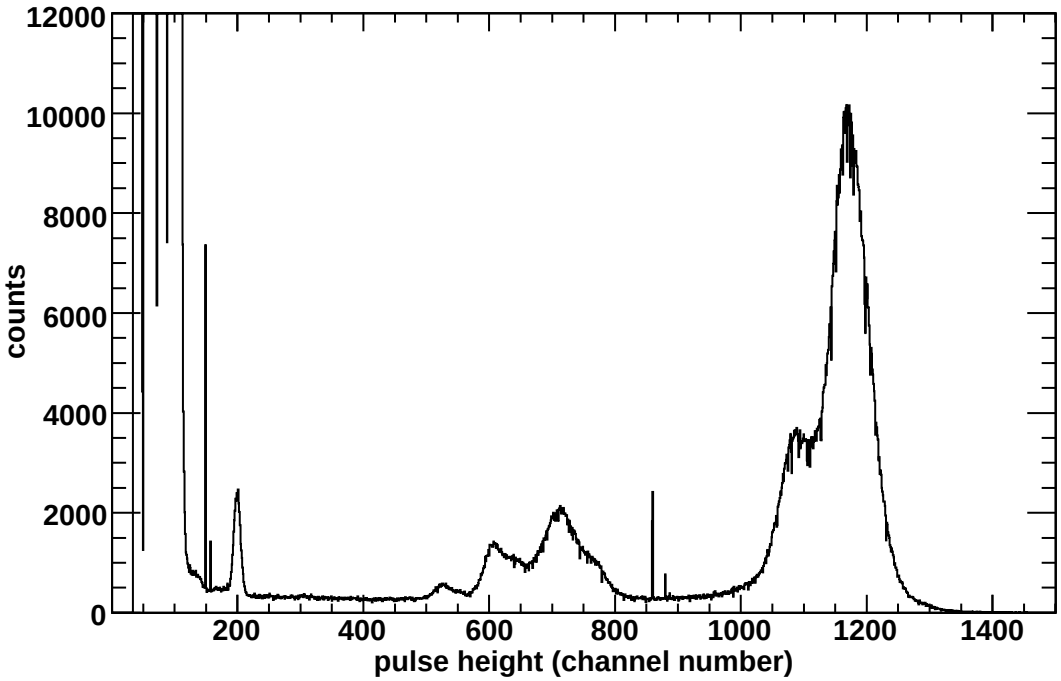

Figure 6.8: The 'calibrated' (cross-normalized) pulse height spectrum for the back side of the detector. Note that the view has been zoomed in and that the mass 2 peaks are mostly cut away. (The vertical lines in the left part below a pulse height of 100 are artefacts left over from the cross-normalization.) The relatively high "background" between the peaks is evidence for a strong signal splitting effect. The sharp spikes come from "noisy" events.

Event reconstruction

It would be desirable to define mass windows for all possible fragments from any dissociation process. However, this is hampered by the overlap of mass 26/28 side peaks with the peaks in the region mass 12 to 16. On the other hand, in order to account for DR fragments at 0 eV collision energy, only windows for masses 2, 4, 26 and 28 are needed, since a breakup of CN is energetically forbidden. In the further analysis presented in this thesis, only these four windows have been used.[3] A further complication comes from the mass 26/28 double peak. The standard event reconstruction procedure requires clearly separated peaks, because in the mass assignment only one definite mass is assigned to a measured pulse height. The mass windows cannot overlap for that reason and have to be chosen in a way that they cover some part of the respective peak. Different window sizes are investigated in order to study the influence of this choice.

In the following discussions, the windows for masses 2 and 4 are not changed, and so are the "left" (low energy) border of the mass 26 window at channel 1000 and the "right" (high energy) border of the mass 28 window at 1450 (neglecting the small mass 30 peak, which therefore lies within the mass 28 window). This border is moved far out in order to cover the whole high energy tail of the mass 28 peak. The range from 1000 to 1450 is subdivided into two windows, and the border between them is varied as described later (see fig. 6.9).

The outcome of the event reconstruction procedure obviously depends on the choice of the mass windows. Considering only the DCN/DNC + D channel, the masses that can occur are 2, 28, and 30. A mass 30 window is not used, i. e. only the mass 2 and mass 28 windows are needed. Furthermore, the identification of this channel requires one mass 28 fragment and exactly *one* mass 2 fragment *in coincidence*. Even if mass 28 is wrongly assigned to a mass 26 fragment, the three-body channel (CN + D + D) cannot be interpreted as DCN/DNC + D, since there are *two* mass 2 fragments.[4] CN + D events, however, which could possibly be formed in collisions with the residual gas, or events where one D is not detected for some reason, are erroneously interpreted as DCN + D if the mass 28 window is covering also the mass 26 peak. On the other hand, a conservative

[3] There should be a fifth window for mass 30. However, since a peak is not clearly visible, such a mass window has not been used. For that reason, events with all fragments on one strip, either vertical or horizontal, are discarded.

[4] There is of course still the possibility of L-shaped events with the two D in the corners, which would be interpreted as DCN/DNC + D anyway.

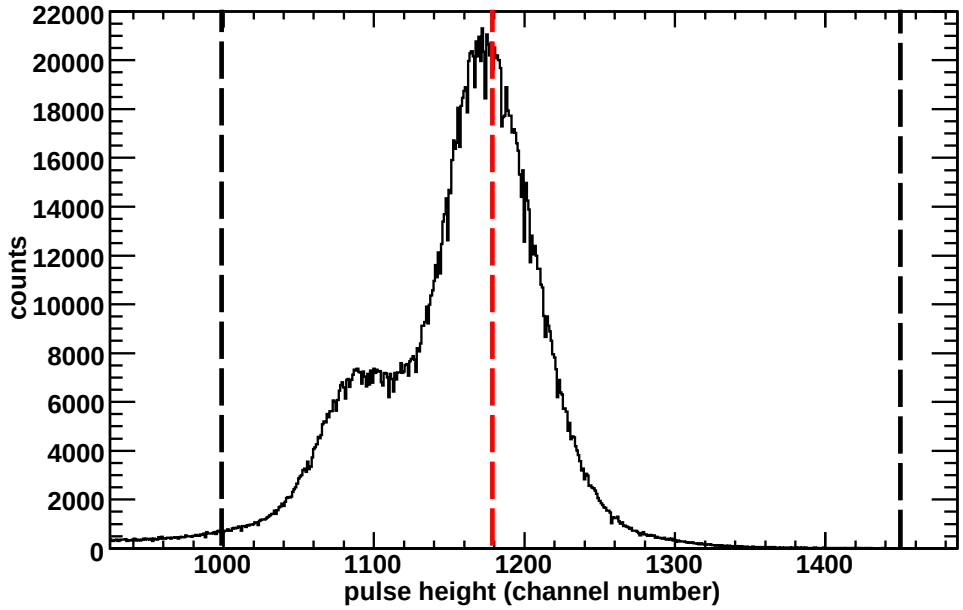

Figure 6.9: The pulse height spectrum for the high energy double peak structure, with pulses from both sides of the detector. The vertical dashed lines are the limits of the mass 26 and mass 28 windows. If not stated otherwise, the black limits are fixed at 1000 and 1450, respectively, while the red border is always chosen accordingly – here at 1180. This choice makes sure that almost no mass 26 pulses fall inside the mass 28 window, avoiding that CN + D events are mistaken as DCN/DNC + D. However, moving the red line further to the left would increase statistics in the channel DCN/DNC + D.

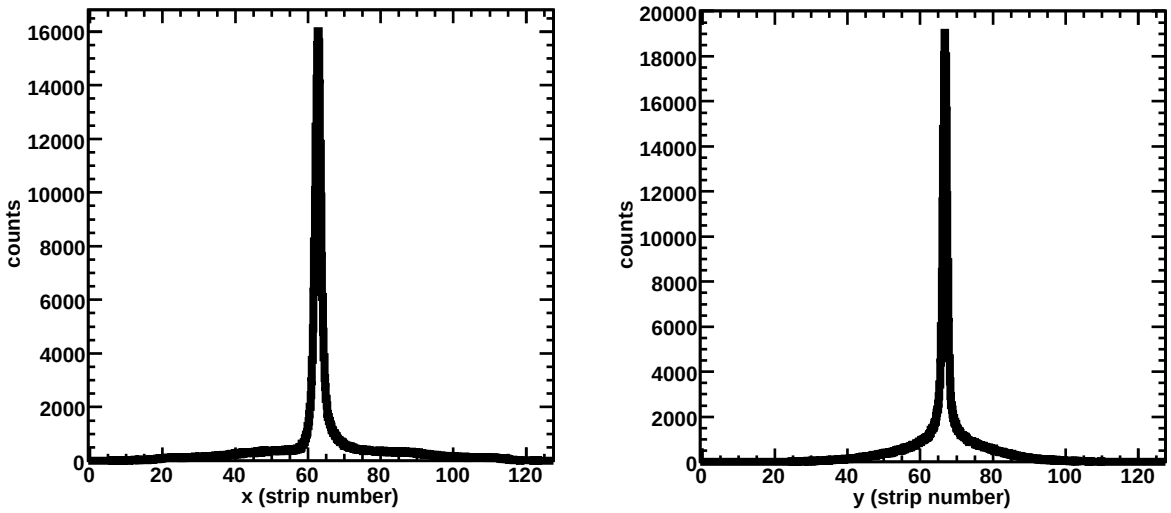

Figure 6.10: The distribution of the center-of-mass for all DR events in x and y direction. The mass windows have been chosen according to fig. 6.9.

choice of the mass 28 window would mean that many real DCN + D events are discarded unnecessarily. It is therefore indispensable to study how the choice of the windows affects the results.

Center-of-mass

Fig. 6.10 shows the center-of-mass positions in x (front side) and y direction (back side) for all identified DR events, while the border between mass 26 and mass 28 was at 1180. The narrow peaks demonstrate that phase space cooling is effective. The conditions are not perfect, however. This can be seen from the broad background extending basically over the whole detector, and from larger peak widths compared to what is usually achieved in TSR beamtimes, especially with lighter ions (see fig. 5.7 for comparison). Nevertheless, such a center-of-mass distribution can only be obtained from an actively cooled beam. The cooling process was already finished when the shutter was opened about 10 seconds after injection.

In order to suppress background events, a center-of-mass cut has been applied to the data. The cut region is shown in fig. 6.11. It corresponds approximately to the 2σ region of the central peak. The cut region is elliptical with major axes of 3.88 strip widths (2.95 mm) in x direction and 2.36 strip widths (1.79 mm) in y direction, respectively.

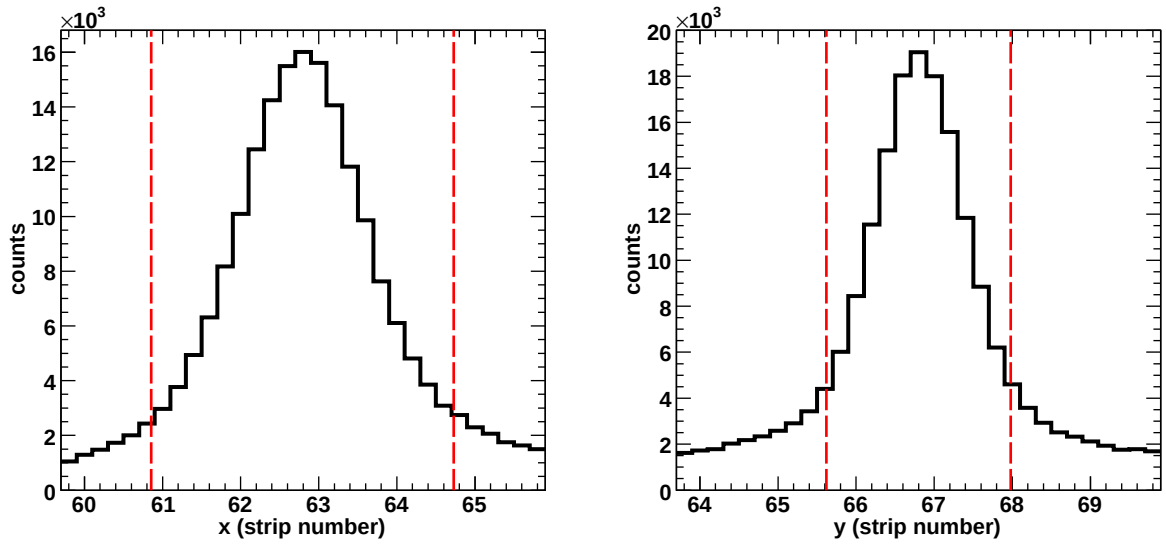

Figure 6.11: The center-of-mass distribution around the central peak in x and y. The cut region is depicted by the red dashed lines. The cut region is elliptical, while the principal axes lie along the x and y direction.

Two-body fragmentation

According to the results of Semaniak *et al.* [76] (see also table 6.1), the channel CN + D_2 should not occur. Depending on the choice of the mass windows, a few percent of the events that are identified as DR events are observed to be in this channel. However, it cannot be stated that this channel is actually produced in the DR process. Misassignments as well as background events from collisions with the residual gas cannot be excluded. Since the amount of events is statistically not enough to do a serious analysis of that channel, it will not be discussed here.

The remaining two-body channel is DCN/DNC + D. The two isomers cannot be distinguished in the mass-spectroscopical fragment identification procedure. Consequently, the events have to be attributed to one single channel in the analysis.

Fig. 6.12 shows the distribution of impact positions on the detector for the channel DCN(DNC) + D, obtained with mass windows 1000–1180 for mass 26 and 1180–1450 for mass 28. The center-of-mass cut is already applied. The impact positions extend to the edge of the detector, although the density of impact positions (for the lighter fragment, i. e. the D) starts to drop significantly long before. A cutoff in the upper and lower part

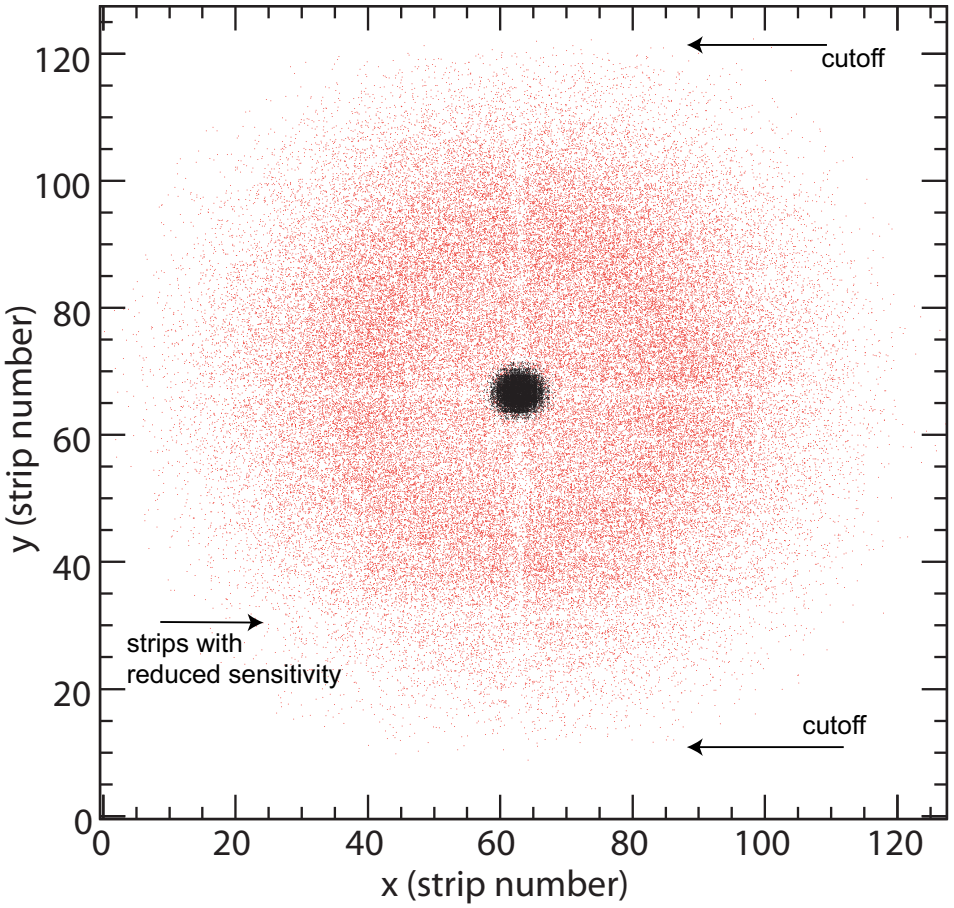

Figure 6.12: Distribution of impact positions of DCN/DNC (black) and D (red) from the two-body dissociation channel. Note that D positions within the black area are partly shadowed by the DCN/DNC hits due to the plotting procedure. The structures are explained in the text.

can also be seen – it is a shadow of the transition vacuum chamber connecting the TSR and the BAMBI beamline. It is hard to estimate the loss, but the distribution of impact positions suggests that the situation is better than suspected.

The DR process should not depend on the azimuthal angle, and therefore the pattern should be perfectly symmetrical around the center. However, a structure in the shape of a cross can be seen. This structure is of course in no way related to the DR process, but can be explained as a result of the analysis procedure. Remember that no window has been assigned for mass 30. If the fragments DCN/DNC and D hit the same strip, a pulse according to mass 30 is generated, but it is interpreted as mass 28 since it falls into the corresponding window. On the other side of the detector, however, the fragments are likely on different strips and will be recognized as mass 28 and mass 2. The fragment assignment procedure finds that the total masses on the two sides are different, and the event is discarded. Obviously, the center-of-mass lies on the strip with the double hit. Due to the narrow center-of-mass distribution, this leads to a reduced sensitivity for the strips in the pattern in fig. 6.12, given by the position of the peak in the center-of-mass distribution.

Another feature can be seen around strip 30 on the y side (back side). Here, the sensitivity of the strips is lowered due to a truncation of the mass 2 peak by the threshold in the MDI-2 VME unit (ADC threshold) for strips between 30 and 34. Unfortunately, this was only discovered after the beamtime and could not be corrected any more. About 20 % of the strips on the back side are affected by such a truncation. In most cases, the part that is cut away is small, and the affected strips are scattered over the whole detector. Except for the accumulation of such strips between 30 and 34, the effect is practically not seen in the distribution of impact positions. On the front side of the detector, this problem does not occur.

The distribution of the distances between the impact positions of the DCN/DNC and the D belonging to the same event is shown in fig. 6.13 for four different choices of the separation line between windows for mass 26 and mass 28, ranging from 1140 to 1200. Fortunately, the shape of the distribution does not change within what can be considered to be a reasonable range of possible mass windows, i. e. this result is stable against small changes in the mass windows. This looks very promising regarding the discrimination between DCN/DNC + D and other events by the coincidence requirements of the event reconstruction procedure, and allows to extract imaging information even in the case of overlapping mass peaks in the pulse height spectrum.

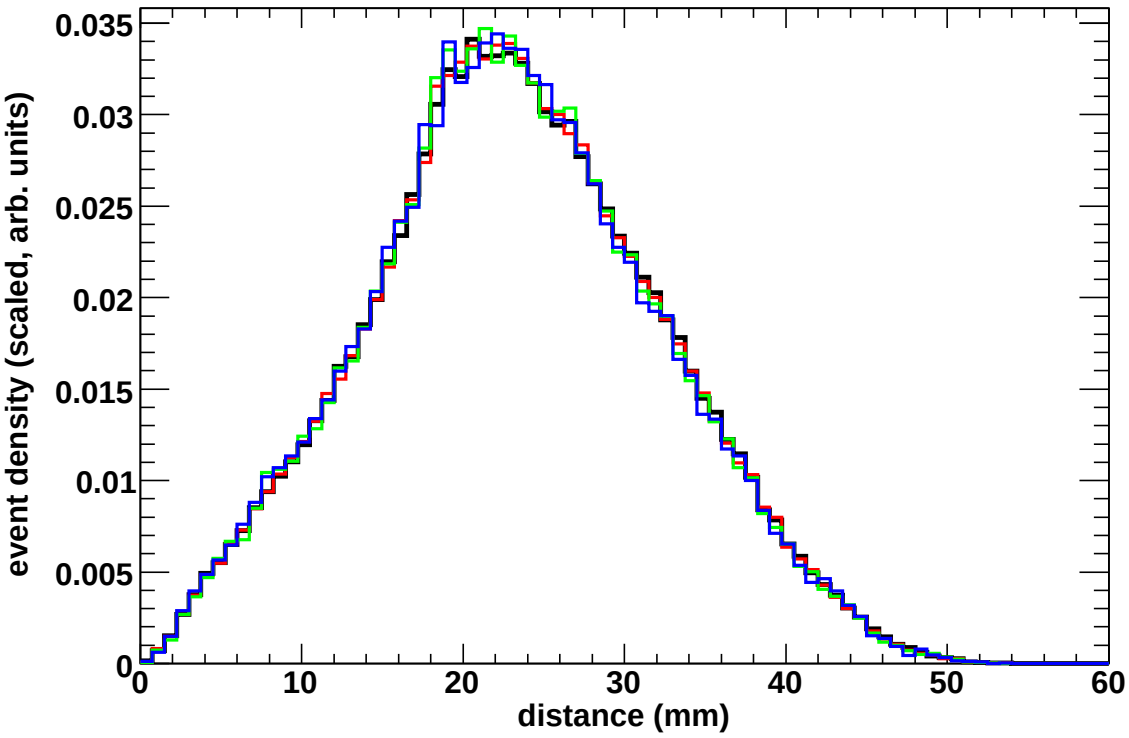

Figure 6.13: Distribution of the measured distances between the impact positions of the fragments DCN/DNC and D on the detector. The distribution has been generated for four different choices of the separation line between windows for mass 26 and mass 28: 1140 (black), 1160 (red), 1180 (green), and 1200 (blue). The borders at channels 1000 and 1450 and the mass windows for masses 2 and 4 were not changed. Note that the distributions have been scaled and that they differ by the total number of events; see also fig. 6.14.

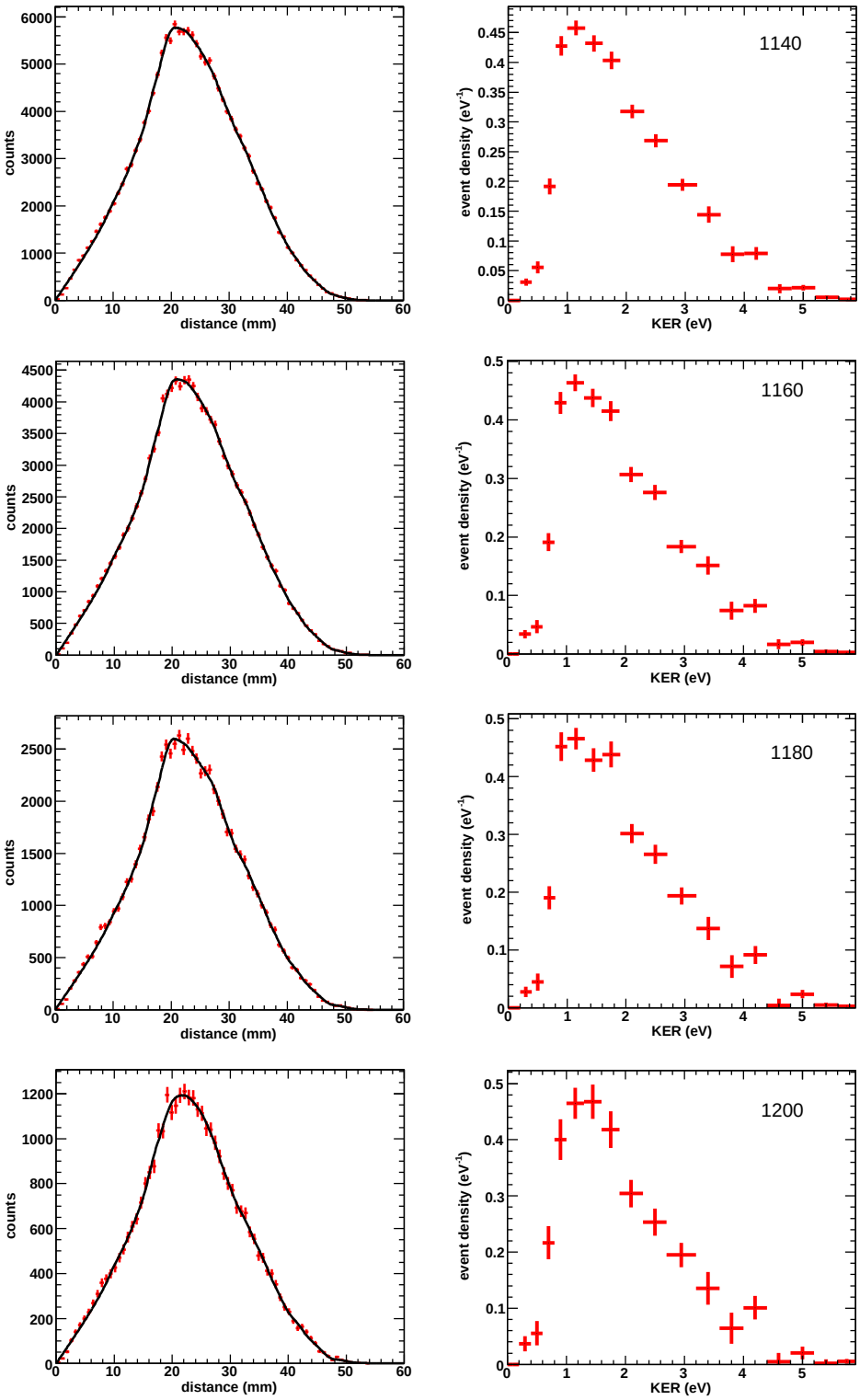

Figure 6.14: Measured distance distributions with the fit curves (left) and underlying energy distributions (right) for four different mass window choices with the 26/28 between 1140 and 1200 (see also fig. 6.13). For explanations see text.

The shape of the distributions in fig. 6.13 does not comply with a distribution pertaining to a single KER, which is the same for all events, as given by the analytic expression in eq. 3.7 (see also fig. 6.23). Instead, the observed distribution is a sum of such distributions:

$$P(d_{2D}) = \sum_j b_j P(d_{2D}, j).$$

$P(d_{2D}, j)$ is the distribution given by eq. 3.7 for a KER E_j, and the sum has to be taken over all possible final states connected with these energy releases. However, the density of states per energy interval is so high that the distance distribution is better described by an integral than a sum, i. e. rather than having a distribution over a discrete set of states, given by the branching ratios b_j, the events are continously distributed in energy:

$$P(d_{2D}) = \int_0^{E_{max}} P(d_{2D}, E) dE.$$

$P(d_{2D}, E)$ is a distribution in the projected distance *and* energy. In order to construct a fitting procedure, the energy range between 0 and E_{max} is subdivided into energy intervals. For each energy interval, a constant distribution of events is assumed, and the corresponding distance distribution

$$P(d_{2D}, k) = \frac{1}{E_{k+1} - E_k} \int_{E_k}^{E_{k+1}} P_E(d_{2D}) dE$$

with the single energy distribution $P_E(d_{2D})$ given by eq. 3.7, is generated numerically. The total distribution is then approximately given by

$$P(d_{2D}) = \sum_k a'_k \, P(d_{2D}, k),$$

with coefficients a'_k proportional to the number of events in the k-th energy interval. However, one is usually interested in the number of events *per eV*. This means that the number of events in each energy interval has to be scaled to the width of this interval:

$$P(d_{2D}) = \sum_k a_k \cdot P(d_{2D}, k) \cdot (E_{k+1} - E_k).$$

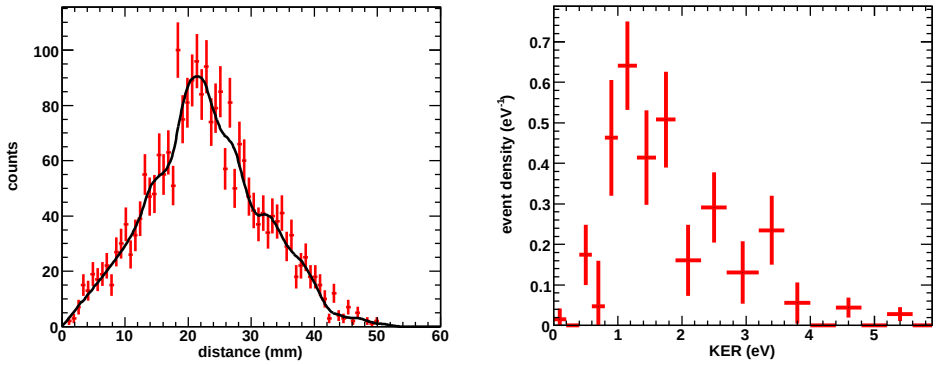

Figure 6.15: By chosing the separation line between mass 26 and mass 28 (red dashed line in fig. 6.9) such that no mass 26 pulses are within the mass 28 window, and one would obtain only DCN/DNC + D results with no background from CN + D. Here, the separation line between mass 26 and mass 28 is at ADC channel 1250, and this condition is basically fulfilled. The shapes agree well with fig. 6.14.

The $a_k = a'_k/(E_{k+1} - E_k)$ can be obtained from a fit.

The results of the fitting are shown in fig. 6.14 for the four distance distributions also shown in fig. 6.13. The event densities are almost zero for very low energies. They rise abruptly, starting at about 0.5 eV, and reach their maximum around 1.3 eV. The exothermicity for the DR channel DCN + D, which would be the maximum KER if the $DCND^+$ is in the ground state and the collision energy is 0, is 5.9 eV. It can be seen that the vast majority of events has a much lower KER. The main features of this distribution are well reproduced for all four choices of the mass windows. Even the small bump just above 4 eV is seen in all distributions. Hence, also the KER distribution is stable against small changes in the mass windows.

An interesting question is how the distance and KER distributions for the channel DCN/DNC + D are influenced from CN + D events, stemming either from residual gas collisions or incompletely detected CN + D + D events, which are erroneously interpreted as DCN/DNC + D. In order to elucidate this question, consider "pure" DCN/DNC + D and CN + D distributions. Figs. 6.15 and 6.16 show examples with choices of the mass windows resulting in two different channels. If the separation line between mass 26 and mass 28 windows is chosen such that the mass 26 peaks lies completely outside the mass 28 window, CN + D events are not misinterpreted, and pure DCN/DNC + D distributions are obtained (fig. 6.15). It can be seen that the main features of the distributions in fig. 6.14

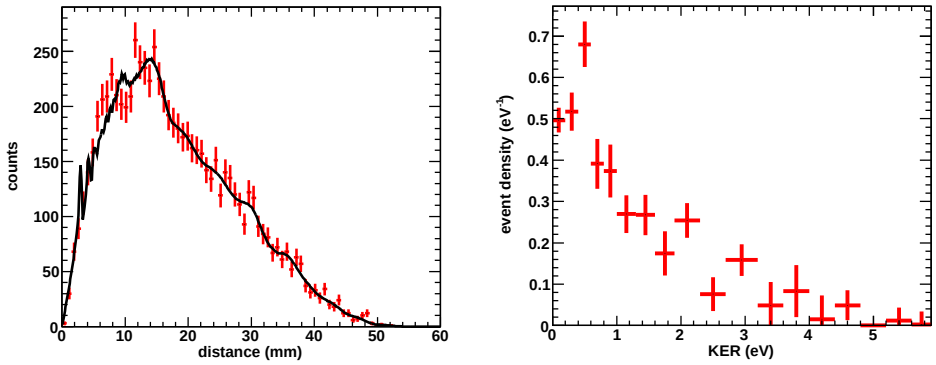

Figure 6.16: By chosing no mass 26 window and shifting the mass 28 window in the region of the mass 26 peak (here between 1000 and 1100), the influence from CN + D events can be extracted. The resulting distributions are different from the results for DCN + D (see figs. 6.14 and 6.15). It is concluded that the influence of these events in the distributions shown in fig. 6.14 is negligible.

are reproduced, especially the position of the maximum in the KER distribution. However, since many "real" DCN/DNC + D events are now not correctly recognized by the event reconstruction procedure, the result suffers from bad statistics. If the mass 28 window is chosen such that it covers only mass 26 pulses, the resulting distributions are due to misinterpreted CN + D events (fig. 6.16). These distributions look completely different. The maximum in the KER is lower than 0.6 eV, i. e. in a region where the distributions in fig. 6.14 already drop to values close to zero. Hence, it is concluded that *the background effects in the KER distribution of the channel DCN/DNC + D (fig. 6.14) are negligible for a "reasonable" choice of mass windows.*

Consequently, any of the energy distributions shown in fig. 6.14 can be regarded as a final result. In order to have good statistics and nevertheless only a small part of the mass 26 peak within the mass 28 window, the result with the mass 28 window between 1160 and 1450 is used for further discussions (see also fig. 6.24).

Three-body fragmentation

The three-body channel (CN + D + D) is less critical than the two-body channel regarding the losses of fragments, since the maximum KER is much lower and the energy is shared between three fragments. This leads to a smaller "explosion cone", and the area covered by the fragments is in any case on the detector surface.

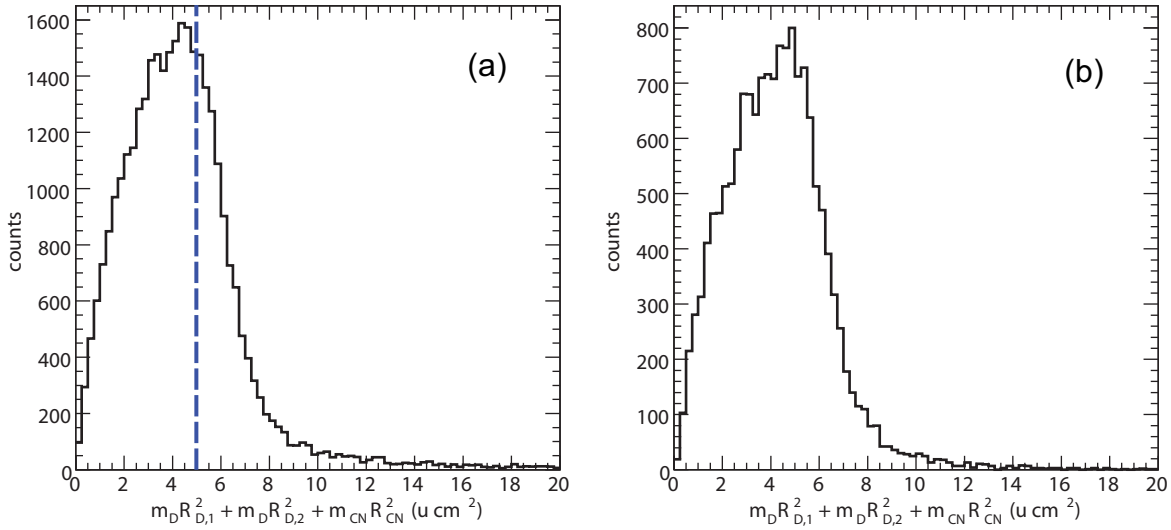

Figure 6.17: (a) Distribution of $\varepsilon^{\perp}$ of the three-body channel (CN + D + D) for a separation line at 1180. The blue dashed line corresponds to the maximum for a KER of 0.5 eV, which is about the exothermicity, assuming a maximum length of the flight path from the reaction point to the detector of 10 m. (b) Distribution obtained *without* a mass 28 window, and a mass 26 window extending from 1000 to only 1100. This seems to suppress some of the events very far out at high KERs, which might occur due to misinterpretations of two-body events with signal splitting, but it does not affect the general finding that the KER is larger than the exothermicity!

The distribution of $\varepsilon^{\perp} = \sum_{i=1}^{3} m_i R_i^2$ (m_i is the mass of the i-th fragment, R_i the projected distance to the center-of-mass), representing the KER in transversal direction, is shown in fig. 6.17. It appears that the KER must be higher than expected if the $DCND^+$ is assumed to be in its ground state. However, some of the events can be due to DCN/DNC + D events, which are misinterpreted due to signal splitting. These events can actually show a higher KER. But even a strict choice of the mass windows reveals a high KER in the three-body channel, which can only be explained as a result of excited parent ions.

The measured distribution of $\varepsilon^{\perp}$ for the three-body channel (fig. 6.17 (a)) is one of the main results, and an explanation for the high KER has to be found in any case, especially in the light of a possible contamination with other ions or higher-energy isomers. This discussion will be resumed in section 6.4.

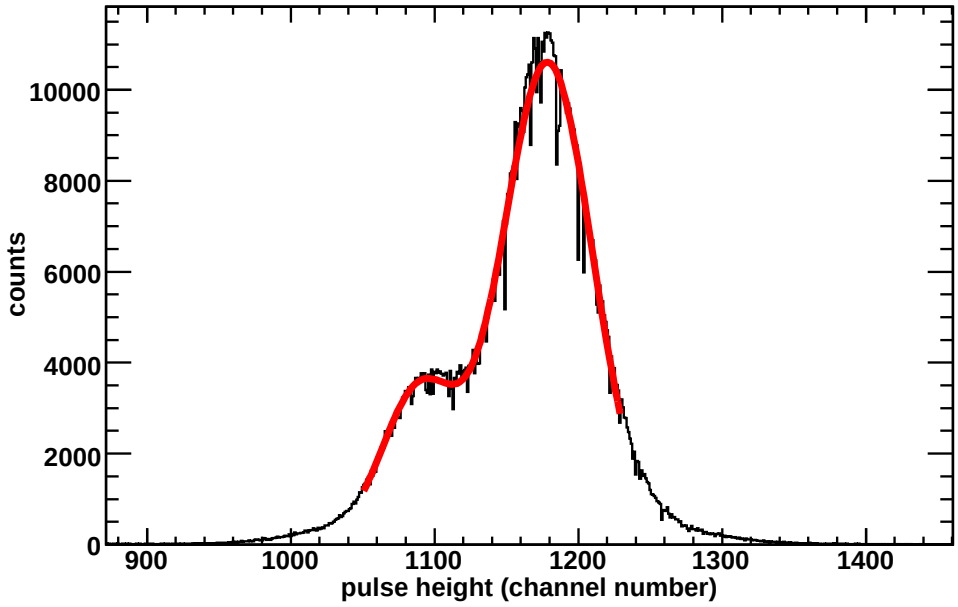

Figure 6.18: The mass 26/28 double peak (only front side of the detector) with a fitted sum of two gaussians (red). The areas under the two gaussians yield branching ratios of about 22 % for the three-body channel and 78 % for the two-body channel.

Branching ratios

Due to the overlapping mass 26/28 peaks, a determination of the branching ratios by counting of events in each channel, as shown in chapter 5, is not possible. The results would strongly depend on the choice of the mass windows. However, it would be desirable to have at least an order-of-magnitude estimate. Provided that only DR fragments hit the detector, i. e. neglecting the fact that some of the events can be induced by residual gas collisions, every mass 26 pulse would indicate a CN + D + D event, while mass 28 pulses would belong to DCN/DNC + D. Furthermore, if it is assumed that the channel CN + D_2 does not occur, these are the only possible channels. By measuring the integrals of the mass 26 and mass 28 peaks, the branching ratios can be estimated.

Fig. 6.18 shows the mass 26/28 double peak (only front side) with a sum of two gaussians fitted to it. The integrals of the gaussians correspond to branching ratios of 22 % for CN + D + D and 78 % for DCN/DNC + D. This has to be compared with the results for $HCNH^+$ from the CRYRING experiment (table 6.1), which are 32.5 % and 67.5%, respectively. The

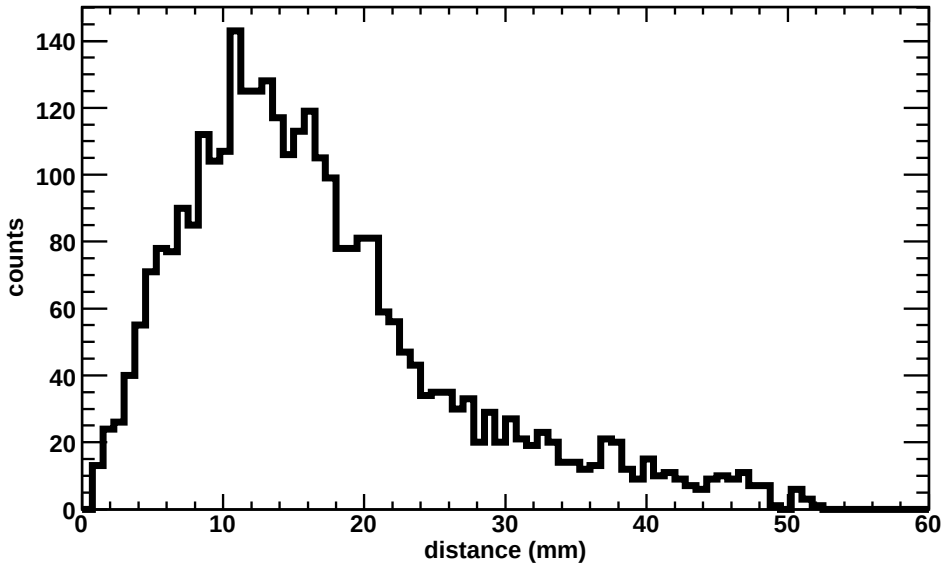

Figure 6.19: Distance distribution for the two-body channel N_2 + D of the ion N_2D^+ (corresponding to the pulse height spectrum from fig. 6.5). This channel could be misinterpreted as DCN/DNC + D, if the ion beam is contaminated with N_2D^+.

difference could indicate a possible contamination with N_2D^+; the channel N_2 + D would be interpreted as DCN/DNC + D, whereas there is no channel corresponding to CN + D + D, resulting in an observed increase of the fraction of the two body channel. Assuming that the actual branching ratios are 67.5 % for DCN/DNC + D and 32.5 % for CN + D + D, this would mean that ≈40 % of the observed two-body events belong to the channel N_2 + D. This could explain the higher fraction of the two-body channel. However, this estimate is rather inexact, and it is known that the grid method, which was used to obtain the CRYRING results, has its uncertainties as well. Consequently, this observation *could* indicate a possible contamination, although it is no definite proof.

Possible contamination with N_2D+

In order to further elucidate the question whether the ion beam was contaminated with N_2D^+, the results regarding the two-body channel of Run 000 are compared with the corresponding channel in the DR of N_2D^+.

Fig. 6.19 shows a distance distribution for the two-body channel of the data set with the

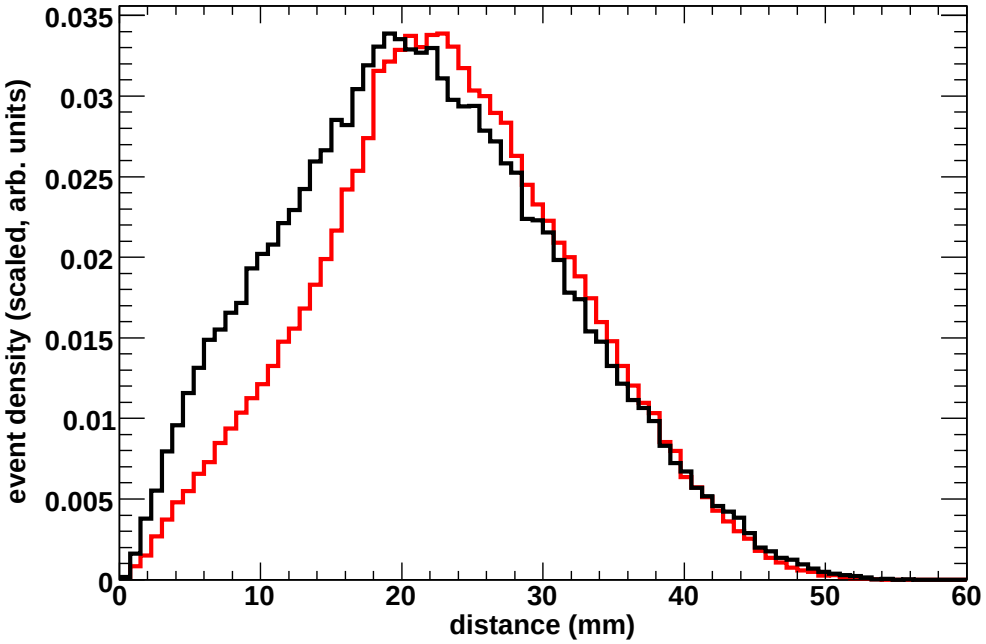

Figure 6.20: Distance distributions for the channel 'DCN/DNC + D' (including possible contamination from N_2 + D) for Run 000 (red) and Run 001 (black). The mass 28 window is between 1160 and 1450. Whereas Run 000 shows no clear trace of a contamination of the beam with N_2D^+, the data from Run 001 clearly deviate especially for small distances, indicating a considerable contamination.

pulse height spectrum shown in fig. 6.5, i. e. data which were assigned to the ion N_2D^+, with a mass 28 window between 1160 and 1450. The two-body channel with masses 28 and 2 is N_2 + D, but would erroneously be interpreted as DCN/DNC + D, if the suspected ion species is $DCND^+$. However, the distribution looks quite different from the distributions in fig. 6.13. In particular, the maximum is at a much lower distance.

In fig. 6.20, the distance distributions for the two-body channel are compared for Run 000 and Run 001 for a mass 28 window between 1160 and 1450. The data for Run 001 differ quite strongly in that an addidional bump is seen at the left slope. This is interpreted as a strong hint that the beam was contaminated with N_2D^+ and justifies the choice of Run 000 with hindsight. It is, however, not clear how much contamination is included in Run 000, since no 'pure' distance distribution for $DCND^+$ is available which could be used for comparison. Nevertheless, the contamination must be small (much smaller than the

40 % one would guess from the estimated branching ratios), since no traces of a distribution like the one shown in fig. 6.19 are identifiable.

Fig. 6.21 shows the fraction of the identified events in the two channels DCN + D and CN + D + D in each injection for the two runs for a certain choice of mass windows. In Run 000 these fractions are almost constant, with only a few outliers mainly towards the end of the run. Run 001, however, shows clearly that the conditions in the injections can change. Towards the end of the run, almost exclusively two-body events are found. This strongly indicates that the ion species is changing to N_2D^+.

6.4 Discussion of results

Three-body channel – excited parent ions

As already mentioned, the high KER in the three-body channel (see result fig. 6.17 (a)) can only be understood if the parent ions $DCND^+$ are excited. The production of internally (vibrationally and rotationally) excited ions in the source is not surprising. However, since they are allowed to cool radiatively for 10 s in the TSR before measurement, the vibrations should long have relaxed. $DCND^+$ is linear and has a dipole moment of 0.26 D [86], and therefore also the rotations should cool down to the ambient room temperature. Nevertheless, no time dependence is seen in the distributions shown in fig. 6.17. (It should be mentioned, however, that the possibility to apply time cuts is limited by bad statistics and the relatively short measurement time between 10 and 20 s after injection.) It is shown in appendix B that the lifetimes of the rotational states are actually so long (and the energy spacings between them so small) that it is possible that *radiative cooling of the rotations is so slow that it can't be seen on the time scale of the experiment.* Hence, the high KER can be understood without a contamination with other ion species or isomers.

In fig. 6.22 the measured $\varepsilon^{\perp}$ distribution is compared to simulated distributions. They have been obtained from a forward Monte-Carlo simulation of the three-body dissociation. The exothermicity has been fixed to 0.5 eV, and the rotational temperature of the parent ions has been chosen as 2000 K and 3000 K, respectively. The breakup was assumed to be uncorrelated (see [48] for an explanation of the method, which is based on Dalitz plots). The data set obtained from the simulation has been analyzed with the standard EMU analysis procedure. Since neither possible fragment excitations nor correlations in the

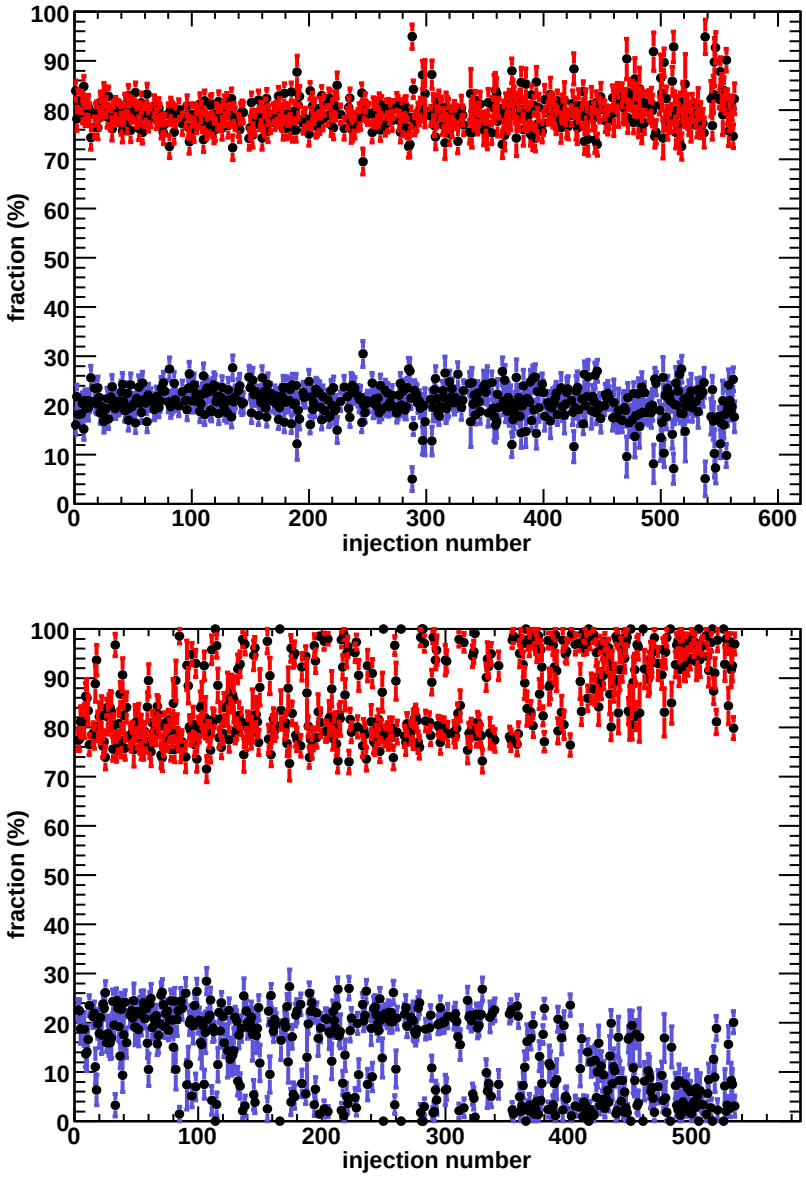

Figure 6.21: Comparison of the number of events identified as DCN/DNC + D (red) and CN + D + D (purple) for a border between the mass windows at 1160 for Run 000 (above) and Run 001 (below). The fraction in each channel is shown as a function of the injection number. Error bars represent statistical uncertainties. Whereas in Run 000 the fractions are at about 80 % and 20 %, respectively, with deviations from these values in only a few injections, a complete switching to ratios of about 100 %/0 % is observed in Run 001, indicating that the ion species changes to N_2D^+.

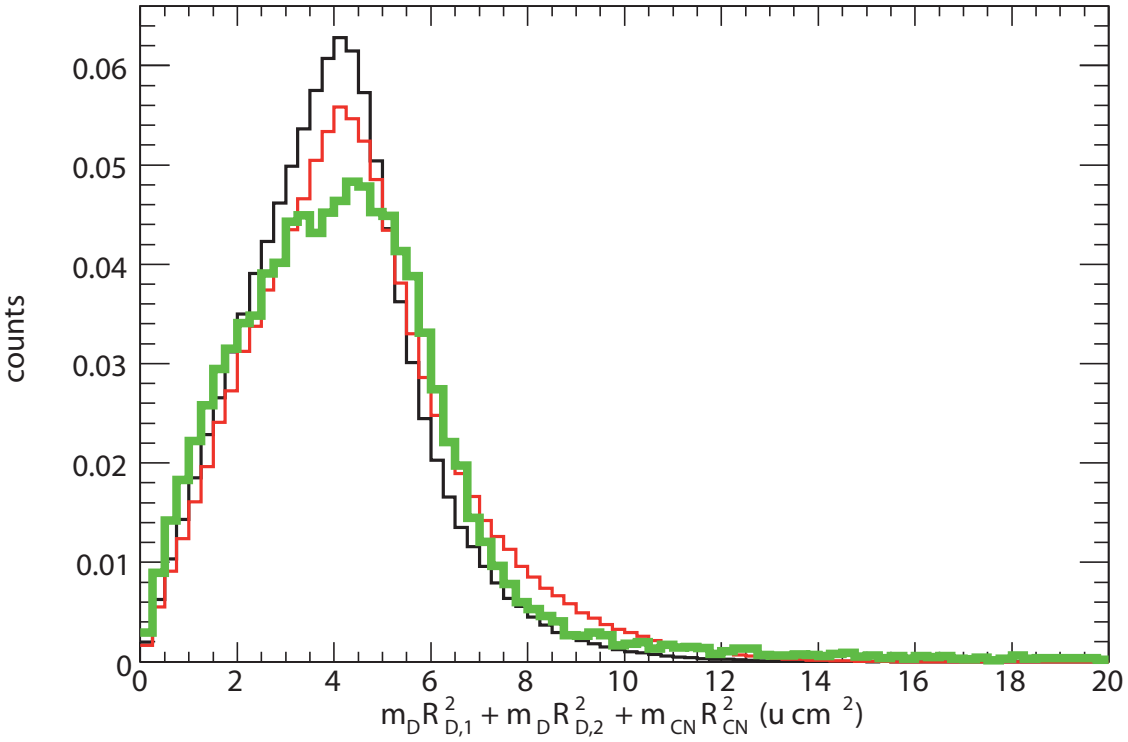

Figure 6.22: Comparison of the measured $\varepsilon^{\perp}$ distribution (green) and simulated distributions for rotational temperatures of the parent ion of 2000 K (black) and 3000 K (red).

breakup geometry have been taken into accout, deviations from the shape of the measured distributions naturally occur. However, the high $\varepsilon^{\perp}$ tail of the distribution gives an estimate of the rotational temperature, which seems to be higher than 2000 K.

Two-body channel – excited molecular fragments

The goal of this experiment was originally to make a statement about the DCN/DNC branching ratio. So far, there was no distinction between the two isomers, since they have the same mass and are not distinguished by the EMU detector. The exothermicities of the two decay channels are 5.9 eV and 5.3 eV, respectively (see appendix C), and there would have been a chance to distinguish between them if the whole exothermicity would show up as the KER (see fig. 6.23). However, the measured distance distribution significantly differs from what would be expected. It actually shows that for most events only a minor

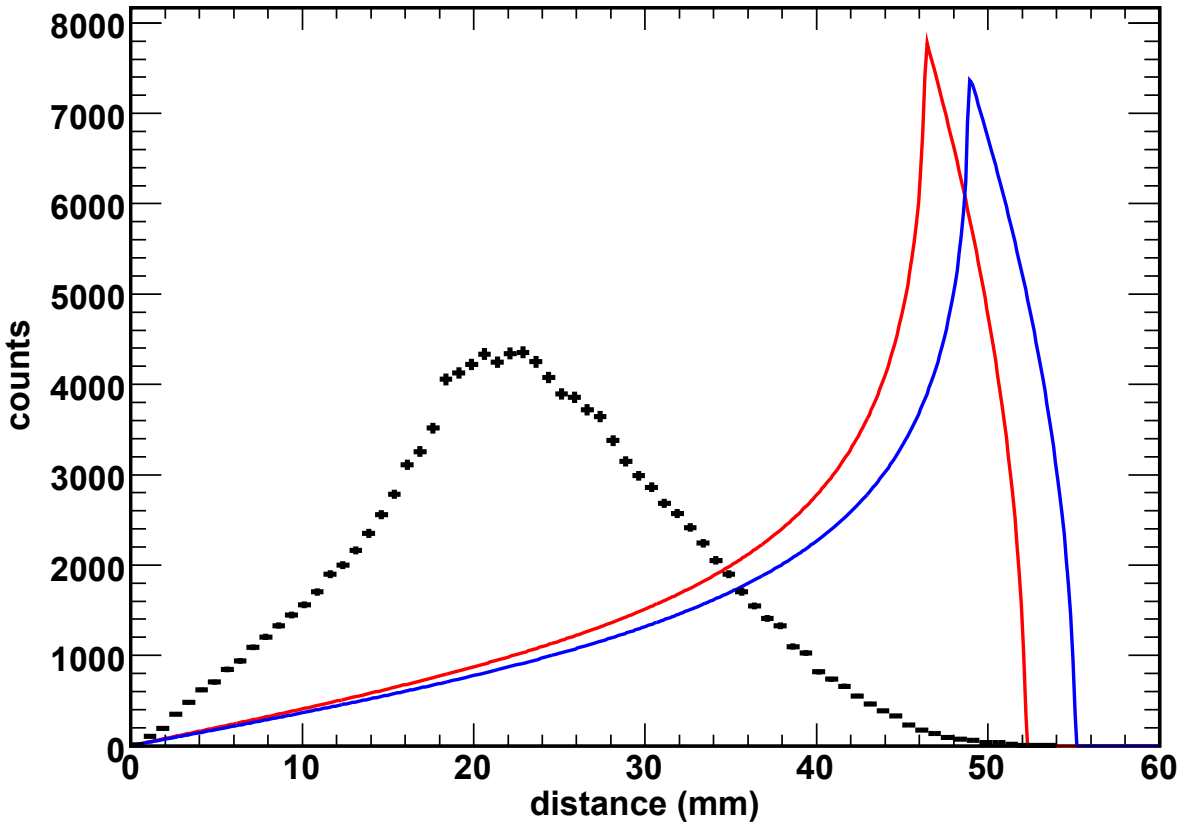

Figure 6.23: Simulated distance distributions for energy releases of 5.9 eV (blue) and 5.3 eV (red), corresponding to the maximum KER of DCN + D and DNC + D, respectively. As a comparison, the measured distance distribution of the DCN/DNC + D channel is shown.

part of the available energy goes into the KER. The only explanation is that *the molecular fragment, be it DCN or DNC, is produced in internally excited states.* This can be rotational or vibrational excitation – there is no way to distinguish between them in this experiment. However, the excitation energies of a few eV (!) suggest that a main part of the energy goes into *vibrational* excitations, since the small energy spacings of the rotational levels would require very high rotational quantum numbers and angular momenta connected with them.

The KER distribution for the finally selected settings (mass 28 window from 1160 to 1450) is shown again in fig. 6.24, together with some energy levels relevant for the process. All energy levels are based on the assumption that the parent ion $DCND^+$ is in its ro-vibrational

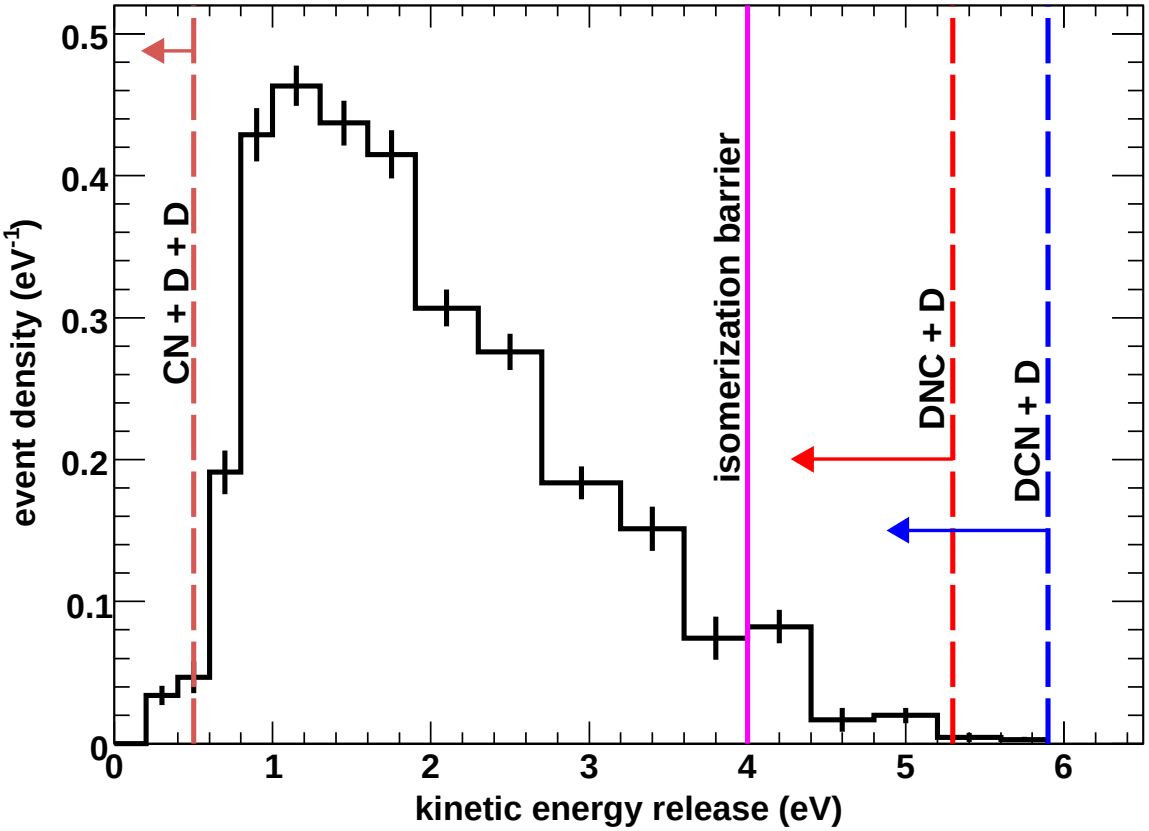

Figure 6.24: The KER distribution for two-body decays. The vertical dashed blue and red lines are the maximum KERs for DCN + D and DNC + D, respectively, assuming that $DCND^+$ is not excited. The arrows point in the direction of increasing internal energy of the fragment. The isomerization barrier and the threshold for dissociation into CN + D + D are also shown. For explanations see text.

ground state. The maximum KER of each isomeric decay channel is marked. The distance to these markings is the excitation energy with respect to the corresponding ground state level. However, the actual excitation energy can even be higher, since it is known from the three-body channel that the parent ions are rotationally excited, thus bringing additional energy into the reaction and allowing the KER to be higher.[5] At a KER of $\approx 0.5\,\mathrm{eV}$, the excitation energy is that high that the dissociation limit is reached and the DCN/DNC further dissociates into CN + D. This causes the sudden drop of the distribution to almost zero – the events here are not seen, because they are already in the three-body channel. It can be seen that this drop is not as sudden as it would be expected, and that it starts at least half an eV above the threshold. This is again due to the rotational excitation of the parent ions and agrees with the result from the three-body channel. Furthermore, the event density is not exactly zero below 0.5 eV. This could again indicate a possible contamination with N_2D^+, however showing that the effect is small.

In addition, the isomerization barrier, i. e. the energy barrier separating the two isomers in the triatomic PES of the system H/C/N, is depicted in fig. 6.24. For all events with a KER lower than 4 eV, the DCN/DNC fragment is excited above this isomerization barrier. The parent ion excitation would move this barrier even further to the right. Hence, the results of the two-body channel yield an extraordinary interesting finding: *Most of the molecular fragments in the dissociation channel DCN/DNC + D are excited above the isomerization barrier, and the probability of finding an excited fragment (per energy interval) even rises with increasing energy; the most probable excitation energies are just below the dissociation limit 3.5 eV above the isomerization barrier.*

This result is extremely important regarding the DCN/DNC branching ratio. It means that the formation of the two isomers is not completely explained by the DR process, but that *only after radiative cooling of the highly excited fragment to either DCN or DNC, the identity of the isomer is finally settled.* As long as the vibrational state of the fragment is above the isomerization barrier, *isomerization is energetically possible!*

[5] For the results shown here, the maximum KER, as it was used in the fitting, has been chosen to be 5.9 eV. Energy intervals reaching to higher energies would result in event densities in agreement with a value of zero in that region.

Radiative relaxation of highly excited D/C/N

Starting with the question whether DCN or DNC is produced in the DR of $DCND^+$, the somehow surprising answer is that the fragments that are found are neither DCN nor DNC, but a highly excited molecule, that cannot easily be attributed to one of the isomers, is formed. This shifts the question from the DR process to the process of radiative cooling of vibrationally excited D/C/N, which could of course not be studied in the experiment at the TSR. One theoretical paper has been published about relaxation of highly excited H/C/N by Barger *et al.* [87]. For the lowest 500 vibrational states, reaching just above the isomerization barrier, the probabilities for relaxation to HCN and HNC are calculated. Three different kinds of states are found:

1. HNC-localized states, which almost always relax to HNC,
2. HCN-localized states, which almost always relax to HCN,
3. non-localized states, which can relax to both HCN and HNC.

The first non-localized state is just below the isomerization barrier (tunneling), and the localized states are found in the respective potential valley as well as *above* the isomerization barrier. The authors also studied the resulting branching ratios, assuming that the states are initially equally populated. The values for the HNC/HCN ratio are between 0.59 (all 500 levels populated) and 0.98 (only the 25 highest levels populated) and tend towards unity the higher the average excitation is.

Regarding the results of the present experiment, the findings of Barger *et al.* are very encouraging, since they suggest that the final result after DR *and* vibrational relaxation is indeed a DCN/DNC ratio close to unity. However, they also tell that the outcome after relaxation strongly depends on the initial vibrational state. Since we can only state the distribution in energy and not over specific states, we cannot exclude that a certain kind of states is favored. Amano *et al.* [68] found different vibrational temperatures for stretching and bending modes, suggesting that the bending motion is probably not so easily excited in the DR. One would expect, however, that a large bending motion is required in order to obtain delocalized states which can isomerize. On the other hand, it could also mean that the bending motion cools faster than the stretching modes.

In any case, the results from Barger *et al.* extend only to excitation energies of about 2.5 eV, whereas in the present experiment much higher excitations up to more than 5 eV are

observed. It is still an open question how such highly excited fragments relax towards the two isomers. One argument would be that the fraction of delocalized states increases with energy. Intuitively, it is clear that the light D can easily move around in a bending motion for such high energies, and that it can stick to either side of the molecule during relaxation with about a 50:50 probability. In addition, since there are hundreds of vibrational states in between, the cooling process would be stepwise in a long cascade. Therefore, even if the probability for the D to jump to the other side of the molecule is small in each step, these probabilities would add up and lead to a population of all kinds of states. An ensemble of molecules starting at excitation energies high above the isomerization barrier would probably be equally distributed over the available states once it has relaxed to just above the isomerization barrier, where the result of Barger *et al.* would apply, leading to an DCN/DNC ratio of unity.

6.5 Comparison with other ions

One of the systems investigated so far with the EMU detector is D_3O^+. Interest comes again from the chemistry of interstellar clouds, where DR of H_3O^+ is believed to be a major source of water molecules.

The most exothermic channel in the DR of H_3O^+ is the dissociation into H_2O + H with an exothermicity of 6.4 eV. However, this channel accounts for only 18 % of the events, and the less exothermic three-body channel (OH + H + H; exothermicity: 1.3 eV) has a branching ratio of about 67 % [31]. It has been proposed that the fragment H_2O is produced in vibrationally excited states and that it will further dissociate into OH + H if the internal energy is above the dissociation barrier [88]. The EMU results – again measured with the completely deuterated ion – indeed support this idea. The energy distribution of the KER in the channel D_2O + D shows a similar behaviour as for DCN/DNC + D; lower energy releases are favoured, indicating high fragment excitation, and an even sharper cutoff at the dissociation barrier is seen [64].

This sheds new light on the question whether the two-body channel is favoured over the three-body channel, or vice versa. Whereas the two-body channel is dominant for $DCND^+$, it is the other way around for D_3O^+. The observation is that the exothermicity of the three-body channel as compared to the two-body channel is higher for D_3O^+. In the $DCND^+$ case, the ratio of the available energies is 0.5 eV:5.9 eV, while it is 1.17 eV:6.36 eV

for D_3O^+. Thus, assuming an energy distribution of the fragments that rises with the excitation energy, a larger fraction can be excited above the dissociation barrier in the D_3O^+ case. The conclusion would be that the large branching fraction for OD + D + D comes from many "over-excited" two-body events, whereas there is not so much room to access states above the dissociation barrier of the DCN/DNC, consequently leading to a smaller fraction for CN + D + D[6].

The results for both ions and for D_2H^+, which is also vibrationally excited [59], show that many theoretical treatments of DR branching ratios oversimplify the dissociation mechanism. Usually, emphasis is put on the calculation of potential curves or potential energy surfaces, and favoured dissociation pathways are identified. The picture that is sometimes invoked is that of rigid molecular fragments moving along the potential curves (as e. g. in [78]). The role of vibrational excitation during the dissociation process cannot be accounted for in that picture. The theoretical treatment of the DR of *polyatomic* ions requires a whole new understanding. A first step would be the explanation of the distribution of vibrational excitation energies of the fragments. If this distribution could be predicted theoretically, it could be used to estimate how many two-body events are excited above the dissociation barrier. This would help to refine the theoretical understanding (and prediction) of chemical branching ratios, which are badly needed for the modelling of interstellar chemistry.

A further interesting aspect of the results is that they suggest the existence of vibrationally highly excited molecules in environments where DR is important. This could help to understand so far unexplained features in the spectra of astronomical objects. Recently, some lines in cometary spectra could be assigned to vibrationally excited water [89]. DR could be a possible source of these molecules. It would be no surprise if more unidentified lines can be related to vibrationally highly excited molecules in the next years.

6.6 Conclusions

The main result presented in this chapter is the production of vibrationally excited molecular fragments in the DR process, in which the excitation energies can be a few eV. For the particular fragment D/C/N this means excitation above the DCN-DNC isomerization

[6] or CN + H + H, respectively, since the branching ratios for the DR of $DCND^+$ have not been measured.

barrier.

This result was obtained in a storage ring experiment; the storage ring method is probably the most precise way to study DR, since it allows to perform the experiment under well controlled conditions, using electron cooling. It should be stressed, however, that such a result was only possible with the use of the new EMU detector. The imaging data can be recorded with any kind of imaging detector, e. g. MCP-based systems, but the distinction between different decay channels can only be achieved with a mass-sensitive system. Although the resuls of Semaniak *et al.* [76] suggest that there is only one two-body channel, it would not be sufficient to use the two-body events in a conventional imaging experiment, since they could also be CN + D from collisions with the residual gas, or from incompletely detected three-body events. A center-of-mass cut would not completely eliminate them, since the center-of-mass is mainly determined by the heaviest fragment (i. e. the CN or DCN, respectively), which have almost the same mass, and the cut would not be strict enough, since many background events would still lie within the allowed cut region. On the other hand, it was not possible to identify the fragments unambigously, since the peaks in the pulse height spectrum corresponding to masses 26 and 28 could not be resolved completely. However, by applying a center-of-mass cut *and* by studying different cuts in the pulse height spectrum, it was possible to show which effects come from real DCN/DNC + D events, and how the background from CN + D would look like. This would not have been possible with a conventional imaging detector *without* mass-sensitivity.

A possible contamination of the ion beam with other ions or with a different isomer cannot finally be ruled out. However, the energy releases that are observed are in agreement with $DCND^+$, especially the position of the dissociation barrier, taking the rotational excitation of the ion into account. It could be shown that the high parent ion excitation can be explained with long rotational cooling times. It would be advantageous to find a way to produce the ion in rotationally cold states, since this would better reflect the conditions in cold dense interstellar clouds.

Together with other results obtained with the EMU detector [64], the one presented here shows for the first time how the available energy is shared between KER and internal excitation of the molecular fragments. It is surprising that high excitation energies are favoured; such a clear trend has not been anticipated, although it was known that vibrationally excited fragments can be produced in the DR of simpler ions like H_3^+ [90]. This finding presents the DR mechanism for small polyatomic molecules in a new light. It is a

new challenge for theory to understand the excitation mechanism and to predict energy distributions. Obviously, the dissociation process is highly dynamical. Instead of following a potential curve leading to the dissociation of a particular bond, all degrees of freedom of the whole system are involved. It is amazing that the capture of a low-energy electron can trigger such a violent movement of the heavy nuclei.

This new insight into the DR mechanism has implications on the question about the HCN/HNC branching ratio, which has been discussed for such a long time. The idea that both molecules can be formed in the DR of $HCNH^+$ was mainly driven by the fact that $HCNH^+$ has a linear structure, and the problem was sometimes reduced to the question whether the H-C or the H-N bond is more likely to break. In that picture, the isomeric nature of the fragment is determined by the dissociation process itself. The result presented in this thesis, however, shows that this kind of thinking points into the wrong direction. The DR process yields a highly excited fragment above the isomerization barrier, and it is only the subsequent relaxation process that fixes the isomeric configuration. As far as the author knows, the only publication where such a two-step process (DR & relaxation) has been anticipated is the paper by Barger *et al.* [87]. If isomerization can occur after the dissociation, it may also be possible *during* the DR process. The structure of neutral molecules differs in general from the structure of their ions, and it is not surprising if the electron capture is associated with a change in the geometry. Alternatively, one can think of an indirect process, where the electron is captured in a Rydberg state. While it relaxes through the Rydberg ladder (as proposed by Shiba *et al.* [79]), the molecular 'core' acquires more and more vibrational energy, until it can change it structure. Being highly dynamical, DR should not only be seen as a process where bonds are broken, but where also new bonds can form.

Although the mechanism revealed by the EMU detector is completely different from the traditional view, it supports the idea of an HCN/HNC production ratio close to unity. In order to further elaborate on the consequences of the proposed two-step mechanism, it is suggested that the relaxation of highly excited H/C/N (D/C/N) with excitation energies up to about 5 eV is studied theoretically.

7 Summary and outlook

The two main achievements presented in this thesis are a new experimental method to study the dissociative recombination of small polyatomic ions, and new aspects regarding the production of molecular fragments in this process. In particular, this concerns the fragment excitation and implications for the isomeric configuration of the fragments stemming from the DR of the ion $DCND^+$. It is shown that – in contradiction to the general perception presented in literature – the isomeric configuration of the triatomic fragment D/C/N is not finally determined by DR. In fact, this fragment is mostly produced in vibrationally excited states, which are energetically above the isomerisation barrier between the isomers DCN and DNC.

The new experimental technique relies on the *energy-sensitive multi-strip detector* (EMU), which is a double-sided silicon strip detector with 128 vertical and 128 horizontal strips. This detector allows for a position-sensitive detection of the impinging fragments, while they can be identified mass-spectroscopically. It has been shown in chapter 4 that such a detector can reconstruct the 'transversal' kinetic energy release, i. e. the kinetic energy release taking only the velocities parallel to the detector surface into account; this can always be achieved for each dissociation event separately, even if the impact positions of the individual fragments cannot be assigned unambiguously, as it is the case for decay channels with two or more fragments of the same mass. Under certain circumstances, it is possible to extract the *total* KER from the distribution of the *transversal* KER of many events.

One of the strengths of the EMU detector is its capability to distinguish between decay channels with chemically different fragments, which is a prerequisite in order to study questions depending on the fragmentation channel. For that reason, the EMU detector is ideally suited for experiments with polyatomic ions. Apart from the measurement of the KER, it can be used to determine chemical branching ratios.

The detector has been characterised by a measurement on the DR of CHD^+, as presented in chapter 5. This ion provides fragments over a wide range of masses, with mass differences

of only one mass unit. It could be shown that the mass resolution is good enough to distinguish all different decay channels. However, some detector effects, e. g. 'signal splitting' or the occurrence of 'side peaks' related to the design of the detector, complicate the analysis. The origins of these effects are mostly understood; nevertheless, their influence on the results has to be taken into account, depending on the problem under investigation. Especially the measurement of branching ratios requires a correction by using a Monte-Carlo simulation of the dissociation and measurement processes. Thus, detector effects can partly be taken into account. The results show a strong isotope effect – the ejection of the H atom is favoured over ejection of the D in two-body breakups. Branching ratios measured with the EMU are also found in [59] for D_2H^+ and in [63] for D_3O^+.

One of the mysteries of DR is the isomeric branching between HCN and HNC in two-body decays in the DR of $HCNH^+$. Theory suggests that these two molecules are produced at a ratio of about 1:1. However, the different theoretical approaches were not able to agree about the reaction mechanism. Furthermore, it is assumed that the DR of $HCNH^+$ is the main source of HNC and HCN in interstellar clouds. Based on this assumption, astronomical observations also suggest that the production efficiencies are the same for both isomers. However, the isomeric branching could never be determined experimentally. In order to shed some light on the problem, an experiment at the TSR using the EMU detector has been performed. The completely deuterated species $DCND^+$ has been chosen instead of $HCNH^+$ due to experimental reasons. The experiment and the results have been discussed in chapter 6. It has been shown that the molecular fragment DCN or DNC, respectively, is mostly produced in vibrationally excited states above the energy barrier between the two isomers, with excitation energies of up to more than 5 eV above the ground state, reaching to the threshold for dissociation into CN + D. In the dilute plasma of interstellar clouds, these highly excited fragments can basically only relax radiatively. The results of the EMU measurement have been discussed in the light of a theoretical study of the relaxation of highly excited H/C/N [87]. It was suggested that indeed the production of both isomers is efficient. However, this result clearly shows that the common perception of the DR process is not correctly describing the production of the isomers; it is not the DR process that determines the isomeric configuration of the molecular fragment, but only by subsequent radiative relaxation the isomer is finally set.

The results suggest a two-step process as production mechanism of both isomers in interstellar environments, namely DR, followed by subsequent radiative relaxation. So

far, this has only been considered in [87], and this thesis provides the first experimental evidence. Although the original goal, which was to measure DR branching ratios for the production of the two isomers, turned out to be not achievable, it is this very result which is probably much more interesting, since it provides a new perspective regarding the DR process instead of just numbers needed in astrochemical models. However, many questions are still open. Neither the excitation mechanism yielding excited fragments nor the relaxation afterwards are well understood. Especially the latter aspect could be much improved. Calculations already exist for energies of up to about 2.5 eV above the HCN ground state, and it is suggested that they are extended until the dissociation barrier. Furthermore, it should be emphasized that – since vibrational states are involved – the results obtained for $DCND^+$ cannot directly be transferred to $HCNH^+$. It would therefore be desirable to do the experiment with $HCNH^+$ as well.

As far as the performance of the detector is concerned, all requirements have been met. It was shown in the previous chapters that the EMU detector serves very well as a fast detector providing 2D imaging data, recording up to 2000 events per second. Regarding the intended scope of applications, which includes mainly channel-specific imaging of the DR of small polyatomic ions and the measurement of branching ratios, this is a superb performance, especially when compared to the readout-rate of a CCD-based imaging detector of typically below 100 Hz. Furthermore, 2D imaging data and branching ratios are measured simultaneously. This has never been achieved before in a storage ring-based DR experiment.

However, one can still think of improvements which would even expand the capabilities of the EMU detector. Whereas the maximum detection rate of 2 kHz is more than required in an imaging experiment, it would be rather low in order to measure rates for the determination of reaction cross sections, since one would always risk to encounter saturation effects. Therefore, a possible upgrade of the EMU detector could be targeted at the improvement of the maximum rate, e. g. by using upgraded electronics and further suppressing noise-triggered readouts.

It took quite some time to get the EMU detector working, to understand its characteristics, and to develop appropriate analysis procedures. For the future, this opens new opportunities to study the DR of further ions like NH_2^+, NH_4^+, DCO^+ (which has already been measured and is currently being analyzed), or CH_3^+, which are not only relevant in astrochemistry, but can also help to uncover the secrets from the process of DR of small polyatomic ions.

A Event reconstruction for the EMU detector

This appendix describes the event reconstruction procedure for the EMU detector. Data processing is described as far as it is relevant for the event reconstruction.

A.1 Introduction

The *energy-sensitive multi-strip detector* (EMU detector) is a fully depleted silicon strip detector with 128 vertical strips on its front side and 128 horizontal strips on its back side. Its goal is to study molecular breakup processes in a storage ring on an event-by-event basis. The focus is on small polyatomic molecules, i.e. on systems than can dissociate into three or more fragments. When hitting the detector, each fragment produces an amount of free electrical charge proportional to its mass. This charge is detected in both the horizontal and vertical strip crossing at the impact position. Since all fragments stemming from the same dissociating molecule arrive at the detector within a few nanoseconds and can therefore not be detected one after one, an "event" is characterised by a number of strips generating electrical pulses with different pulse heights – depending on the number of fragments, their masses and impact positions. The task of the event reconstruction procedure is to obtain from this "strip pattern" the masses and impact positions of the different fragments for further analysis.

A.2 Processing of raw data

The EMU detector takes advantage of *mileDAQ* [91], a dedicated control and data acquisition system developed for TSR experiments. *mileDAQ* and its data format for raw data

files (which are actually ASCII files) has been described elsewhere (see [91] for further information). Here it should suffice to mention that the details of the data format depend on a separate program called *daq_listen* that is responsible for writing the raw data files. Special versions of both *mileDAQ* and *daq_listen* exist in order to control the readout of the EMU detector and to write special raw data files containing EMU data.

An important subsequent data processing step is the translation of the raw data files into ROOT files. ROOT offers the possibility to store data in a data structure called *tree*. The different information available for each event are assigned to different *branches*. Each entry in a tree (represented by an entry in each of its branches) corresponds to an event. The variables attached to a branch are referred to as *leafs*.

The translation is done by a program called *emu2root*, a descendant of *md2root*. The output format differs slightly. Here only the branches containing EMU specific data are considered:

- The branch *event_length* contains the number of responding strips (event length) of the event. The data type is a 32 bit signed integer.

- The branch *strip_num* contains the ordinal numbers of the responding strips (their ID, in a manner of speaking) as an array (type 32 bit signed integer) of variable size. The size is given by the event length.

- The branch *ampl* contains the pulse heights as an array (type 32 bit signed integer), again the size being given by the event length. The array indices correspond to the indices of the ordinal numbers of the strips, i. e. the strip with number `strip_num[i]` has the pulse height `ampl[i]`.

Branch	**Leaf(s)**	**Data type**
event_length	event_length	I
strip_num	strip_num[event_length]	I
ampl	ampl[event_length]	I

Further branches contain data that are generally required for molecular experiments at the TSR. Since they appear also in the standard *md2root* output files and are not used for event reconstruction, they will not be described here.

In general there are two ways to handle the pulse height data. They can be stored as they were measured, disregarding the different characteristics of the strips (different pulse heights for the same fragment type and same energy), which have to be considered later in the event reconstruction. The other possibility is to apply a calibration (cross-normalization) during the translation with *emu2root*, i. e. to move the peaks in the pulse height spectra for all strips to the same position. The calibration data used in the $DCND^+$ experiment were obtained from DR data of D_3O^+ from December 2008.

Another remark should be made regarding the ordinal numbers of the strips. In the raw data format, the strip numbers do not directly reflect the strip positions on the detector. This is changed during the translation by *emu2root*. From the ROOT file on the strips on the back side of the detector (horizontal) have the numbers 0 to 127, whereas the strips on the front side (vertical) are connected with the numbers 200 to 327. Now strips with consecutive ordinal numbers lie adjacent to each other on the detector.

All further analysis steps – including the event reconstruction – make use of the ROOT file instead of the raw data file. For this purpose a graphical user interface (GUI) can be used.

A.3 Event reconstruction

A.3.1 General remarks

A graphical user interface, called *EMU_GUI*, can be used to perform the event reconstruction by essentially clicking only one button. Unfortunately, this requires the code of the *EMU_GUI* to be changed for every molecular species and beam energy. As far as the event reconstruction is concerned, this affects only

- the number of possible fragments with different mass (number of peaks in the pulse height spectrum)
- their masses, so far only as integer numbers
- the "mass windows", i.e. the lower and upper bounds of the peaks
- a threshold for the summation of neighbouring strips (see below)
- the different DR channels and the possible values of the variable *check* (see below).

For further analysis steps other changes in the *EMU_GUI* have to be made.

If the pulse heights are already calibrated or if the differences in the pulse heights between the different strips are small compared to the distance between peaks of different fragments, it is sufficient to specify only one set of mass windows. Otherwise, individual mass windows for the strips must be used. This is also the case if the calibration failed or is not precise enough. Mixed procedures (one window for a high energy peak, individual windows for a low energy peak) may also be used.

When clicking on the appropriate button, the function *cm_identify()* is called. The main task of this function is the calculation of the centre-of-mass positions for all identified DR events. This requires of course that the identification of the fragments has already been performed. For that reason the function *cm_identify()* calls another function – *identify()* – at the very beginning. *identify()* executes the event reconstruction procedure.

The function *identify()* creates a new ROOT file. (If the name of the ROOT file containing the raw data was *<name_of_beamtime>_<run_number>.root*, the name of the new ROOT file will be *<name_of_beamtime>_<run_number>_frag_data.root*.) This ROOT file contains a tree (named *fragments*) with the following branches:

Branch	**Leaf(s)**	**Data type**
check	check	I
event_length	event_length	I
masses	masses[event_length]	I
n_masses	n_masses	I
mass	mass[n_masses]	I
fposx	fposx[n_masses]	F
fposy	fposy[n_masses]	F

The data type F is a 32 bit floating point.

The branch *event_length* contains the same data as the branch with the same name in the raw data ROOT file. The contents of the other branches will be explained in the following.

The event reconstruction routine loops over the whole raw data tree. For each event, it first reads the entries in the branches *event_length*, *ampl* and *strip_num*.

A.3.2 Interpretation of pulse heights (mass assignment)

Each responding strip is now compared with the mass windows. If its pulse height is within a window, the corresponding mass is assigned to this strip. This is done using the following code:

```
// Assign the masses (here for strips within mass windows)
for (int j = 0; j < event_length; j++){
  if (ampl[j] > 3840) continue;
  for (int k = 0; k < MASSES; k++) {
    if ((ampl[j] > windows[2*k][strip_num[j]])
&& (ampl[j] < windows[2*k+1][strip_num[j]])){
      masses[j] = MASS_AMU[k];
      ampl[j] = 0; //set already assigned strips to 0
                   //in order not to use them again
    }
  }
}
```

Each strip (as long as its pulse height does not exceed the highest possible value of 3840) is compared with every mass window. The number of different mass windows is `MASSES`. `windows[2*k][strip_num[j]]` is the lower bound of the mass window for peak number k and strip number j, whereas `windows[2*k+1][strip_num[j]]` is the upper bound.[1] If the pulse height fits in a mass window, the corresponding mass (in atomic mass units, but so far only as integer) is written in an array. Since `masses[j]` has been set to 0 for this event, the assigned mass will be zero if the strip does not fit in any of the windows.

The next step deals with the strips that do not fall into the mass windows. It is possible that the charge created by one fragment was recorded by two neighbouring strips, i.e. that the signal was split. For that reason, the signals of neighbouring strips are added and compared with the mass windows. In the case the comparison yields a positive result, the appropriate mass is assigned to the strip with the higher signal:

```
//now the remaining strips
```

[1] This array has been created before. If only one single mass window has been assigned to each peak, there is no dependence on the strip number.

```
for (int j = 0; j < event_length; j++){
  if (ampl[j] > 3840) continue;
  if (ampl[j] > THRESH){
    for (int k = j + 1; k < event_length; k++){
      if (ampl[k] > 3840) continue;
      if ((ampl[k] > THRESH) && (abs(strip_num[j] - strip_num[k]) == 1)){
        for (int l = 0; l < MASSES; l++) {
          if (((ampl[j] + ampl[k]) > windows[2*l][strip_num[j]])
                && ((ampl[j] + ampl[k]) < windows[2*l+1][strip_num[j]])){
            if (ampl[j] > ampl[k]) masses[j] = MASS_AMU[l];
            else masses[k] = MASS_AMU[l];
            ampl[j] = 0; /*set already assigned strips
             to 0 in order not to use them again*/
            ampl[k] = 0;
          }
        }
      }
    }
  }
}
```

Here `THRESH` is a threshold that can be used in order to suppress noise.

After that step, the array `masses[]` contains for each responding strip in the event the assigned mass. The assigned mass is zero for all strips for which the assignment failed.

In order to get an identification of the fragments, the masses on front and back side of the detector have to be compared. For that reason the strips are now reordered:

```
for (int j = 0; j < event_length; j++) {
  if ((masses[j] != 0) && (strip_num[j] < 128)) {
    posy[ny] = strip_num[j];
    massy[ny] = masses[j];
    ny++;
    total_mass_back += masses[j];
  }
```

```
  if ((masses[j] != 0) && (strip_num[j] > 199)) {
    posx[nx] = strip_num[j] - 200;
    massx[nx] = masses[j];
    nx++;
    total_mass_front += masses[j];
  }
}
```

Now the positions of the strips and the masses assigned to them are contained in the arrays `posx[]` and `massx[]` for the front side of the detector and `posy[]` and `massy[]` for the back side, respectively. `nx` and `ny` are the number of assigned strips, and `total_mass_front` and `total_mass_back` the total mass for each side.[2]

It is checked that there is no remaining strip with a signal above `THRESH`. If there is such a strip without mass assignment, the event will be considered as unusable and therefore left out in the following analysis steps. This can be achieved by setting `total_mass_front` to a negative value:

```
for (int j = 0; j < event_length; j++){
  if (ampl[j] > THRESH) total_mass_front = -1; //events with unassigned
                                               //strips are discarded
}
```

A.3.3 Identification of the fragments (fragment assignment)

A very easy check is the comparison of the masses for front and back side. If they are not the same, the event has to be discarded. This is certainly the case if `total_mass_front` was set to a negative value in the previous step.

After passing this check, the event is assigned to one of two categories: `nx >= ny` and `nx < ny`. These two cases are now treated separately. Here the case `nx >= ny` will be considered:

```
if (nx >= ny) {
```

[2]These variables have to be set to zero at the beginning of the analysis of each event.

```
for (int j = 0; j < nx; j++) { //obvious
  for (int k = 0; k < ny; k++) {
    if (massx[j] == massy[k]) {
      posx_ro[j] = (Float_t) posx[j];
      posy_ro[j] = (Float_t) posy[k];
      mass[j] = massx[j];
      n_masses++;
      massy[k] = 0;
      massx[j] = 0;
      k=ny;
    }
  }
} // end for int j < nx

for (int j = 0; j < ny; j++) {
  if (massy[j] != 0) {
    dummy = massy[j];
    counter = 0;
    for (int k = 0; k < nx; k++) { //multiple hits on a strip
                                        //(first attempt)
      dummy -= massx[k];
      if (massx[k] != 0) {
        massx_backup[k] = massx[k];
        mass[k] = massx[k];
        counter++;
        posx_ro[k] = (Float_t) posx[k];
        posy_ro[k] = (Float_t) posy[j];
        massx[k] = 0;
      }
      if (dummy == 0){
        n_masses += counter;
        k = nx;
        massy[j] = 0;
```

```
      }
    }// end for int k < nx
    if (dummy != 0){
      //dummy = massy[j];
      for (int k = 0; k < nx; k++){
        massx[k] = massx_backup[k];
      }
      for (int k = 0; k < nx; k++){
        for (int l = k; l < nx; l++){
         //several strips with double hits (second attempt)
          if ((massx[k] + massx[l]) == massy[j]){
            mass[k] = massx[k];
            n_masses++;
            mass[l] = massx[l];
            n_masses++;
            posx_ro[k] = (Float_t) posx[k];
            posy_ro[k] = (Float_t) posy[j];
            posx_ro[l] = (Float_t) posx[l];
            posy_ro[l] = (Float_t) posy[j];
            massx[k] = 0;
            massx[l] = 0;
            massy[j] = 0;
            k = nx;
          }
        }
      }
    }
  }// end if massy[j] != 0
} // end for int j < ny

counter = 0;
//special L-shaped events:
//find heigher and lower mass on each side
```

```
//interpretation: the smaller of the two highest masses
//is the mass of one fragment, the smaller of the two
//lowest masses another fragment
for (int j = 0; j < ny; j++){
  if (massy[j] != 0){
    counter++;
    if (massy[j] < massy_min) massy_min = massy[j];
    if (massy[j] > massy_max) massy_max = massy[j];
  }
}

if (counter > 2) counter = 5;  //only one L allowed

for (int j = 0; j < nx; j++){
  if (massx[j] != 0){
    counter++;
    if (massx[j] < massx_min) massx_min = massx[j];
    if (massx[j] > massx_max) massx_max = massx[j];
  }
}

if (counter == 4){  //only one L allowed
  for (int j = 0; j < nx; j++){
    for (int k = 0; k < ny; k++){
      if ((massx[j] == massx_max) && (massy[k] == massy_max)){
        if (massx_max > massy_max){
          mass[j] = massy[k];
          posx_ro[j] = (Float_t) posx[j];
          posy_ro[j] = (Float_t) posy[k];
          n_masses++;
          last_mass1 = massx[j] - massy[k];
          massy[k] = 0;
        }
```

```
        if (massx_max < massy_max){
          mass[j] = massx[j];
          posx_ro[j] = (Float_t) posx[j];
          posy_ro[j] = (Float_t) posy[k];
          n_masses++;
          last_mass1 = massy[k] - massx[j];
          massx[j] = 0;
        }
      }
      if ((massx[j] == massx_min) && (massy[k] == massy_min)){
        if (massx_min > massy_min){
          mass[j] = massy[k];
          posx_ro[j] = (Float_t) posx[j];
          posy_ro[j] = (Float_t) posy[k];
          n_masses++;
          last_mass2 = massx[j] - massy[k];
          massy[k] = 0;
        }
        if (massx_min < massy_min){
          mass[j] = massx[j];
          posx_ro[j] = (Float_t) posx[j];
          posy_ro[j] = (Float_t) posy[k];
          n_masses++;
          last_mass2 = massy[k] - massx[j];
          massx[j] = 0;
        }
      }
    }
  }
  for (int j = 0; j < nx; j++){
    if (massx[j] != 0){
      for (int k = 0; k < ny; k++){
        if (massy[k] != 0){
```

```
            mass[n_masses] = last_mass1;
            posx_ro[n_masses] = (Float_t) posx[j];
            posy_ro[n_masses] = (Float_t) posy[k];
            massx[j] = 0;
            massy[k] = 0;
            n_masses++;
          }
        }
      }
    }
  }

  if (counter > 4) massy[0] = -1;  //only one L allowed

  for (int j = 0; j < ny; j++){
    //cout << massy[j] << endl;
    if (massy[j] != 0) {
      check = -1;
      j = ny;
    }
  }

} // end if nx >= ny
```

The idea is the following: Whenever a pair of strips on front and back side with the same mass is found, they are considered to belong to the same fragment, and its mass and coordinates are written to the arrays `mass[]`, `posx_ro[]`, and `posy_ro[]`. As long as there are no multiple hits on a strip, all fragments will be identified (see fig. A.1). (Special cases will be considered later.)

If there is one additional strip on one side, then one strip on the other side should not find a partner, but its mass should be the sum of masses of the two strips that are left over. This is the case when two fragments hit the same strip. Similarly, if more than two fragments hit the same strip, the sum of masses of the remaining strips on one side

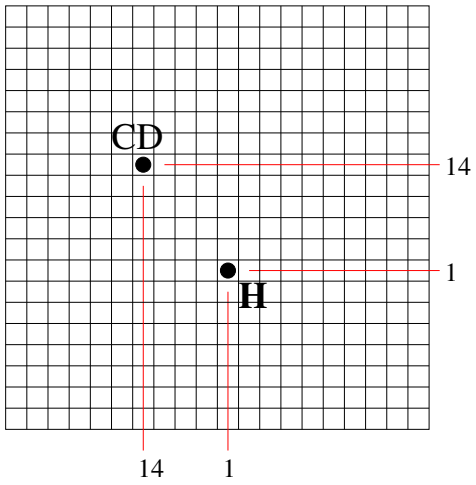

Figure A.1: An example of a simple EMU event with nx = 2 and ny = 2.

should be equal to the mass of the only remaining strip on the other side. This is checked in a second step: From the mass of the first (and probably only) remaining strip on the side with *less* strips the masses of the remaining strips on the other side are successively subtracted until a value of zero is obtained. This is repeated if there are still remaining strips. By applying this procedure all events shown in fig. A.2 can be identified.[3]

Although the second event in fig. A.2 is an example with more than one strip with multiple hits on the same side that can be accidentally identified with this procedure, this does not work in general (see fig. A.3). Assuming that two strips on one and four strips on the other side are left over, i. e. a pair of strips should always sum up to the mass of one strip. The task is now to find the correct pairings. This is done in the next step, assuming that there are only two fragments on strips with multiple hits. This means that the procedure is able to identify all events with multiple hits on either front *or* back side for systems with up to four fragments. In the case of five fragments, an event with two fragments on one and three fragments on a second strip will not always be identified. On the other hand, such an event is considered to be very unlikely.

Whereas these events can uniquely be identified, the case of strips with multiple hits on both front *and* back side is much more complicated and does in general not allow for an unambiguous interpretation. Although these events are rather unlikely, at least the

[3]Here and in the following examples it is suggested that the order of appearance of the strips in the corresponding arrays reflects their position on the detector. This is not true in general! Here this pictorial interpretation is chosen for better understanding and does not affect the general conclusions.

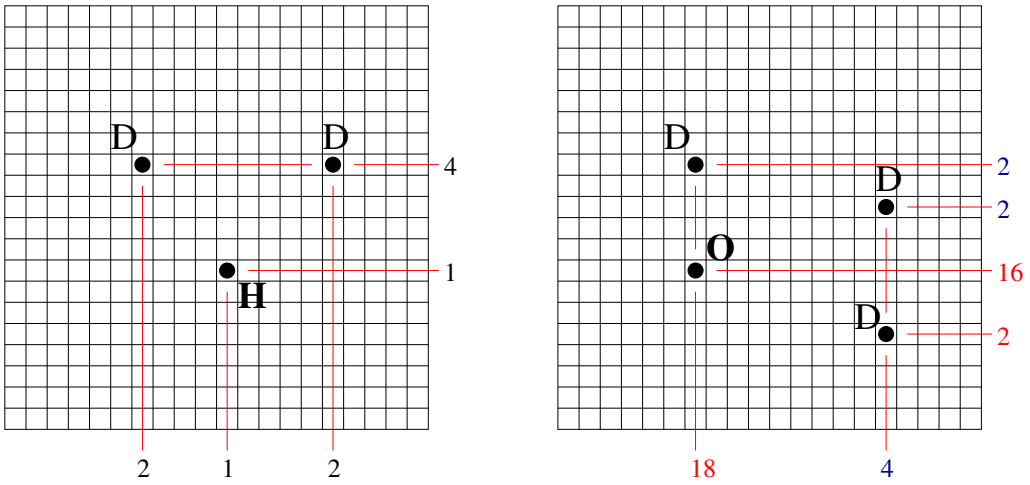

Figure A.2: Left: An example with nx = 3 and ny = 2. Every vertical strip is first compared to every horizontal strip. This leads to the identification of the H. After that, it is checked that the remaining vertical strips sum up to the mass of the only remaining horizontal strips. The procedure yields a complete identification of the event. Right: An event with nx = 2 and ny = 4. No fragment is found in the first step – there is no pair of strips with the same mass on front and back side. In the second step, an identification of all fragments is possible since the masses of the first and the second strip (counted bottom-up, as in an x-y-frame with the origin in the lower left corner) on the back side add up to the mass of the first strip on the front side, the same for the third and fourth strip on the back side and the second strip on the front side. Notice that this gives us an identification of the fragments, not necessarily their correct impact positions!

most common types should be handled in a consistent way. The last part of the source code above is dedicated to the identification of so called "L-shaped" events, i. e. three fragments hitting the detector in such a way that the signals are seen on only two strips on both front and back side (see fig. A.4). If the fragments sitting in the corners of the L have different masses, then all four strips show a different mass. I. e. that neither of the identification steps performed before is able to identify any fragment. Unfortunately, this kind of L-shaped event turns out to be ambiguous regarding the fragment masses. The argument goes now as follows: The smallest of all four masses is obviously the mass of the lighter of the two fragments in the corners. The masses of the other two fragments are not so clear, but the largest mass of all four strips is the sum of the masses of the heaviest fragment and another fragment. If the heaviest fragment is sitting in the kink, then the two strips with the bigger mass on front and on back side represent double hits, their masses

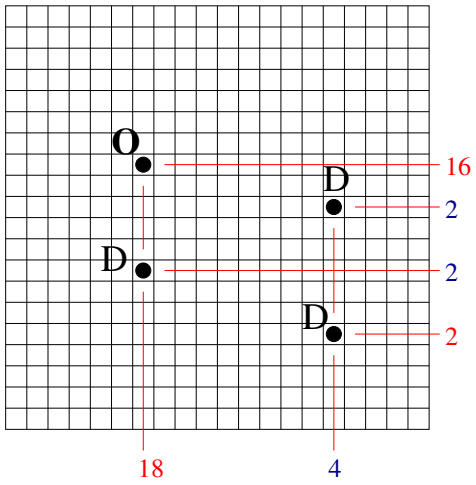

Figure A.3: In this example the fragments cannot be identified by successively subtracting the masses of the horizontal strips from the masses of the vertical strips. For that reason, all pairs of horizontal strips have to be compared to the vertical strips. E.g. the first and fourth horizontal strip sum up to the mass of the first vertical strip, as well as the second and third horizontal and the second vertical strip do. Since there are only two fragments on the same strip, this results in a complete identification of the event.

being the sum of masses of the heaviest fragment and the lightest or the second heaviest fragment, respectively. If the heaviest fragment is sitting in one of the corners, its mass corresponds to either the smaller of the highest masses on front and back side, respectively, or the bigger of the two smaller masses. The latter case yields the highest possible mass for the heaviest fragment. Since in many examples in DR decay channels for which fragments with low mass are ejected and a fragment with comparatively high mass is left are preferred, this is the interpretation that has been implemented in the code above[4]. In any case one should be aware of possible misinterpretations and study their effects using simulations if necessary.

In summary this part of the identification is composed of four subparts: At the beginning a simple comparison of front and back side is performed, and for each pair of strips with the same mass a fragment is assigned. The other three stages of the procedure deal only with the remaining strips. There are two attempts to deal with multiple hits: The first one assumes that there is one strip with multiple hits (the multiplicity being arbitrary) and

[4]This can be changed if desired, e. g. if the resulting interpretation is forbidden for energetic or other reasons.

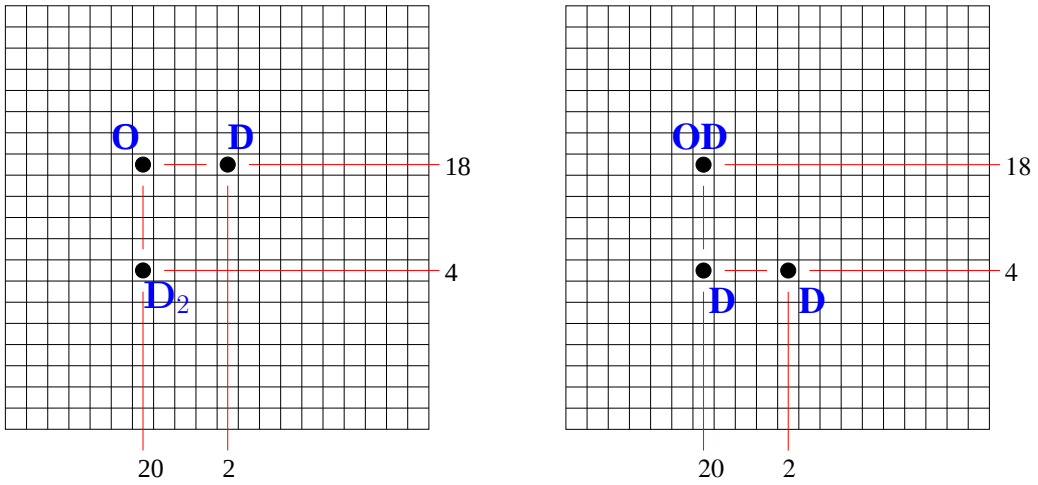

Figure A.4: Two L-shaped events with fragments of different mass in the corners. They produce the same strip pattern and can therefore not be distinguished. A special part of the identification routine is dedicated to these events, whereas such a strip pattern will always be interpreted as the event on the right, as described in the text.

tries to prove this by successively subtracting the masses that are left over on the side with more strips from the strip with suspected multiple hits until a value of zero is obtained. (By accident some events with more that one strip with multiple hits can be identified.) If this procedure fails, in a second attempt all pairs of strips from the side with more strips are compared to the strips on the other side. This assumes that there are at least two strips with multiple hits on the same side (otherwise the step before would have been successful) and that each of them is hit by only two fragments. If there are still unassigned strips after that step, a check for special L-shaped events is performed. This requires that there are exactly two remaining strips on each side, i. e. that there is only one (suspected) L. One has to think of these steps as a sequence tailored to find *some* fragments at each stage until all strips are assigned. Steps two and three are two alternatives at the same stage.

One should emphasize that in this procedure not only the masses of the fragments are determined, but also their positions are assigned. Whereas the mass identification – except for the special L-shaped events and some other cases considered later – is unique, the positions are sometimes ambiguous. This is a general problem of a strip detector if there are fragments with the same mass (see e.g. figs. A.2 (right) and A.3). Since usually only quantities which are not affected by this ambiguity are of interest, like fragment distances, transversal kinetic energy releases etc., this should not be a problem at all, but one should

keep this in mind when e. g. the distribution of fragments on the detector is considered.

The variables `n_masses` and `check` are needed for the further classification of the event. `n_masses` is set to zero at the beginning, and is incremented by one for each fragment that was found. After the step described above, it should be equal to the number of fragments in the event. But it might be that the comparison between front and back side failed for some reason, i.e. the sum of masses for front and back side is the same, but the algorithm above does not cover the arrangement of the strips. In that case we do not have a regular event, and the variable `check` is set to -1. On the other hand, if the sum of masses differs for front and back side, the variable `n_masses` will necessarily stay zero, and we do not have a regular event again. In order to keep consistent labelling of the events, the variables `n_masses` and `check` are now synchronised:

```
if (n_masses == 0) check = -1;
if (check == -1) n_masses = 0;
```

Now any irregular event (noise, fragment not visible on one of the two sides, event reconstruction failed etc.) can be excluded using any of these two variables.

The next step is the assignment of the `check` variable for the remaining events. We notice that `check` is zero for all regular events. For all these events we have `total_mass_front == total_mass_back`, and we can compare this now with the total mass of the molecule under investigation. If the total mass observed in the event is not the same as the total mass of the molecule, then the `check` variable is not changed, i.e. a value of zero means that we have a regular event that was not recognized as a DR event (e.g. DE, collision with the residual gas, DR with a fragment that was not detected)[5].

For all DR events, `check` gets a positive value, which acts as a label specifying the decay channel. The following rules shall be applied if possible:

- Each DR channel gets its own unique positive value.
- If uniquely possible, the value assigned to `check` is the mass of the heaviest fragment.
- In other cases, the mass of the second (third,....) heaviest fragment is used.
- In any case the values should be documented, at least in the source code. This is particularly important if a different scheme is used.

[5]This does not rule out events with a total mass greater than the mass of the molecule under investigation!

It should be taken into account that all possible events with the total mass of the molecule should get their own `check` value, even if their occurrence is not possible for physical reasons. This helps to monitor systematical uncertainties due to misassignments. Otherwise these events would also get the value zero.

The next step affects the position of the fragments. So far only the strip numbers are known. Since in the usual case the whole signal is detected by only one strip on either side, the position information cannot be improved[6]. If the strip numbers (which are integer numbers) would be used as fragment positions, a continuous variable would be replaced by a descrete variable. This leads to artefacts in the subsequent analysis, e.g. a preference of certain bins in a histogram of fragment distances, depending on the bin size. In order to avoid this, the position is artificially spread over the whole strip width. This is achieved by adding a random number between zero and one to the strip number:

```
// randomize position on each stripe
for (int j = 0; j < n_masses; j++) {
  posx_ro[j] += rand.Rndm();
  posy_ro[j] += rand.Rndm();
}
```

`rand` is an instance of the ROOT class *TRandom3*. The method `Rndm()` creates a uniformly distributed floating point random number in the intervall `]0,1]`.

The variables `n_masses`, `mass[]`, `posx_ro[]` and `posy_ro[]` are written to the branches *n_masses*, *mass*, *fposx*, and *fposy*, respectively.

A.3.4 Special cases

As was already pointed out, the event reconstruction procedure can handle events with one strip with multiple hits on either the front *or* the back side. Two and more strips with multiple hits on the *same* side are covered as long as there are only two fragments on one strip. Problematic are events with multiple hits on both front *and* back side. Here we have so far only considered so called "L-shaped" events with fragments of different mass sitting in the corners of the L.

[6] If the signal would be spread over several strips, a fit could yield a position that is more precise than the limit given by the strip width.

Let us now consider L-shaped events with two fragments of the same mass sitting on the ends of the L, and a third fragment in the kink. This results in only two responding strips on either side. Each strip on the front side has a partner with the same mass on the back side (see fig. A.5). I. e. the algorithm finds only two fragments, one of them at the position of the kink but with an incorrect mass, the other with the mass of one of the fragments at the ends but at an incorrect position. Since this interpretation is also a regular event, it

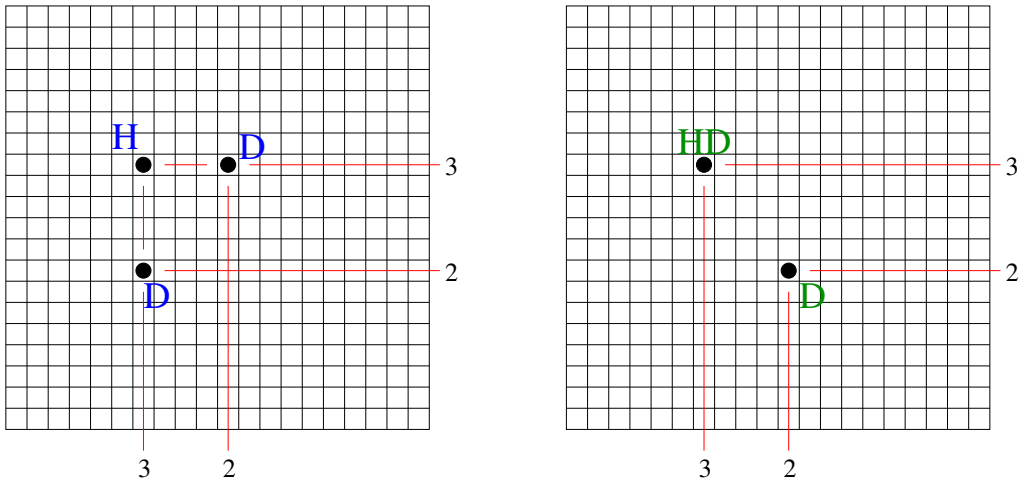

Figure A.5: An example of an L-shaped event (left). This will always be interpreted as a two-body event (right). Since there is no way to distinguish these two events, misassignments will necessarily occur. They can only be accounted for using simulational techniques.

will consequently be adopted for this kind of pattern, i. e. these L-shaped events are always interpreted the wrong way. It is left to a simulation to estimate the number of these wrong assignments, which are in general negligible.

For systems with more than four fragments, special arrangements can occur that are not always recognized by the identification routine. An example is shown in fig. A.6. Here it depends on the exact arrangement if the masses can be obtained with the method of successive subtraction. In general these events can be quite complicated: Assuming that the number of strips are nx and ny (with ny $>$ nx), and that the number of fragments is ny (no multiple hits on the y side), all possible multiplicities $n_1 ... n_{nx}$ with $\sum_{i=1}^{nx} n_i = ny$ and $n_i > 1$ (otherwise it would have been found before) and for each multiplicity all permutations of fragments with different mass are possible solutions and have to be tried out. This is currently not implemented.

The last example shows how the event reconstruction works for a quite complicated event

(see fig. A.7).

A.4 Calculation of CM

After calling the fragment identification routine, *cm_identify()* proceeds with the center-of-mass calculation, which is now straightforward. The cm data are contained in the tree *CM* in the ROOT file *<name_of_beamtime>_<run_number>_cm_data.root*.

Branch	**Leaf(s)**	**Data type**
cmx	cmx	F
cmy	cmy	F

`cmx` and `cmy` are only calculated for DR events (`check > 0`). For all other events they are zero.

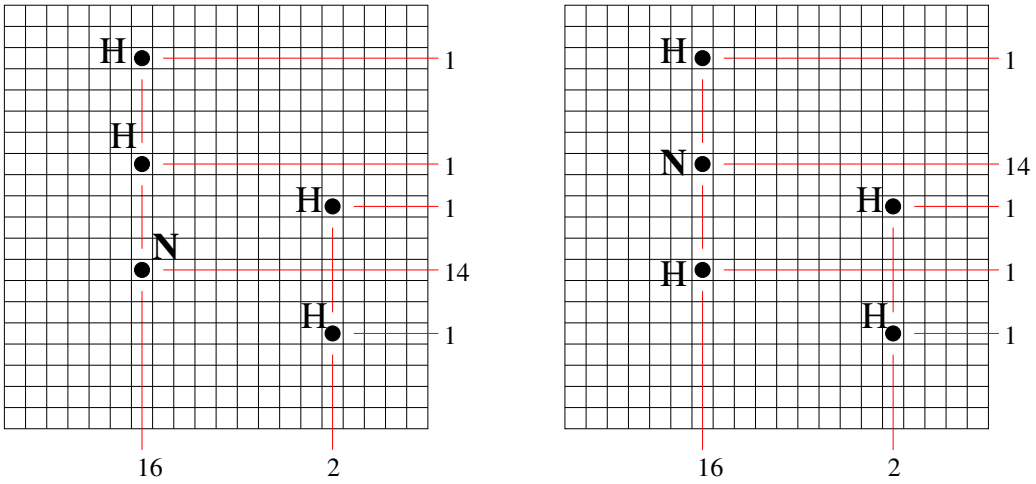

Figure A.6: Events with five fragments. Using the method of successive subtraction all fragments in the left event are found. For the event on the right the current identification routine fails.

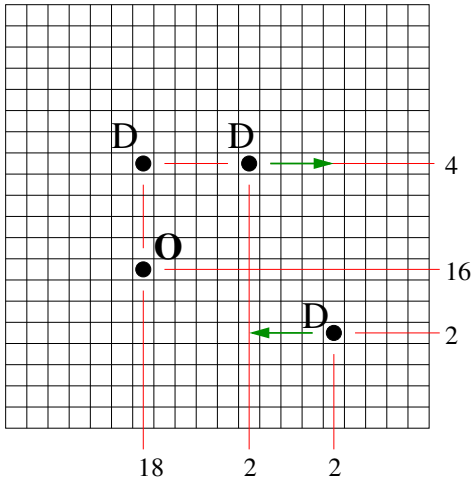

Figure A.7: An event where all fragments are correctly identified. In the first identification step, a D is assigned to the horizontal and one of the vertical strips with mass 2. What remains is obviously an L-shaped pattern, that will be accounted for in the appropriate identification step which provides in this case the correct fragment masses by virtue of its construction. Remember: The fragment positions are ambiguous. Here the routine will shift the positions of two fragments (green arrows).

B Estimation of rotational lifetimes of $DCND^+$

Starting from the assumption that the ion $DCND^+$ is in its vibrational ground state, the lifetimes of rotationally excited states depend on purely rotational transitions due to spontaneous emission. The lifetime for an ion in the initial state i with rotational quantum number J is

$$\tau = \frac{1}{\sum_f A_{fi}}, \tag{B.1}$$

whereas A_{fi} is the Einstein coefficient for spontaneous emission pertaining to a transition $J \rightarrow J'$ and the sum has to be taken over all final states that are energetically below the initial state, i. e. $J' < J$, taking multiplicities due to the quantum number $M_{J'}$ into account. A formula for the Einstein coefficient in the dipole approximation can be found in any textbook on atomic physics:

$$A_{fi} = \frac{1}{3\pi\varepsilon_0 c^3 \hbar}\, \omega_{fi}^3 \left|\vec{\mu}_{fi}\right|^2, \tag{B.2}$$

with the transition frequency $\omega_{fi} = 2\pi\nu_{fi}$, and the transition dipole moment $\vec{\mu}_{fi} = \langle f|\vec{\mu}|i\rangle$, while $\vec{\mu}$ is the dipole moment operator. For purely rotational transitions, we have $i = (J, M_J)$ and $f = (J', M_{J'})$ with $J' = J - 1$ and $M_{J'} = M_J,\ M_J \pm 1$ (dipole allowed transitions). Adding all the contributions gives

$$\sum_{M_{J'}} \left|\langle J-1,\ M_{J'}|\vec{\mu}|J,\ M_J\rangle\right|^2 = \mu^2\, \frac{J}{2J+1} \tag{B.3}$$

with $\mu = |\vec{\mu}|$ (equation 1-76 in [92]). The dipole moment of $DCND^+$ has been calculated by Botschwina [86] and is $\mu = 0.26$ D $= 0.054$ eÅ. The transition frequency can be expressed

J	τ	rotational energy (eV)
1	9.6 months	0.00022
2	1 month	0.00066
3	8.3 days	0.00133
20	35 minutes	0.046
30	627 s	0.10
50	136 s	0.28
70	50 s	0.55
100	17.6 s	1.11

Table B.1: Lifetimes of some rotationally excited states of $DCND^+$ in the vibrational ground state up to $J = 100$, and the corresponding rotational energies.

by the rotational constants B_e and D_e as

$$\nu = 2B_eJ - 4D_eJ^3. \tag{B.4}$$

These constants have been measured [93]: $B_e = 26774.1295$ MHz $= 0.893$ cm^{-1}, $D_e = 0.024888$ MHz $= 8.3 \cdot 10^{-7}$ cm^{-1}.

Putting everything together, the lifetimes can be calculated using

$$\frac{1}{\tau} = 7.234 \cdot 10^{-6} \cdot (2B_eJ - 4D_eJ^3)^3 \, \mu^2 \, \frac{J}{2J+1} \tag{B.5}$$

with B_e and D_e in cm^{-1}, μ in eÅ, and τ in s.

It should be noted that this expression contains some approximations. First of all, the transition dipole moments are based on a rigid rotor model, i. e. a centrifugal distortion is neglected. Thus, the dipole moment of the molecule is assumed to be independent of the rotational state. The value that has been chosen corresponds to the equilibrium geometry of $DCND^+$. Furthermore, for polyatomic linear molecules, the so-called *l-type doubling* [92] should be taken into account. However, since it is assumed that the molecule is in its vibrational ground state, this does not apply here.

Some results are shown in table B.1. The long lifetimes as well as the small energy spacings between the rotational levels reveal long rotational cooling times.

C Exothermicities for the DR of $DCND^+$

The exothermicities for the different decay channels of $DCND^+$ can not be retrieved from the usual sources and have therefore to be estimated. It should be stressed, however, that they are only needed for the interpretation of the results (see e. g. fig. 6.24) and do enter the analysis in any way!

Exothermicities for the DR of $HCNH^+$ have been calculated by Semaniak *et al.* [76] and are shown in table 6.1. For $DCND^+$, they have to be corrected for the different zero-point energies of the deuterated species. The vibrational energies for the different modes for DCN, DNC and $HCNH^+$ are available from the NIST database [94] (for DNC different values are listed for each vibrational mode). The zero-point energies are estimated to be one-half times the sum of these energies. The results are: $2562\,cm^{-1}$ for DCN, about the same for DNC, and $5137\,cm^{-1}$ for $HCNH^+$. For $DCND^+$, the harmonic frequencies have been calculated by Botschwina [86], and the resulting zero-point energy is $4136\,cm^{-1}$. The zero-point energies for HCN and HNC have been calculated by Bowman *et al.* [75] and are $3477.4\,cm^{-1}$ and $3299\,cm^{-1}$, respectively.

Thus, the differences between the zero-point energies are 0.11 eV between HCN and DCN, 0.09 eV between HNC and DNC, and 0.12 eV between $HCNH^+$ and $DCND^+$, i. e. the parent ion as well as the fragments are about 0.1 eV lower for the deuterated species, and the differences cancel for the two dissociation channels leading to DCN and DNC. However, the exothermicity of the three-body channel (CN + D + D) reduces by 0.1 eV.

The exothermicities according to [76] and corrected for the zero-point energies are:

Channel	Exothermicity (eV)
DCN + D	5.9
DNC + D	5.3
CN + D + D	0.5

Bibliography

[1] M. Larsson and A.E. Orel, *Dissociative recombination of molecular ions*, Cambridge University Press, 2008.

[2] D.R. Bates, *Dissociative recombination*, Phys. Rev. **78** (1950), 492–493.

[3] W.D. Watson, *Ion-Molecule Reactions, Molecule Formation, and Hydrogen-Isotope Exchange in Dense Interstellar Clouds*, The Astrophysical Journal **188** (1974), 35.

[4] Joseph Kaplan, *The light of the night sky*, Phys. Rev. **38** (1931), 1048–1051.

[5] M. H. Rees, *Excitation of O (^1S) and emission of 5577 Å radiation in aurora*, Planetary and Space Science **32** (1984), 373–378.

[6] Richard P. Wayne, *Chemistry of Atmospheres*, third ed., Oxford University Press, 2000.

[7] D. R. Bates and H. S. W. Massey, *The basic reactions in the upper atmosphere. II. The theory of recombination in the ionized layers*, Proceedings of the Royal Society of London. Series A, Mathematical and Physical Sciences **192** (1947), 1–16.

[8] Wolfgang Demtröder, *Molekülphysik*, Oldenbourg Verlag, 2003.

[9] M. Born and R. Oppenheimer, *Zur Quantentheorie der Molekeln*, Annalen der Physik **84** (1927), 457.

[10] J. von Neumann and E. Wigner, *Über merkwürdige diskrete Eigenwerte. Über das Verhalten von Eigenwerten bei adiabatischen Prozessen*, Phys. Z. **30** (1929), 467–470.

[11] H. Buhr, H. B. Pedersen, S. Altevogt, V. M. Andrianarijaona, H. Kreckel, L. Lammich, S. Novotny, D. Strasser, J. Hoffmann, M. Lange, M. Lestinsky, M. B. Mendes, M. Motsch, O. Novotný, D. Schwalm, X. Urbain, D. Zajfman, and A. Wolf, *Inelastic electron collisions of the isotopically symmetric helium dimer ion $^4He_2^+$ in a storage ring*, Phys. Rev. A **77** (2008), 032719.

[12] J.N. Bardsley, *The theory of dissociative recombination*, Journal of Physics B: Atomic and Molecular Physics **1** (1968), 365–380.

[13] D. Zajfman, Z. Amitay, C. Broude, P. Forck, B. Seidel, M. Grieser, D. Habs, D. Schwalm, and A. Wolf, *Measurement of Branching Ratios for the Dissociative Recombination of Cold HD^+ Using Fragment Imaging*, Phys. Rev. Lett. **75** (1995), 814–817.

[14] D. Shafir, S. Novotny, H. Buhr, S. Altevogt, A. Faure, M. Grieser, A. G. Harvey, O. Heber, J. Hoffmann, H. Kreckel, L. Lammich, I. Nevo, H. B. Pedersen, H. Rubinstein, I. F. Schneider, D. Schwalm, J. Tennyson, A. Wolf, and D. Zajfman, *Rotational Cooling of HD^+ Molecular Ions by Superelastic Collisions with Electrons*, Phys. Rev. Lett. **102** (2009), 223202.

[15] E. Herbst, *What are the products of polyatomic ion-electron dissociative recombination reactions*, The Astrophysical Journal **222** (1978), 508–516.

[16] D. R. Bates, *Products of dissociative recombination of polyatomic ions*, The Astrophysical Journal **306** (1986), L45–L47.

[17] ———, *Dissociative recombination of polyatomic ions*, Journal of Physics B Atomic Molecular Physics **24** (1991), 3267–3284.

[18] O Novotny, O Motapon, M H Berg, D Bing, H Buhr, H Fadil, M Grieser, J Hoffmann, A S Jaroshevich, B Jordon-Thaden, C Krantz, M Lange, M Lestinsky, M Mendes, S Novotny, D A Orlov, A Petrignani, I F Schneider, A E Orel, and A Wolf, *Dissociative recombination of CF^+: Experiment and theory*, Journal of Physics: Conference Series **192** (2009), 012021.

[19] D. Strasser, J. Levin, H. B. Pedersen, O. Heber, A. Wolf, D. Schwalm, and D. Zajfman, *Branching ratios in the dissociative recombination of polyatomic ions: The H_3^+ case*, Phys. Rev. A **65** (2001), 010702.

[20] www.astrochymist.org.

[21] D.R. Bates and L.J. Spitzer, *The Density of Molecules in Interstellar Space.*, The Astrophysical Journal **113** (1951), 441.

[22] E. Herbst and W. Klemperer, *The formation and depletion of molecules in dense interstellar clouds*, The Astrophysical Journal **185** (1973), 505.

[23] www.udfa.net.

[24] A.I. Florescu-Mitchell and J.B.A. Mitchell, *Dissociative recombination*, Physics Reports **430** (2006), 277–374.

[25] N.G. Adams, V. Poterya, and L.M. Babcock, *Electron molecular ion recombination: Product excitation and fragmentation*, Mass Spectrometry Reviews **25** (2006), 798–828.

[26] Glenn F. Knoll, *Radiation Detection and Measurement*, John Wiley & Sons, 1989.

[27] A. Coche and P. Siffert, *Surface-barrier diodes*, Semiconductor Detectors (G. Bertolini and A. Coche, eds.), North Holland Publishing Company, 1968.

[28] ———, *N-P detectors*, Semiconductor Detectors (G. Bertolini and A. Coche, eds.), North Holland Publishing Company, 1968.

[29] S. Datz, M. Larsson, C. Stromholm, G. Sundström, V. Zengin, H. Danared, A. Källberg, and M. af Ugglas, *Dissociative recombination of H_2D^+: Cross sections, branching fractions, and isotope effects*, Phys. Rev. A **52** (1995), 2901–2909.

[30] L.H. Andersen, O. Heber, D. Kella, H.B. Pedersen, L. Vejby-Christensen, and D. Zajfman, *Production of Water Molecules from Dissociative Recombination of H_3O^+ with Electrons*, Phys. Rev. Lett. **77** (1996), 4891–4894.

[31] A. Neau, A. Al Khalili, S. Rosén, A. Le Padellec, A.M. Derkatch, W. Shi, L. Vikor, M. Larsson, J. Semaniak, and R. Thomas, *Dissociative recombination of D_3O^+ and H_3O^+: Absolute cross sections and branching ratios*, Journal of Chemical Physics **113** (2000), 1762–1770.

[32] M.J. Jensen, R.C. Bilodeau, C.P. Safvan, K. Seiersen, L.H. Andersen, H.B. Pedersen, and O. Heber, *Dissociative Recombination of H_3O^+, HD_2O^+, and D_3O^+*, The Astrophysical Journal **543** (2000), 764–774.

[33] A. Wolf, D. Schwalm, and D. Zajfman, *Fragment imaging studies of dissociative recombination*, Many-Particle Quantum Dynamics in Atomic and Molecular Fragmentation, J. Ullrich and V. P. Shevelko, 2003, pp. 485–506.

[34] A.J.R. Heck and D.W. Chandler, *Imaging techniques for the study of chemical reaction dynamics*, Annual Review of Physical Chemistry **46** (1995), 335–372.

[35] V. Horvat, O. Heber, R.L. Watson, R. Parameswaran, and J.M. Blackadar, *3-D imaging of binary dissociation events induced by heavy ion impact*, Nuclear Instruments and Methods in Physics Research B **99** (1995), 94–97.

[36] W.J. van der Zande, W. Koot, D.P. de Bruijn, and C. Kubach, *Dissociative Charge Exchange of HeH^+: An Experimental Study of the HeH Molecule*, Phys. Rev. Lett. **57** (1986), 1219–1222.

[37] D. Zajfman, O. Heber, *Molecular imaging with fast ion beams*, Accelerator-based atomic physics: techniques and applications (Stephen M. Shafroth and James C. Austin, eds.), American Institute of Physics, 1997, pp. 481–507.

[38] Joseph Ladislas Wiza, *Microchannel plate detectors*, Nuclear Instruments and Methods **162** (1979), 587 – 601.

[39] D. Kella, M. Algranati, H. Feldman, O. Heber, H. Kovner, E. Malkin, E. Miklazky, R. Naaman, D. Zajfman, J. Zajfman, and Z Vager, *A system for Coulomb explosion imaging of small molecules at the Weizmann institute*, Nuclear Instruments and Methods in Physics Research A **329** (1993), 440–452.

[40] Z. Amitay, D. Zajfman, *A new type of multiparticle three-dimensional imaging detector with subnanosecond time resolution*, Rev. Sci. Instr. **68** (1997), 1387–1392.

[41] D. P. de Bruijn and J. Los, *Time and position-sensitive detector for dissociative processes in fast beams*, Rev. Sci. Instr. **53** (1982), 1020–1026.

[42] D. Strasser, X. Urbain, H. B. Pedersen, N. Altstein, O. Heber, R. Wester, K. G. Bhushan, and D. Zajfman, *An innovative approach to multiparticle three-dimensional imaging*, Rev. Sci. Instr. **71** (2000), 3092–3098.

[43] Steffen Novotny, *Fast-beam molecular fragmentation imaging using a high-speed gated camera system*, Diplomarbeit, Ruprecht-Karls-Universität Heidelberg, 2004.

[44] Mario Benjamin Mendes, *Hochauflösende dreidimensionale Fragmentabbildung bei Speicherringexperimenten mit Molekülionen*, Diplomarbeit, Ruprecht-Karls-Universität Heidelberg, 2007.

[45] Steffen Novotny, *Fragmentation of molecular ions in slow electron collisions*, Dissertation, Ruprecht-Karls-Universität Heidelberg, 2008.

[46] Viatcheslav Kokoouline and Chris H Greene, *Theoretical study of the H_3^+ ion dissociative recombination process*, Journal of Physics: Conference Series **4** (2005), 74–82.

[47] Z. Amitay, D. Zajfman, P. Forck, U. Hechtfischer, B. Seidel, M. Grieser, D. Habs, R. Repnow, D. Schwalm, and A. Wolf, *Dissociative recombination of CH^+: Cross section and final states*, Phys. Rev. A **54** (1996), 4032–4050.

[48] Lutz Lammich, *Fragmentation Studies with Stored Beams of Small Polyatomic Ions*, Dissertation, Ruprecht-Karls-Universität Heidelberg, 2005.

[49] R.H. Dalitz, *On the analysis of τ-meson data and the nature of the τ-meson*, Phil. Mag. **44** (1953), 1068.

[50] D. Habs, W. Baumann, J. Berger, P. Blatt, A. Faulstich, P. Krause, G. Kilgus, R. Neumann, W. Petrich, R. Stokstad, D. Schwalm, E. Szmola, K. Welti, A. Wolf, S. Zwickler, E. Jaeschke, D. Krämer, G. Bisoffi, M. Blum, A. Friedrich, C. Geyer, M.

Grieser, H. W. Heyng, B. Holzer, R. Ihde, M. Jung, K. Matl, W. Ott, B. Povh, R. Repnow, M. Steck, E. Steffens, D. Dutta, T. Kühl, D. Marx, S. Schröder, M. Gerhard, R Grieser, G. Huber, R. Klein, M. Krieg, N. Schmidt, R. Schuch, J. F. Babb, L. Spruch, W. Arnold, A. Noda, *First experiments with the Heidelberg test storage ring TSR*, Nuclear Instruments and Methods in Physics Research B **43** (1989), 390–410.

[51] M. Grieser, H. Deitinghoff, D. Habs, R. von Hahn, E. Jaeschke, C.-M. Kleffner, V. Kössler, S. Papureanu, R. Repnow, M.-H. Rhee, D. Schwalm, A. Schempp, *Upgrading of the Heidelberg accelerator facility with a new high current injector*, Nuclear Instruments and Methods in Physics Research A **328** (1993), 160–163.

[52] M. Steck, G. Bisoffi, M. Blum, A. Friedrich, C. Geyer, M. Grieser, B. Holzer, E. Jaeschke, M. Jung, D. Krämer, K. Matl, W. Ott, R. Repnow, *Electron cooling of heavy ions*, Nuclear Instruments and Methods in Physics Research A **287** (1990), 324–327.

[53] Frank Sprenger, *Production of cold electron beams for collision experiments with stored ions*, Dissertation, Ruprecht-Karls-Universität Heidelberg, 2003.

[54] S. Pastuszka, U. Schramm, M. Grieser, C. Broude, R. Grimm, D. Habs, J. Kenntner, H.-J. Miesner, T. Schüßler, D. Schwalm, A. Wolf, *Electron cooling and recombination experiments with an adiabatically expanded electron beam*, Nuclear Instruments and Methods in Physics Research A **369** (1996), 11–22.

[55] H. Danared, G. Andler, L. Bagge, C. J. Herrlander, J. Hilke, J. Jeansson, A. Källberg, A. Nilsson, A. Paál, K. G. Rensfelt, U. Rosengård, J. Starker, and M. af Ugglas, *Electron cooling with an ultracold electron beam*, Phys. Rev. Lett. **72** (1994), 3775–3778.

[56] D. A. Orlov, C. Krantz, A. Wolf, A. S. Jaroshevich, S. N. Kosolobov, H. E. Scheibler, and A. S. Terekhov, *Long term operation of high quantum efficiency GaAs(Cs,O) photocathodes using multiple recleaning by atomic hydrogen*, Journal of Applied Physics **106** (2009), 054907.

[57] Claude Krantz, *Intense Electron Beams from GaAs Photocathodes as a Tool for Molecular and Atomic Physics*, Dissertation, Ruprecht-Karls-Universität Heidelberg, 2009.

[58] W. K. Chu, R. H. Kastl, R. F. Lever, S. Mader, and B. J. Masters, *Distribution of irradiation damage in silicon bombarded with hydrogen*, Phys. Rev. B **16** (1977), 3851–3859.

[59] H. Buhr, M.B. Mendes, O. Novotný, D. Schwalm, M.H. Berg, D. Bing, O. Heber, C. Krantz, D.A. Orlov, M.L. Rappaport, T. Sorg, J. Stützel, J. Varju, A. Wolf, and D. Zajfman, *Energy-sensitive imaging detector applied to the dissociative recombination of* D_2H^+, 2010, arXiv: 1003.5101.

[60] www.micronsemiconductor.co.uk.

[61] www.mesytec.de.

[62] root.cern.ch.

[63] Oldřich Novotný, Henrik Buhr, Julia Stützel, Mario B. Mendes, Max H. Berg, Dennis Bing, Michael Froese, Manfred Grieser, Oded Heber, Brandon Jordon-Thaden, Claude Krantz, Michael Lange, Michael Lestinsky, Steffen Novotny, Sebastian Menk, Dmitry A. Orlov, Annemieke Petrignani, Michael L. Rappaport, Andrey Shornikov, Dirk Schwalm, Daniel Zajfman, and Andreas Wolf, *Fragmentation Channels in Dissociative Electron Recombination with Hydronium and Other Astrophysically Important Species*, J. Phys. Chem. A **114** (2010), 4870–4874.

[64] H. Buhr, J. Stützel, M.B. Mendes, O. Novotný, D. Schwalm, M.H. Berg, D. Bing, M. Grieser, O. Heber, C. Krantz, S. Menk, S. Novotny, D.A. Orlov, A. Petrignani, M.L. Rappaport, R. Repnow, D. Zajfman, and A. Wolf, *Hot water molecules from dissociative recombination of D_3O^+ with cold electrons*, submitted to Phys. Rev. Lett.

[65] Å. Larson, A. Le Padellec, J. Semaniak, C. Strömholm, M. Larsson, S. Rosén, R. Peverall, H. Danared, N. Djuric, G. H. Dunn, and S. Datz, *Branching Fractions in Dissociative Recombination of CH_2^+*, Astrophysical Journal **505** (1998), 459–465.

[66] R.D. Thomas, F. Hellberg, A. Neau, S. Rosén, M. Larsson, C.R. Vane, M.E. Bannister, S. Datz, A. Petrignani, and W.J. Van der Zande, *Three-body fragmentation dynamics of amidogen and methylene radicals via dissociative recombination*, Physical Review A **71** (2005), 32711.

[67] Evelyne Roueff, *Microphysics and astrophysical observations: the molecular perspective*, Journal of Physics: Conference Series, vol. 4, Institute of Physics Publishing, 2005, pp. 1–9.

[68] T. Amano, Z. Zelinger, T. Hirao, J. Takano, and R. Toyoda, *HNC and HCN in an extended negative glow discharge: Implication to the branching ratio of the dissociative recombination of $HCNH^+$*, Journal of Molecular Spectroscopy **251** (2008), 252–255.

[69] L.E. Snyder and D. Buhl, *Observations of radio emission from interstellar hydrogen cyanide*, The Astrophysical Journal **163** (1971), L47–52.

[70] L.E. Snyder and D. Buhl, *Radio astronomy-Interstellar methylacetylene and isocyanic acid*, Nature Physical Science **243** (1973), 45.

[71] P.K. Pearson and H.F. Schaefer, III, *Some Properties of H_2CN^+: a Potentially Important Interstellar Species*, The Astrophysical Journal **192** (1974), 33–36.

[72] A. Wootten, N. J. Evans, II, R. Snell, and P. vanden Bout, *Molecular abundance variations in interstellar clouds*, The Astrophysical Journal **225** (1978), L143–L148.

[73] E. Sarrasin, D. Ben Abdallah, M. Wernli, A. Faure, J. Cernicharo, and F. Lique, *The rotational excitation of HCN and HNC by He: new insights on the HCN/HNC abundance ratio in molecular clouds*, Monthly Notices of the Royal Astronomical Society (2010).

[74] P. Schilke, C.M. Walmsley, G. Pineau Des Forets, E. Roueff, D.R. Flower, and S. Guilloteau, *A study of HCN, HNC and their isotopomers in OMC-1. I - Abundances and chemistry*, Astronomy and Astrophysics **256** (1992), 595–612.

[75] Joel M. Bowman, Bela Gazdy, Joseph A. Bentley, Timothy J. Lee, and Christopher E. Dateo, *Ab initio calculation of a global potential, vibrational energies, and wave functions for HCN/HNC, and a simulation of the $\tilde{A} - \tilde{X}$ emission spectrum*, The Journal of Chemical Physics **99** (1993), 308–323.

[76] J. Semaniak, B.F. Minaev, A.M. Derkatch, F. Hellberg, A. Neau, S. Rosén, R. Thomas, M. Larsson, H. Danared, A. Paál, and M. af Ugglas, *Dissociative recombination of $HCNH^+$: absolute cross-sections and branching ratios*, The Astrophysical Journal Supplement Series **135** (2001), 275–283.

[77] L.M. Ziurys and B.E. Turner, *$HCNH^+$: a new interstellar molecular ion*, The Astrophysical Journal **302** (1986), L31–L36.

[78] Dahbia Talbi and Yves Ellinger, *Potential energy surfaces for the electronic dissociative recombination of $HCNH^+$: astrophysical implications on the HCN/HNC abundance ratio*, Chemical Physics Letters **288** (1998), 155–164.

[79] Yoko Shiba, Tsuneo Hirano, Umpei Nagashima, and Keisaku Ishii, *Potential energy surfaces and branching ratio of the dissociative recombination reaction $HCNH^+ + e^-$: An ab initio molecular orbital study*, The Journal of Chemical Physics **108** (1998), 698–705.

[80] Hiroto Tachikawa, *Reaction mechanism of the astrochemical electron capture reaction $HCNH^+ + e^- \rightarrow HNC + H$: a direct ab-initio dynamics study*, Phys. Chem. Chem. Phys. **1** (1999), 4925–4930.

[81] A.P. Hickman, R.D. Miles, C. Hayden, and D. Talbi, *Dissociative recombination of $e + HCNH^+$: Diabatic potential curves and dynamics calculations*, Astronomy and Astrophysics **438** (2005), 31–37.

[82] K. Ishii, A. Tajima, T. Taketsugu, and K. Yamashita, *Theoretical Elucidation of the Unusually High [HNC]/[HCN] Abundance Ratio in Interstellar Space: Two-dimensional*

and Two-State Quantum Wave Packet Dynamics Study on the Branching Ratio of the Dissociative Recombination Reaction $HCNH^+ + e^- \rightarrow HNC/HCN + H$, The Astrophysical Journal **636** (2006), 927–931.

[83] M. Grieser, R. Bastert, K. Blaum, H. Buhr, R. von Hahn, M. B. Mendes, R. Repnow, and A. Wolf, *Acceleration, deceleration and bunching of stored and cooled ion beams at the TSR, Heidelberg*, HIAT 09 Proceedings, Venice, 2009.

[84] G. Audi, A.H. Wapstra, C. Thibault, Blachot J., and O. Bersillon, *The Ame2003 atomic mass evaluation (II)*, Nuclear Physics A **729** (2003), 337–676.

[85] Christian Nordhorn, private communication.

[86] Peter Botschwina, *Spectroscopic properties of $HCNH^+$ calculated by SCEP CEPA*, Chemical Physics Letters **124** (1986), 382–390.

[87] T. Barger, A.M. Wodtke, and J.M. Bowman, *Isomeric Branching of Highly Excited H/C/N*, The Astrophysical Journal **587** (2003), 841–846.

[88] A.E. Ketvirtis and J. Simons, *Dissociative recombination of H_3O^+*, J. Phys. Chem. A **103** (1999), 6552–6563.

[89] R.J. Barber, S. Miller, T. Stallard, J. Tennyson, P. Hirst, T. Carroll, and A. Adamson, *The United Kingdom Infrared Telescope Deep Impact observations: Light curve, ejecta expansion rates and water spectral features*, Icarus **191** (2007), 371–380.

[90] D. Strasser, L. Lammich, H. Kreckel, S. Krohn, M. Lange, A. Naaman, D. Schwalm, A. Wolf, and D. Zajfman, *Breakup dynamics and the isotope effect in H_3^+ and D_3^+ dissociative recombination*, Phys. Rev. A **66** (2002), 32719.

[91] Michael Lestinsky, *High Resolution Electron Collision Spectroscopy with Multicharged Ions in Merged Beams*, Dissertation, Ruprecht-Karls-Universität Heidelberg, 2007.

[92] C.H. Townes and A.L. Schawlow, *Microwave Spectroscopy*, McGraw-Hill Book Company, Inc., 1955.

[93] M. Araki, H. Ozeki, and S. Saito, *Laboratory measurements of the pure rotational transitions of $HCNH^+$ and its isotopic species*, The Astrophysical Journal **496** (1998), L53–L55.

[94] webbook.nist.gov.

Danksagung

Es ist allgemein bekannt, dass eine Doktorarbeit nur Dank der Unterstützung anderer Menschen entstehen kann. Ohne viele Worte zu verlieren, danke ich daher

- Andreas Wolf, der mir diese Arbeit angeboten, sie mit stetem Interesse begleitet und durch seine hilfreichen Anregungen bereichert hat, wobei er mir immer genug Freiräume ließ, dass ich meine eigenen Ideen entwickeln konnte;
- Selim Jochim, der sich bereit erklärt hat, das Zweitgutachten zu erstellen;
- Henrik Buhr, unter dessen Betreuung ich viel gelernt habe, und der außerdem in mancher Arbeitspause einer meiner Skatpartner war;
- Dirk Schwalm, ohne den das EMU-Projekt nicht denkbar wäre;
- meinen Kollegen am Weizmann-Institut, insbesondere Oded Heber;
- meinem zweiten Skatpartner, Dennis Bing, sowie allen anderen Mitgliedern unserer Gruppe (Ehemalige eingeschlossen), auch wenn sie nicht alle namentlich erwähnt werden; sie alle haben das hervorragende Arbeitsklima erst ermöglicht;
- Manfred Grieser, Roland Repnow und den Operateuren, ohne die Strahlzeiten am TSR undenkbar wären;
- den Werkstätten, insbesondere dem Team von Karl Hahn;
- allen übrigen Serviceeinrichtungen am Max-Planck-Institut für Kernphysik, die hervorragende Arbeit leisten;
- der International Max Planck Research School for Quantum Dynamics in Physics, Chemistry, and Biology;
- allen, die ich jetzt nicht explizit erwähnt habe und die wohl selbst am besten wissen, was sie zum Erfolg meiner Arbeit beigetragen haben.